

REPORT DOCUMENTATION PAGE			Form Approved CMB No. 0704-0188	
<small>Public reporting burden for this collection of information is estimated to average 1 hour per response, including the time for reviewing instructions, searching existing data sources, gathering and maintaining the data needed, and completing and reviewing the collection of information. Send comments regarding this burden estimate or any other aspect of this collection of information, including suggestions for reducing this burden, to Washington Headquarters Services, Directorate for Information Operations and Reports, 1215 Jefferson Davis Highway, Suite 1204, Arlington, VA 22202-4302, and to the Office of Management and Budget, Paperwork Reduction Project (0704-0188), Washington, DC 20503.</small>				
1. AGENCY USE ONLY (Leave blank)	2. REPORT DATE 15/10/1995	3. REPORT TYPE AND DATES COVERED Final 1/5/1991-31/1/1995		
4. TITLE AND SUBTITLE Mechanical Properties of Porous. High Temperature Structural Materials: Sources of Toughness in Reaction Bonded Silicon Nitride		5. FUNDING NUMBERS AFOSR-91-0263		
6. AUTHOR(S) Ali S. Argon and John S. Haggerty				
7. PERFORMING ORGANIZATION NAME(S) AND ADDRESS(ES) Massachusetts Institute of Technology 77 Massachusetts Avenue Cambridge, MA 02139 (Dept. of Mechanical Eng. & Materials Processing Center)		8. PERFORMING ORGANIZATION REPORT NUMBER AFOSR-TR-95 0699		
9. SPONSORING / MONITORING AGENCY NAME(S) AND ADDRESS(ES) Air Force Office of Scientific Research Directorate of Aerospace Sciences Bolling Air Force Base, DC 20332-6448 Attention: Dr. Walter F. Jones		NA		
11. SUPPLEMENTARY NOTES Final Technical Report of Experimental and Modeling Research Conducted under AFOSR Support over the period 1/5/1991-31/1/1995				
12a. DISTRIBUTION / AVAILABILITY STATEMENT  <div style="border: 1px solid black; padding: 5px; width: fit-content;"> <b>DISTRIBUTION STATEMENT A</b>            Approved for public release            Distribution Unlimited         </div>		12b. DISTRIBUTION CODE <div style="border: 1px solid black; padding: 10px; text-align: center;"> <b>DTIC SELECTED</b>              NOV 20 1995  <b>F</b> </div>		
13. ABSTRACT (Maximum 200 words) Reaction bonded silicon nitride (RBSN) prepared from submicron size pure silicon powder is a micro-porous ceramic with excellent mechanical and dielectric properties for high temperature structural applications and for radomes. In this research program the mechanical properties including elastic moduli, tensile strength and fracture toughness of RBSN was experimentally studied in connection with its quasi-regular microstructure. The further ranges of microstructural features and the processes related to local fracture resistance were studied by means of two related and quite flexible computer simulations of the reaction kinetics controlling the microstructure and the processes that control the crack paths. These results are summarized and presented in greater detail in four appended manuscripts.				
14. SUBJECT TERMS		15. NUMBER OF PAGES 16. PRICE CODE		
17. SECURITY CLASSIFICATION OF REPORT Unclassified	18. SECURITY CLASSIFICATION OF THIS PAGE Unclassified	19. SECURITY CLASSIFICATION OF ABSTRACT Unclassified	20. LIMITATION OF ABSTRACT	

# MECHANICAL PROPERTIES OF POROUS HIGH TEMPERATURE STRUCTURAL MATERIALS: SOURCES OF TOUGHNESS IN REACTION BONDED SILICON NITRIDE

## 1.0 Introduction

In the production of high temperature ceramics by gaseous reaction bonding, as in the case of reaction bonded silicon nitride (RBSN), a material of quasi-homogenous porous microstructure is obtained with a porosity in the range of 0.2 - 0.3. A ceramic such as RBSN, prepared with no liquid phase sintering aids, has many attractive high temperature properties and physical characteristics. It is a candidate material for the structural components of the Advanced Turbine Systems with potential operating temperatures in the range of 1400C. With careful processing RBSN can be produced in near net shapes. In fully reacted form with a minimum of retained unreacted Si it has a low dielectric constant and exhibits low dielectric losses making it a very attractive material for radome applications. The special processing procedures of this material and its structural and dielectric properties that have been developed and explored under previous ARO and NASA support are summarized in Appendix A.

From a more generic point of view, RBSN of porosity in the range of 0.25, is a material nearly an order of magnitude more porous than the levels of porosity encountered in imperfectly sintered solids, but is very much denser than the usual cellular solids. While it has many microstructural characteristics common with materials on both sides of the porosity scale, RBSN requires different methodology for understanding of its mechanical properties. In the present case it was concluded that the attractive structural potential and other outstanding physical characteristics of RBSN would be difficult to exploit without fully understanding and improving its mechanical properties, and in particular its strength and fracture toughness. Thus, in the AFOSR program while considerable effort was directed to the processing aspects of RBSN from pure specially prepared Si powder, the main emphasis was on the understanding of its mechanical properties and particularly the factors that affect the fracture toughness. In this, a *complete cycle* approach was taken as a case study in the development of an advanced material *by design*. In the complete cycle approach to an attractive candidate material such as RBSN, the starting point is a detailed study of the

<input checked="checked" type="checkbox"/>
<input type="checkbox"/>
<input type="checkbox"/>

Availability Codes	
Dist	Avail and/or Special
A-1	

physical process beginning with the gaseous reaction processing, to the topology of the reaction induced microstructure and the characteristics of this microstructure that directly affect its strength and fracture toughness. This is followed by a detailed computer simulation of both the gaseous reaction process controlling the microstructure and the fracture paths that are taken by a crack through the resulting microstructure. When satisfactory congruity is established between the actual physical phenomenon of the observed structure property relation and that in the computer simulations, then, the latter is used to explore other possible structure property relations through the computer simulation to decide on new avenues for processing to improve properties.

## **2.0 The Material and Its Mechanical Properties**

The RBSN produced at M.I.T. is made from a pure silane-produced ( $\text{SiH}_4$ ) supply of perfectly spherical sub-micron size Si particles through a gaseous reaction process with  $\text{N}_2$  resulting in  $\text{Si}_3\text{N}_4$  with a quasi-homogeneously dispersed porosity of about 0.25. The pores have a size distribution ranging from roughly 70-700nm with aspect ratios in the range of 1.0-2.0. The individual grains in the microstructure, on the average, have a size roughly half that of the pores. A certain fraction of the pores are interconnected. Uncharacteristically large pores of large aspect ratio which could strongly reduce the strength are rare. There is x-ray line broadening evidence that there are short range reaction induced residual misfit stresses in the microstructure of a wave length roughly equal to the grain size. While the specific effect of these residual stresses has not been determined, they are likely to be a principal cause of the predominantly intergranular nature of the fracture in the RBSN.

The elastic properties of all RBSN samples of various porosities were measured by a laser pulse-echo technique with wave length much larger than the microstructural scale. The measured Young's moduli were predictably related to the porosity. The typical material has strength values in the range of 400MPa, with maximum values reaching as high as 870MPa. Fracture toughness, ranged from 2.2-2.8MPa  $\sqrt{\text{m}}$ . These fracture toughnesses have been obtained from fracture loads and estimates of fracture mirrors. In the course of the study a new method has been devised which is based on direct measurement of shapes of open cracks on the verge of propagation. These measurements which are considered more reliable

have resulted in somewhat lower values of fracture toughness. In such determinations of crack shapes some evidence of crack bridging by native heterogeneities in the microstructure has been found in addition to a direct correlation between crack plane tortuosity and level of fracture toughness. These measurements and features were taken as principal characteristics of the RBSN to be matched by simulations. The micro-structure of the MIT RBSN, its stereological description, and associated mechanical properties have been described in detail by Haubensak et al, (1995a) while the new method of fracture toughness determination has been described by Haubensak and Argon (1995). These manuscripts are attached as Appendixes B and C.

### **3.0 The Reaction Kinetics Simulation**

The first phase of the simulation involved devising a reaction kinetics model starting with spherical single crystal Si particles which become transformed into RBSN through a gaseous reaction with  $N_2$ . The reaction kinetics model has followed a cellular automata approach in 2-D, with some crucial topological input characteristic of 3-D features of the actual process.

The model starts by considering dense randomly packed spherical particles of constant size in space. The actual coordinates of particle centers and particle sizes for the 2-D model are obtained from a planar cut through this 3-D arrangement. The material fraction in the planar cut is then transcribed onto a hexagonally tessellated 2-D plane with mesh size roughly 0.1 that of the disk shaped particles. The surface sites of the circular particles are then assumed to fully communicate with an infinite supply of  $N_2$  and a stochastic gas phase reaction with an average rate proportional to the Si vapor pressure in the cavities. The overall conversion reaction is governed by the initial density of  $Si_3N_4$  nuclei on the surfaces, on the ratio of reaction rate to Si evaporation rate, and on the ratio of the Si evaporation rate to the re-condensation rate. Through the manipulation of these parameters and the incorporation of some surface smoothing by diffusion to control pore surface roughness, computer generated microstructures with features closely resembling those of the real microstructures were obtained. In this simulation a rare but regularly encountered feature was some uncharacteristically large, ill shaped pores, resulting from initial packing imperfections. These are expected to control the strength and are considered as an analogous feature to the

elongated crack like imperfections found in some experimentally produced microstructures described by Haubensak, et al (1995a). On the whole, the reaction kinetics simulation was successful in providing realistic rate constants for the overall reaction, for, the distribution of grain sizes and for the pore size and their aspect ratio distributions. An important observation of potential relevance for improvement of mechanical properties was the development of some interpenetrating elongated grains resulting from choosing anisotropic reaction directions. These were observed to result in stronger and tougher microstructures. This simulation has been described in detail by Haubensak et al (1995b) and is attached to this report as Appendix D.

#### **4.0 The Fracture Path Simulation**

The fracture path simulation was also performed in 2-D where the previously simulated microstructure is overlaid by a hexagonal network of nodal points connected by linear central force springs and angle flexing, so called, "watch springs" with spring constants chosen to obtain an exact match to the elastic properties of the isotropic RBSN. The nodes and the bond springs that fall into pore regions of the microstructure were assigned zero strength and zero stiffness, other bonds falling into the grain interiors of the solid matrix material were assigned a constant common stiffness, while those bonds traversing across grain boundaries were assigned only 0.75 of the strength of matrix bonds to mimic the intergranular fracture behavior of the real material. Quantitative evaluations were based on a bond-node-level stress tensor which has become widely used in simulations of heterogeneous solids.

Several levels of strength and toughness simulations were carried out with the model. In the first level, relatively large domains of typical porous microstructure were subjected to overall uniaxial tensile extension. At each level of externally imposed displacements, internal equilibrium was achieved by a conjugate gradient method of energy minimization. Typical loading sequences consisted of searching for the most highly stressed bond, releasing it, incrementing the border displacements to fracture the next highest stressed bond in the re-equilibrated structure, and so on, until the entire structure could no longer support load. From such simulations correlations between stiffness and peak strength of representative volume elements (RVE) were obtained.

In a higher level of simulation probing the crack growth resistance of such microstructures the entire field was homogenized in density but each hexagonal node and its environment were assigned a randomly selected pair of strength and stiffness values obtained from the above cell simulations of RVEs. Such continuum fields with random properties were then probed by cracks subjected to external Mode I fields, to note the distribution of local fracture toughness and the resulting tortuosity of the crack plane. Again, a reasonably close correspondence was obtained between the actual fracture toughness and crack plane tortuosities, and those simulated in the model. Various forms of microstructural variability were explored in the simulation. While interesting improvements for fracture toughness was found from uncorrelated increases in the variability of bond strength (with constant bond stiffness) as well as with bond stiffness (with constant bond strength), however, for the realistic cases where the strength and stiffness were correlated, increasing variability resulted in systematic degradation of toughness.

Finally, 3-D features in the local crack advance were approximated by the introduction of special elements that incorporated the average properties of a random sampling of three adjacent 2-D elements, as a first approximation of a typical element of a 3-D crack front. Simulations performed with such elements showed more realistic variations in local fracture toughness.

The entire set of simulations of fracture paths have been described by Haubensak et al (1995c) and is attached to this report as Appendix E.

## **5.0 Conclusions**

From such simulations of the microstructure and its relation to strength and fracture toughness, it was concluded that for microstructure, with quasi-random pore homogeneity, substantial improvement of toughness is not likely. Variation of grain aspect ratio and interpenetration of elongated grains did, however, result in considerable increases in fracture toughness. This suggests that attractive improvements in the fracture toughness of such porous solids like RBSN may still be possible through the incorporation of a randomly dispersed population of whiskers.

In any case the *complete cycle* approach to development of advanced materials *by design* where the coupling of the processing with property simulations is accomplished should give superior results.

## **6.0 Personnel Associated with the Research Program**

1. A.S. Argon, Principal Investigator, Quentin Berg Professor of Mechanical Engineering.
2. J.S. Haggerty, Co-Principal Investigator, Senior Research Scientist, Materials Processing Center.
3. V.V. Bulatov, Research Associate, Department of Mechanical Engineering (part time).
4. F.G. Haubensak, Research Assistant, Department of Materials Science and Engineering.
5. A. Lightfoot, Staff Researcher, Materials Processing Center (part time).
6. A. Seman, U. Callinan, Secretaries, Mechanical Engineering Department.

## **7.0 Technical Presentations**

1. A.S. Argon, "Interface Fracture and Toughness of Composites" Stanford University Seminar Lecture, Nov. 19, 1992.
2. A.S. Argon, "Controlling Toughness in Brittle Composites", Lawrence Livermore Laboratory Lecture, Nov. 6, 1992.
3. A.S. Argon, "Controlling Toughness in Brittle Composites", Invited lecture at the Institute of Mechanics and Materials Symposium entitled "Interfaces in Materials - Bridging the Length Scale Gap", La Jolla, CA, Sep. 12, 1993.
4. A.S. Argon, V.V. Bulatov, and F.G. Haubensak, "Simulation of the Microstructure and Fracture Paths of RBSN", Contributed presentation at the Pacific Rim Meeting of the American Ceramics Society, Honolulu, Hawaii, Nov. 8, 1993.
5. A.S. Argon, "Toughening Mechanisms in Brittle Solids", Materials Science Seminar Lecture at Cornell University, Nov. 17, 1993.
6. A.S. Argon, "Simulation of Crack Propagation Resistance in Brittle Media of High Porosity", Invited lecture at the AIME Symposium on High Temperature Materials in Chicago, IL, Oct. 3, 1994.

7. A.S. Argon, "Simulation of Crack Propagation Resistance in Brittle Media of High Porosity", Seminar lecture at the Colorado School of Mines, Nov. 18, 1994.
8. A.S. Argon, "Sources of Toughness in Reaction Bonded Silicon Nitride", Applied Mechanics Seminar lecture, Brown University, May 2, 1995.

## **8.0 Theses Completed**

Haubensak, F.G., "Microstructure Design of Porous Brittle Materials", Ph.D. Thesis, Department of Materials Science and Engineering, MIT September, 1994.

## **9.0 Publications**

1. Haubensak, F.G. , Lightfoot, A., Argon, A.S., and Haggerty, J.S., (1995a) "Reaction Bonded Porous Pure Silicon Nitride: Microstructure, Tensile Strength, Fracture Toughness", J. Materials Science, submitted for publication.
2. Haubensak, F.G., and Argon, A.S., (1995) "A New Method of Fracture Toughness Determination in Brittle Ceramics by Open Crack Shape Analysis", J. Materials Science, submitted for publication.
3. Haubensak, F.G., Bulatov, V.V., and Argon. A.S., (1995b) "A Simulation of the Reaction Bonding of  $\text{Si}_3\text{N}_4$  to Generate Porous Microstructures", J. Computer Aided Materials Design, submitted for publication.
4. Haubensak, F.G., Bulatov, V.V. and Argon, A.S., (1995c) "Simulation of Crack Propagation Resistance in Brittle Media of High Porosity", J. Computer Aided Materials Design, submitted for publication.



**Appendix A: Summary of Processing Details and Early Results on  
Dielectric and Mechanical Properties of Reaction Bonded Si<sub>3</sub>N<sub>4</sub>.  
(work performed under earlier ARO and NASA support)**

A two year program designed to develop high purity reaction bonded silicon nitride (RBSN) for hypersonic radome applications has been conducted by Raytheon Corporation and the Massachusetts Institute of Technology. The planned three-year program was terminated one year prematurely by funding restrictions.

The development program was initiated based on properties exhibited by laboratory scale RBSN samples made by MIT from semiconductor grade silane (SiH<sub>4</sub>). At the program's inception extraordinary strengths had been achieved (averages up to 592 MPa and individual samples up to 870 MPa) for a brittle material containing ~ 25% porosity. High temperature dielectric measurements of these RBSN samples at 35 GHz showed low losses up to 1200°C ( $\tan \delta < 10^{-2}$ ), low dielectric constants (~ 5.0) and low temperature coefficients. Net shape processing experiments demonstrated that nitrided parts exhibited dimensions within 0.1-0.2% of die dimensions.

The goal of this program was to develop a process for fabricating engineering shapes (radomes) from this material which retained the advantageous properties demonstrated with laboratory scale samples, and to acquire a data-base of mechanical, dielectric and thermal properties necessary for utilization of this material. Resulting properties were analyzed to determine their effect on permissible flight profiles.

Alternative forming techniques were evaluated in terms of satisfying the dimensional and quality requirements, and also in terms of matching existing industrial experience and equipment for forming large radomes. Considered processes included dry pressing, isostatic pressing, pressure slip casting, colloidal pressing, centrifugal casting, electrophoretic deposition, injection molding and bulk freeze injection molding. Laboratory scale experiments demonstrated the feasibility of all of these techniques (except for bulk freeze injection molding). Extensive nitriding kinetics experiments were conducted in parallel to insure that candidate binders, solvents and exposures did not inhibit complete conversion of the Si to Si<sub>3</sub>N<sub>4</sub> or leave residues, both of which are essential for meeting dielectric property

requirements. The combination of xylene as a solvent and polystyrene as a binder proved satisfactory in terms of nitriding rates, extent of conversion, residues and both safety and emission criteria. Powders dispersed in this solvent and binder combination were satisfactorily spray dried to form handleable powders. Based on a practical solvent and binder combination, a demonstrated powder pretreatment technique, prior radome forming experience, and existing industrial forming equipment, warm isopressing of spray dried powders was selected as the forming process.

Processing experiments were initiated at MIT. When satisfactory procedures were identified, duplicate samples were made at Raytheon. Extensive characterizations were used to demonstrate the equivalency of parts made in both laboratories. Mechanical and dielectric properties of laboratory scale samples made by warm isopressing were made to qualify the process and to begin optimization of process variables.

The strengths of the initial batch of samples made by warm forming spray dried Si powders averaged ~308 MPa. While less than the maximum values exhibited by optimized colloidally pressed samples based on alcohol solvents, these strengths were significantly higher than is exhibited by conventional RBSN (~100-200 MPa) and much higher than is exhibited by fused silica radome material (~48 MPa). Later generations of RBSN samples made by warm isopressing spray dried powders exhibited slightly improved strengths (335 MPa). Using the same binder and solvent, colloidally pressed samples exhibited average strengths of 539 MPa. These strength results for the two forming techniques, fractography and characterization of the spray dried powders indicate that strengths probably were controlled by relics of oversize particles that formed during spray drying. This program demonstrated that high strengths are achievable with the selected solvent and binder through uniformity of microstructure. Also, strength controlling defects can be removed by modifying the spray drying process and/or removing the oversize particles.

Initial high temperature dielectric measurements of several batches of warm isopressed RBSN by the Rockwell Science Center gave completely different results than the colloidally pressed sample they measured prior to the inception of the program. Resolving the cause of these anomalous results required assembly of an apparatus to make elevated temperature ( $T \leq 500^{\circ}\text{C}$ ) loss tangent measurements at Raytheon, many dielectric measurements and many

chemical analyses. Ultimately it was found that the high losses were caused by contamination from cements used to mount the samples at Rockwell. Subsequent measurements showed that all explored process conditions produced RBSN samples with loss tangents  $< 5 \times 10^{-3}$  for temperatures up to 500°C. Also important for radome applications, the dielectric constants were low (5.0-5.5) and relatively insensitive to temperature. This phase of the program demonstrated that improved dielectric properties were reliably achieved for RBSN made with the selected procedures. Although optimization and exploration of higher temperature properties could not be completed within the shortened program, all of the data indicates that acceptable loss tangents ( $\leq 10^{-2}$ ) can be retained for temperatures in excess of 1200°C.

Prototype scale samples were made to demonstrate the feasibility of making practical parts. Before making large parts, extensive nitriding kinetics experiments were undertaken to define firing schedules which avoided excess exothermic heating in large scale parts and which also yielded residual Si levels less than 0.1%. Using spray dried powders, and forming conditions defined with laboratory scale samples, two 12-inch long, 4-inch diameter, 3/16 inch wall cones were pressed and nitrided. Both of the as-formed green parts were crack free, dimensionally true and sound. After nitriding, both parts exhibited cracks and evidence of overheating. Irregularities were experienced with both nitriding runs since these represented the first two runs in a much larger scale furnace than had been used with all of the laboratory scale samples. Detailed comparisons indicated that differences in firing schedules and differences in atmospheres were responsible for the cracking. No evidence suggested that the problem was intrinsic.

Stress levels for a Patriot configured radome subjected to a PAC-3 flight profile were analyzed by Raytheon Missile Systems Division. Thermally and pressure induced stresses at the tip and the base of the radomes were determined. Material properties were based on measured and projected values for high purity RBSN made with the selected binders, solvents and nitriding schedules. It was found that the reduced modulus and relatively high thermal conductivity of the high purity RBSN resulted in reduced thermally-induced stress levels compared with fully dense  $\text{Si}_3\text{N}_4$ . Total induced stress levels were acceptable in terms of measured strengths.

Although, shortened, this program accomplished critical objectives. Forming techniques, binders, solvents, and nitriding schedules were identified which permitted large scale RBSN parts to be formed from high purity Si powders. The property levels exhibited by laboratory scale samples made with the selected procedures exhibited properties that essentially equaled the best levels achieved with processes designed to maximize properties without regard to practical considerations. These outstanding property levels will permit flight profiles that induce significantly higher stagnation temperatures than is permitted by other known materials. The elimination of machining steps should also result in much reduced production costs - not to mention avoiding machinery induced surface damage. Development to full scale appears practical and advantageous.

APPENDIX B. "Reaction Bonded Porous Pure Silicon Nitride:  
Microstructure, Tensile Strength, Fracture Toughness"

F.G. Haubensak, A. Lightfoot, A.S. Argon, and J.S. Haggerty,  
submitted to J. Materials Science.

# **Reaction Bonded Porous Pure Silicon Nitride: Microstructure, Tensile Strength, Fracture Toughness**

**F. Haubensak, A. Lightfoot, A.S. Argon\* and J.S. Haggerty  
Massachusetts Institute of Technology  
Cambridge, MA 02139**

## **Abstract**

Porous silicon nitride from high purity uniform sized spherical particles of sub-micron dimensions obtained by a gaseous reaction and resulting in material in an intermediate porosity regime of 0.2 - 0.3 was studied in considerable detail to establish connections between the porous microstructure and the principal mechanical properties such as Young's Modulus, tensile strength, and fracture toughness.

In the course of the investigation several new techniques of material characterization were developed which proved to be superior to what has been used in the past. These include a laser pulse-echo technique of determining the Young's Modulus, and a new method for determination of fracture toughness which relies on accurate measurements of the shape of cracks at impending states of propagation.

The present study and a pair of related computer simulations of the principal elements of the gaseous reaction that results in the porous microstructure and the modes of the crack propagation through such microstructures indicates that such materials with rather uniform porosity have a limited potential for development of tough material. Higher fracture toughness requires the introduction of new degrees of freedom that nurture crack deflection, development of associated redundant cracking, and crack bridging.

---

\* Author for correspondence.

## 1.0 INTRODUCTION

The cause-effect relationship between microstructure and mechanical properties of materials has been of interest for several decades. In particular, the characterization of the mechanical behavior of heterogeneous, and specifically, porous materials, has recently become of technological interest. Research has typically concentrated on materials with highly porous cellular microstructures [1] with relative densities as low as 0.3% and on materials with dilute porosity. For each extreme of porosity there are models of mechanical behavior with good predictive properties that are based on engineering assumptions about the microstructural morphology. In each case, extrapolations can be made to intermediate porosities with some limited success, however, there is a fundamental lack of understanding of behavior of materials within the intermediate range of porosities.

In the cases where the effects of porosity have been investigated, often the study relates to relatively isolated pores (and consequently low levels of porosity) acting as strength reducing defects. On the opposite end of the porosity spectrum, Gibson and Ashby [1] have assessed the field of cellular materials ( $p < 30\%$ ). These density trends in properties can be extended somewhat beyond their applicable range with reasonable results. In the intermediate porosity range, the mechanical properties of ceramics are often described in terms of an empirical exponential function of porosity. Figure 1 schematically illustrates the limits of intermediate porosity. Rice [2] has suggested that the fracture toughness and moduli of low porosity, brittle materials can be described by such an exponential formulation. While, these descriptive equations can be fitted to experimental data, they do not provide pertinent information for the improvement of properties through microstructural control.

Reaction bonded silicon nitride, developed specifically in the 1950s and 1960s in the search for high strength high temperature materials [3], is intrinsically porous. Loosely packed fine silicon particles heated at temperatures in the region of 1300C in a stream of flowing nitrogen were found to convert into porous silicon nitride with considerable strength. The significant processing economies of the low processing temperature of the reaction bonding process relative to standard sintering processes are apparent [4,5] when contrasted with processes that produce fully dense silicon nitride, such as including hot hydrostatic compaction in the processing steps or adding densification additives. The above

processing temperature is often lower than the target service operating temperature for high temperature diesel or gas-turbine engine hot zone components<sup>†</sup>. Nevertheless, these beneficial reaction kinetics allow for the incorporation of SiC whiskers with minimal interaction with the matrix and permit complete nitriding in less than 10 hours at 1400C [6]. In addition, in dynamic applications such as turbine blades, where the applied stress is linearly proportional to the mass of the material in motion, the inherent low density of porous materials translate into lower operating stresses. Another practical advantage is the fact that many reaction bonding processes have nearly negligible dimensional change during the reaction phase due to the fact that little or no densification by sintering occurs. Consequently, cracking associated with differential shrinkage is avoided, and the produced part will have very nearly the same size and shape as the precursor green body. This is an advantage if the produced part can be spared the final machining steps, which often introduce surface defects that are well known to weaken ceramic parts.

However, as a price for the above benefits, the final microstructure is left with a residual porosity. The consequence of this porosity, as a first order effect, is to reduce the modulus and fracture energy, both of which have been observed to be directly related to the volume fraction of porosity: the modulus goes to zero for an ideally random distribution of porosity at approximately 15%, the three dimensional elastic percolation limit<sup>‡</sup>, and the fracture energy is linearly proportional to the fracture surface area, which for a planar fracture surface implies a linear dependence on porosity. Thus, while mechanical properties are usually inferior at high porosities, materials have been produced that, on mass specific bases, have fracture properties that are comparable to fully dense materials [4]. There are some indications that the fracture energy could be significantly increased at higher porosities due to induced crack branching [7] and grain bridging as found in fully dense, heterogeneous material [8,9]. The RSBN produced at MIT with high purity sub-micron (0.3 $\mu$ m) diameter Si particles from laser-heated SiH<sub>4</sub> have shown unusually rapid nitriding rates at low temperatures, and the resulting strengths approach those of fully dense material [5].

---

<sup>†</sup> Gas inlet temperatures approach 1370C for engine designs suitable for trucks and automobiles[3]

<sup>‡</sup> The critical volume fraction at the percolation threshold for a variety of three dimensional lattices ranges from 0.143 to 0.163. Although the critical volume fraction in two dimensions based on continuum percolation considerations (exactly 0.5) cannot be extended directly to three dimensions, the conjecture that the critical volume fraction is comparable to the three dimensional packing of spheres ( $\approx 0.15$ ) is consistent with Monte Carlo computation (see Ziman, [10]).



Previous methods to determine small fracture toughness differences of RBSN in laboratory scale specimens, in order to better provide for material optimization, have proved to be less than conclusive.

Small variations in fracture toughness by standard methods were not detectable. Ball-on-ring strength testing and corresponding fractographic determination of the associated strength limiting flaw geometry proved to have some accuracy but was affected by the subjective nature of the measurements. While they serve as ready indicators of broad trends standard indentation fracture toughness techniques, do not have strong fundamental accuracy, and uncertainties associated with the sensitivity of the toughness measurement on the crack length dimension were found to be unacceptably large. To rectify these deficiencies, a technique based on stable crack growth from an internally pressurized hole in a disk shaped specimen through a wedging mechanism was developed, but stable crack growth could not be achieved in the stiffest materials. In this technique the load determination from the wedging crack opening mechanism usually suffered from load train relaxations at Hertzian contacts.

Nevertheless, an apparently significant difference in toughness in materials with nominally similar production history, was found, which was attributed to a possible microstructural parameter, such as particle size distribution, associated with the highly complex three dimensional microstructural space network. In the approach taken here to isolate the pertinent elements of microstructure design, the microstructure-property connection is studied experimentally with new or improved set of mechanical property testing procedures, while in a parallel pair of computer simulations the processes that control the microstructure [4] and the mechanisms that control the resulting fracture response [12] are modeled. Ideally, this approach is pursued until a close correspondence is reached with the actual experimentally probed system through a systematic variation of the available parameters that control the simulated microstructures. Once a proven cause-effect relationship is reached in the simulations that parallel the experimental one, it becomes possible in principle, to use the computer simulations to explore other microstructure-property connections and determine the possible benefits of pursuing new developments in processing to achieve such microstructures. This present communication discusses the results obtained for the connections between processing, microstructure and mechanical properties of the RBSN, produced by Haggerty and co-workers [6].

## 2.0 EXPERIMENTAL DETAILS

### 2.1 Production of Material

Reaction Bonded  $\text{Si}_3\text{N}_4$  samples were made from high purity Si powder synthesized from  $\text{CO}_2$  laser heated  $\text{SiH}_4$  [13]. The Si powder was colloiddally dispersed in octanol, pressed, dried and nitrided at 1400C in UHP  $\text{N}_2$ . Complete procedures for production have been described elsewhere [14].

### 2.2 Modulus Measurement

A convenient and effective way of measuring the average elastic properties of a heterogeneous solid of a small microstructure wave length is by acoustic means at a wave length much larger than the microstructure dimensions [15,16]. Such techniques can also be used to detect strength limiting flaws of dimensions much larger than the wave length of the acoustic probe [17-20].

In order to probe for important microstructural differences between samples the Young's Modulus was measured by an ultrasonic pulse-echo technique which lends itself well to the measurement of elastic properties of micro-porous material [21]. The experimental approach used here was to mount a thin specimen to a gold coated piezoelectric single crystal quartz transducer for acoustic transmission as depicted in Fig. 2. The optimal specimen thickness was 1mm, which is thick enough in relation to the wavelength of the acoustic pulse ( $\lambda = 200\mu\text{m}$ ), and thin enough so that minimal attenuation of the acoustic wave occurred and a plane wave condition was obeyed [22]. The volume of the material sampled was approximately  $5 \cdot 10^{-10} \text{m}^3$ .

The acoustic wave was generated by a laser pulse of 1-1.5mm diameter focused on the gold film which creates a well defined pressure pulse that is substantially planar [22,23]. The pressure pulse forms clear signals at entry into the sample and at exit, separated in time and that are clearly resolvable by the piezo electric transducer. In this way, the time of the transmission of the stress wave into the specimen, (and out of the transducer), and the time of return of the echo back into the transducer was obtained. The difference in time between

these two events is the time of travel of the acoustic wave through the thickness, reflection at the free surface and return to the specimen/transducer interface. The uniaxial strain wave velocity was thus obtained and is related to the Young' Modulus by:

$$E = (1+\nu)(1-2\nu)\rho v^2/(1-\nu) \quad (1)$$

where  $\rho$  is the material density,  $v$  is the wave velocity, and  $\nu$  is the Poisson's ratio.

### **2.3 Fracture Toughness Testing**

Fracture strength was measured using the biaxial ball-on-ring method [24,25]. In one method the fracture toughness was related to the strength and the observed, strength-controlling-flaw size [26], by curve fitting the critical flaw size and site stress data by examining the macroscopic fracture surfaces.

In a new and more accurate experimental technique the fracture toughness was determined by measuring the shape of the open crack associated with a Vickers micro-hardness indentation. The motivation for developing this technique was to obtain fracture toughness data of sufficient resolution to make a more precise connection with microstructural characteristics. Previous attempts to measure small variations in fracture toughness in certain RBSN specimens have proven unsuccessful with existing indentation crack length methods [27]. The new technique could be shown to correspond to accepted values for reference materials for which toughness values are known, and reveals variations in toughness previously too small to measure. This technique is described more fully in a separate communication [28], and is summarized in the Appendix.

### **2.4. Microscopy**

Microscopy of the RBSN microstructure involved standard grinding and lapping procedures down to 1 $\mu$ m diamond, which produced surfaces with many filled-in pores that were found to be resistant to ultrasonic cleaning. However, a final ion plasma etch for 30 minutes at 6kV removed sufficient material to reveal the microstructure down to the submicron pores. Stereo-imaging of the produced surface at 5000 magnification revealed a

nearly flat surface on a scale larger than the submicron pores, with a deviation from planar in a wave like form with a wave length of approximately 15 microns and an amplitude of 0.2 microns. This long wave length roughness is attributed to the combination of lapping and ion milling and was considered acceptable for the analyses of the pore features which are substantially smaller than this surface wavelength.

It was found that depositing a 30nm carbon coating allowed for good high voltage microscopy and resolution of sub-micron features. Due to the low atomic mass of carbon, the interaction with the electron beam is weak, and this layer is mostly penetrated by the high energy electron beam of 10-30kV accelerating voltage. Objects of 20nm dimension on such ion milled surfaces with C coating have been resolved with a high resolution field emission SEM (FESEM), and the point-to-point resolution of the images was found to be approximately 5nm. In contrast, for uncoated specimens of RBSN, the field emission SEM resolves 20nm features well with minimal charging at 2.0kV. An additional technique used for observing uncoated specimen surfaces was the environmental scanning electron microscope (ESEM). This microscope operates with 3 to 10 torr of water vapor pressure, which prevents excess charge buildup. In this manner, high accelerating voltages can be used to probe non-conducting specimens without standard coatings. Resolution obtainable with the ESEM is approximately 20nm. The additional feature the latter technique provides is the sampling of a sub-surface layer of material into which the high energy electron beam penetrates to a depth that is a function of the material properties. The same specimen surface imaged in the ESEM, without and with a 20nm Au coating is shown in Fig. 3. The uncoated image reveals a texturing of the contrast attributed to density fluctuations. These large pore channels have been observed previously [29].

In order to objectively determine approximate pore sizes and shapes in highly complex nano-scale microstructures, two complementary procedures of image analyses on metallurgically prepared surfaces were undertaken in parallel. Stereo images with SEM of the microstructure in the first case were hand edited to differentiate solid from pore. In the second case the images were digitized by an optical scanner and pore boundaries were determined by a contrast threshold criterion. In both cases the images were statistically analyzed with a numerical image analysis system. Pore size was measured by pore area and the dimensions of an equal area ellipse. The shape of the fitted ellipse was determined in such a way that maximum overlap occurred with the pore image. The pore aspect ratio

was characterized by the ratio of the major and minor axes of the equal area ellipse and the pore surface roughness was determined by the measured pore circumference,  $C$ , normalized by the circumference of the equivalent area circle,  $C/2\sqrt{\pi A}$ , where  $A$  is the pore area. The circumference was measured at a resolution of 8.5nm.

In addition, fracture paths were studied in 120 micron thick TEM specimen blanks indented with a 1kg Vickers indenter before impregnating with epoxy. Microscopy was performed on an Akashi EM002B microscope. More detailed description of the microscopy procedure is given elsewhere [26].

## **2.5 X-ray Diffraction Experiments**

Ground samples of 9 micron thickness with 1 micron finish in as-nitrided states were used to analyse the interior and exterior regions of the RBSN pellets. The fraction of unreacted Si the alpha/beta ratio, grain size, lattice parameter and lattice distortion were determined in this manner [26]. Lattice distortion can originate from many sources, including localized defects and microstrains; they should be considered separate from changes in the mean lattice parameter values, which result from long range macro-residual stresses.

## **3.0 EXPERIMENTAL RESULTS**

### **3.1 Microstructure**

The bulk density in the final nitrided samples ranged from 69.5% to 83% of the theoretical value. The percent conversion to nitride was determined by x-ray diffraction, and by weight gain. It was between 97-100% [30], and was uniform throughout the specimens, within 2%. The grain sizes as observed by TEM and x-ray diffraction were between 45 and 114 nm respectively. Lattice distortion, by x-ray line broadening, was determined to be approximately between 0.2 and 0.15%. Processing histories for specific samples can be found in Table 2.

Figure 4 shows a typical microstructure of porous RBSN produced by Haggerty and co-workers [6]. The pores appear somewhat equiaxed with relatively smooth surfaces

indicating that during the formation of the RBSN there is a finite amount of time for some smoothing of the surfaces by diffusion. The pore size distribution in the typical microstructure is usually narrow, and is in the range of 50-300nm, as shown in Fig. 5. Pore aspect ratios were found to range between 1 and 4, and pore circumferences normalized with that of the equal area circle range between 1 and 2, as shown in Fig. 6. These measures reinforce the qualitative observations of a relatively homogeneous, equiaxed porosity with smooth surfaces. As can be seen in Figs. 7a and 7b a comparison of pore size distributions as determined by the major axis of the equal area ellipse, between the method of manually edited micrographs and that obtained by a digital contrast threshold method revealed no significant differences in average dimension and distribution of pore size. Manual editing produced fewer pores with diameter less than 50nm, since such pores at  $2 \times 10^4$  magnification are below the threshold of visual detection. All measured pore size distributions over the porosity range of 18 to 30% were alike within experimental error, with variations arising only from limited sample size, as seen in Figs. 5a and 5b for the two extremes in porosity. In a few instances a separate population of pore channels was found (see Table I). These pore channels shown in Fig. 8, appear as high aspect ratio features of approximately 200nm width and typically more than 1 micron length, and form an apparent cell-like network with a periodic length scale of approximately 2-5microns. In addition, the difference in area fraction of micron size pores observable between two nominally identically processed materials: i.e., one with the elongated pore population (specimen G) and the other with quasi-homogeneously distributed equiaxed pores (specimen H) suggests that the volume fraction of these elongated pore channels is approximately 7%. Line profile height measurements of the sectioned surface revealed that 5% of the surface sampled was a large dimension pore. Profilometry measurements were also performed by a scanning laser confocal microscope which has a height resolution of 0.25 $\mu$ m and a vertical resolution of 1 $\mu$ m. Qualitative observation suggests that at least some of the elongated pores are interconnected, providing easy fracture paths.

*A paragraph discussing determination of porosity by porosimetry and internal pore surface and pore connectivity determination by gas permeation should come in here.*

### 3.2 Modulus

As expected the modulus was inversely dependent on the average porosity as is shown in Fig. 9. In the case where the microstructure included a population of elongated pores, this tended to produce a lower modulus, due to the interconnected pore channels. The dependence of modulus on average porosity is expected. This microstructural morphology and its connection with the modulus over the range of porosity mirrors the result obtained from the quantitative microstructure analysis described above. The dependence of the measured moduli on porosity are compared in Fig. 9 with the Eshelby inclusion model of Chow [31] and the self consistent model of Budiansky [32]. The data with its characteristic scatter falls somewhere in between these models. The degree of agreement of the data with the models reinforces the notion of a quasi random, low aspect ratio pore population of roughly uniform dimensions.

Describing the effect of porosity by the empirical exponential curve fit of  $E = E_0 \exp(-bp)$  where  $E_0$  is the modulus of the fully dense material and  $p$  is porosity, requires for the best fit  $b = 2.23 \pm 0.17$  as compared to published values for many varieties of silicon nitride of  $2.4 \pm 0.4$  [33], and 3.7 for a variety of reaction sintered silicon nitrides [34]. This relatively low value of  $b$ , as compared to the range of values of 1.7 to 6.6, in which the large majority of polycrystalline materials fall, implies that for the isotropic RBSN, the elastic properties cannot be substantially increased.<sup>8</sup>

The uncertainty for measured values of  $E$  with this technique is estimated to be 4%, and is associated with obtaining a uniform thickness specimen and measuring this dimension.

### 3.3 Tensile Strength

Tensile strengths of RBSN with porosity ranging from 17 to 27% were between 592 to 308 Mpa, respectively.

---

<sup>8</sup> A lower value of  $b$  implies less dependence on the average porosity

### 3.4 Fracture Toughness

Fracture toughness determination through post-failure fractographic measurement of strength controlling flaw size produced fracture toughness values in the range of 1.65 to 2.7  $\text{Mpa}\sqrt{\text{m}}$ . The subjective nature of determination of flaw size however, limits the accuracy of this method.

The alternate method of measurement of fracture toughness, by determining the shapes of open cracks under load [28] produced somewhat smaller values of fracture toughness when compared with values obtained by the method based on flaw size measurements. The values ranged from 0.93 to 1.97  $\text{Mpa}\sqrt{\text{m}}$  and scale fairly strongly with average porosity, as is shown in Fig. 10. The few cases at the highest levels of porosity exhibited toughness and energy release rates comparable or larger than values of material with substantially less porosity as is shown in Figs. 10 and 11. These highest porosity microstructures exhibited evidence of increased complexity in crack path in comparison with the largely planar character of cracks in the lower porosity materials. The fracture path micrograph of Fig. 12 shows some evidence of crack bridging behavior, on a length scale of the order of the particle diameter in the green body, implying some connection with packing defects.

### 4.0 DISCUSSION

The microstructures of the RBSN presented here have a high degree of uniformity based on microscopy observations and the relatively small scatter in the elastic modulus data. In addition, the similarity of pore size distributions over the porosity range implies a degree of qualitative similarity in microstructural features. While the average pore diameter is related to the initial Si particle diameter, i.e., between 200 and 300nm, the pore size distribution based on stereological measurement performed on planar sections, shows that the microstructure consists of many very small pores less than 100nm. These small pores, quite likely, correspond to bottleneck configurations between larger pores and appear to have little consequence on the overall mechanical properties, as evidenced by the highly planar character of the typical fracture paths.

Microstructural homogeneity was found frequently except in the few cases where pores existed on a scale substantially larger than the average intrinsic pore size. The processing



steps which produced these defects could not be identified. However, the length scale of the pores which is much larger than the initial silicon particle size suggests that the source of inhomogeneity is associated with particle packing defects or stress relief cracks, and may provide a low resistance crack propagation path. These materials indeed exhibited lower strength and toughness.

The grain size, as determined in two representative samples, was found to be approximately one half of the average pore diameter, thus grain boundary surface area is comparable with pore surface area at these relatively high porosities. This result is consistent with the fact that the fracture paths were observed to be predominantly intergranular from observations of indentation cracks viewed by TEM. This could be due to either weaker grain boundaries or due to grain level internal stresses of misfit. The fact that the latter may be important and that they may have a wavelength larger than the grain size might be implied by the apparent stress relief cracks observable in some microstructures.

The monotonic decrease of elastic modulus with average porosity is not fully paralleled by the decrease of fracture toughness and energy release rate. The highly planar character of the fracture paths, especially at low porosity, highlights the small consequence of the pore configurations, and the relative importance of the average porosity level. At the highest porosity levels ( $p = 30\%$ ), the observed increased crack complexity and bridging differs markedly from a planar section probe of the microstructure, and is paralleled by an increased fracture toughness.

The simulation of fracture paths in similar porous microstructures [12] illustrates some of the results already outlined. Highly uniform microstructures have little potential for harnessing toughening mechanisms such as crack tip shieldings by redundant cracking, crack bridging or crack deflection. However, in such simulations it was found that increasing local material variability in terms of strength and stiffness variation in the porous material on the scale of the typical distances of coherent crack advance such as the grain size, which was found to increase the crack complexity and associated toughness. In addition, increased microstructural variability in terms of strength and stiffness was found to arise from increasing amounts of porosity on length scales equivalent to a small multiple of the pore dimensions. The 2-D porosity level for optimal strength variability occurs

within the range of 10-30%. Less porosity corresponds to low material variability and high porosity implies high variability and overall material weakening. However, in view of the fact that material strength and stiffness correlate strongly\*\* and was found to significantly reduce crack complexity, it is likely that increased crack complexity may be found at porosity levels higher than those observed here.

New directions for further improvement of toughness include investigating the specific details of the increase in crack complexity at high porosity levels. Clearly, at levels of quasi-random porosity less than the 3-D elastic percolation limit, small interaction between pores will generate fracture behavior appropriate for dilute porosity such as planar fracture and average sampling of material. At the highest levels of porosity studied here, when porosity can no longer be randomly distributed the crack complexity was found to be only marginally greater than that in material with planar fracture paths. Therefore, a further increase in porosity with a qualitatively similar microstructure morphology, may reveal significantly higher amounts of crack complexity, such as, roughness and bridging. The increase in crack tip shielding effects at higher porosities, however, must out-weigh the reduction in available solid fracture surface area and average elastic modulus. These trends illustrate the competition between the increase in toughness due to higher variability in strength and stiffness at higher porosity and the reduction in toughness due to the reduction of the elastic and strength properties with increasing porosity.

---

\*\* A control microstructure in the simulation deemed to have characteristics of the real RBSN exhibited strength and stiffness variation of material elements on the scale of a multiple of the pore size. These variations were correlated by the two variable correlation parameter,  $\chi = 0.85$ . Although a high correlation of strength and stiffness through porosity, for crack tip material elements was generally found, the dependence was weakened at higher porosities. The implication is that increased material variability at higher porosity produces a de-coupling of local strength and stiffness, and results in comparatively higher crack complexity and toughness.

Other possible avenues of potential toughness improvement, as suggested by the above mentioned simulation results, involve exploring higher variability microstructures. Material variability contributions were found to arise in simulated fracture with the introduction of grain boundary strength less than the bulk matrix strength, suggesting grain boundary strength tailoring. Other potential sources of increased material variability include thermal mismatch residual stresses and elastic anisotropies which are considered as effective heterogeneities in the nucleation of microcracks stimulated by the main crack. Other typical toughening mechanisms such as crack wake bridging suggest higher grain aspect ratio with random principal directions and the incorporation of whiskers.

## **5.0 CONCLUSIONS**

The high degree of homogeneity of microstructures of RBSN on scales larger than the average sub-micron pores and the generally planar character of the observed fracture paths implies that the likelihood of obtaining significantly improved fracture toughness is not high in material with such quasi-homogeneous microstructures. At the highest levels of porosity observed in this study (30%) increased crack complexity and toughness was in evidence. Higher levels of porosity have the potential for increased levels of fracture energy, as has been found by Rice et al [7], and was noted in fracture path simulations [12]. Higher porosity and other factors such as grain boundary strength tailoring, was found to provide increased variability and increased crack complexity and toughness.

## **Acknowledgment**

This research has been supported by the AFOSR under Grant AFOSR-91-0263C. For this support we are grateful to Drs. G. Haritos and W. Jones of that agency.

## REFERENCES

1. L.J. Gibson and M.F. Ashby, *Cellular Solids, Structure and Properties*, Pergamon Press: Oxford (1988).
2. R.W. Rice, *J.Am. Ceram. Soc.*, **59**, 536, (1976).
3. F.L. Riley, *Materials Science Forum*, **47**, 70 (1989).
4. J.E. Ritter, S.V. Nair, P.A. Gennari, J.S. Haggerty, and G.J. Garvey, *Advanced Ceramic Materials*, **3**, 413 (1988).
5. J.S. Haggerty, A. Lightfoot, J.E. Ritter, P.A. Gennari, and S.V. Nair, *J. Am. Ceram. Soc.*, **72**, 1675 (1989).
6. B.W. Sheldon and J.S. Haggerty, "The Formation of Reaction Bonded Si<sub>3</sub>N<sub>4</sub> at Low Temperatures and in Short Times" *Proc. 13th Annual Conference on Composites and Advanced Ceramics, Engineering Ceramics Division Meeting, American Ceramic Society, Cocoa Beach, FL, January 1989*.
7. R.W. Rice, K.R. McKinney, C. Cm. Wu, and S.W. Freiman, *J.Mat. Sci.*, **20**, 1392 (1985).
8. P.L. Swanson, C.J. Fairbanks, B.R. Lawn, Y. Mai, and B.J. Hockey, *J. Am. Ceram. Soc.*, **70**, 279, (1987).
9. J. Rodel, *J. Eur. Cer. Soc.*, **9**, 323 (1992).
10. J.M. Ziman, "Models of Disorder", Cambridge University Press: Cambridge, (1979).
11. F.G. Haubensak, V.V. Bulatov, and A.S. Argon, "Computer Aided Materials Design", submitted for publication.
12. F.G. Haubensak, V.V. Bulatov, and A.S. Argon, "Computer Aided Materials Design", submitted for publication.
13. W.R. Cannon, S.C. Danforth, J.H. Flint, J.S. Haggerty, and R.A. Marra, *J. Am. Ceram. Soc.* **65**, 324 (1982).
14. A. Lightfoot, H.L. Ker, J.S. Haggerty, and J.E. Ritter, *Ceram Eng. and Sci. Proc.*, **11**, 842 (1990).
15. E.A. Dean, *J. Am. Ceram. Soc.*, **66**, 847 (1983).
16. W.A. Fate, *J. Appl. Phys.*, **46**, 2375 (1975).
17. M.A. Biot, *The Journal of the Acoustic Society of America*, **28**, 168 (1956).
18. H.E. Bommel and K. Dransfeld, *Phys. Rev. Letters*, **2**, 298 (1959).
19. B.R. Tittmann and H.E. Bommel, *Rev. Sci. Instruments*, **39**, 614 (1968).

20. R.G.F. Taylor and A.J. Pointon, *Contemp. Phys.*, **10**, 159 (1969).
21. E.A. Dean. Elastic moduli of porous sintered materials.
22. L.C. Lev and A.S. Argon, *Ceram. Eng. and Sci. Proc.*, **18**, 743, (1994).
23. L.C. Lev and A.S. Argon, *J. Appl. Phys.*, submitted for publication.
24. D.K. Shetty, A.R. Rosenfield, P. McGuire, G.K. Bansal, and W.H. Duckworth, *Am. Cer. Soc. Bull.* **59**, 1193, ( )
25. S.V. Nair, Z.Q. Cai, J.E. Ritter, A. Lightfoot, and J.S. Haggerty, Mechanical Behavior of SiC Particulate Reinforced RBSN Matrix Composites, *Proceedings of 16th Annual Conference on Composites and Advanced Ceramics, American Ceramic Society, Cocoa Beach, FL, January, 1992.*
26. A. Lightfoot, J. Sigalovsky, and J.S. Haggerty, *J. Am. Ceram. Soc.*, submitted for publication.
27. S.V. Nair, Z.Q. Cai, J.E. Ritter, A. Lightfoot, and J.S. Haggerty, Indentation Residual Stresses in RBSN and RBSN Composites, *Proc. 16th Annual Conf. on Composites and Advanced Ceramics, American Ceramic Society, Cocoa Beach, FL, January 1992.*
28. F.G. Haubensak and A.S. Argon, *J. Mater. Sci.*, submitted for publication.
29. A. Lightfoot, J. Sigalovsky, and J.S. Haggerty, Relationship between Toughness and Microstructure of Reaction Bonded Silicon Nitride, *16th Annual Conference on Composites and Advanced Ceramics, American Ceramic Society, Cocoa Beach, FL, January, 1992.*
30. A. Lightfoot, H.L. Ker, and J.S. Haggerty, Properties of RBSN and RBSN-SiC Composites. *Proceedings of the 14th Annual Conference on Composites and Advanced Ceramics, Engineering Ceramics Division Meeting, American Ceramic Society, Cocoa Beach, FL, January 1990.*
31. T.S. Chow, *Journal of Polymer Science: (Polymer Physics Edition)*, **16**, 959 (1978).
32. B. Budiansky, *J. Mech. Phys. Solids.*, **13**, 223 (1965).
33. R.W. Rice, "Treatise on Materials Science and Technology", Vol. II, page 199, Academic Press, New York., (1977).
34. R.W. Rice, K.R. McKinney, C.Cm. Wu, and S.W. Freiman, *J. Mat. Sci.*, **20**, 1392 (1985).
35. I.J. McColm, "Ceramic Hardness", Plenum Press: New York (1990).

**Table I. Summary of Elastic Properties and Pore Shape**

<b>Specimen</b>	<b>Young's Modulus</b>	<b>Pore Channels</b>
A	135 GPa	no
B	157 GPa	yes
C	149 GPa	yes
D	169 GPa	no
E	161 GPa	no
F	168 GPa	no
G	164 GPa	yes
H	193 GPa	no
I	175 GPa	no
J	182 GPa	no
K	193 GPa	no
L	185 GPa	no
M	215 GPa	yes
N	182 GPa	no

Table II. Summary of Key Processing Descriptions of Specific RBSN Material

Material	Processing History	porosity, p
K	Octanol w/o CIP	22.0%
H	Octanol w/o CIP	23.9
G	Octanol w/o CIP	25.5
D	Octanol w/o CIP	26.9
E	Octanol w/o CIP	25.8
I	Octanol w/o CIP	23.1
J	Methanol w/o CIP	23.0
L	Methanol w/CIP	19.1
N	Methanol w/CIP-oxidized at 1000°C, 1hr	23.0
M	6-8% polysilazane binder	17.0
C	1.5% polystyrene binder, colloidal pressed	27.0
F	1.5% polystyrene binder, colloidal pressed	25.8
A	5% polystyrene binder, warm isopressed	30.5
B	5% polystyrene binder, warm isopressed	29.0

## **Appendix    Fracture Toughness Determination through Measurement of Open Crack Spaces.**

The stress state at the crack tip of Vickers indentation induced cracks is obtainable from the gradient of separation between the crack faces as a function of distance from the crack tip [28]. Thus, the accuracy of this method relies on the fundamental connection between observable open crack shape on the verge of propagation and the critical crack tip stress intensity. Through relating computed crack shapes obtained by finite element solutions for boundary loading conditions appropriate to the indentation process, to open crack shapes determined by SEM, it was possible to obtain high quality data for the fracture toughness.

Figure 13 shows the open crack displacements  $\Delta v$  for a specific case of a Vickers indentation crack along the length of the crack, fitted against a matching finite element solution for a control experiment on soda lime glass. The fracture toughness determined by the fit was  $K_{IC} = 0.55 \text{ MPa}\sqrt{\text{m}}$ .

The implementation of the measurement technique involves the preparation of the surface for microscopy, the indentation of the surface with the Vickers microhardness technique [35] and generation of high resolution micrographs of the shapes of the produced cracks.

Prior to indentation, a standard gold coating used regularly in SEM, is applied for the purpose of obtaining optimal resolution. Indentations are made with a standard Vickers microhardness apparatus with loads ranging from 2 to 10N. The choice of load is important to the generation of radial cracks which are large enough for observation. However, care must be taken not to exceed the load for which a profusion of other cracks are produced. The load is held for 20 seconds, and removed. Microscopy was performed within several minutes of indentation, and with sufficient resolution to clearly delineate the crack edges.

Open crack shapes are obtained directly from the micrographs with standard micrometer measurements. Care was taken to estimate the uncertainty of open crack flank separation measurement by providing upper and lower bounds, as observed from the micrographs. The upper and lower bounds were determined by the uniformity of the contrast gradients. The technique pre-supposes that the indentation crack is kept open by fracture debris pressed into the crack by the indent and that crack closing is negligible.



Nevertheless, due to this assumption the reported fracture toughness values are considered to be under estimates.

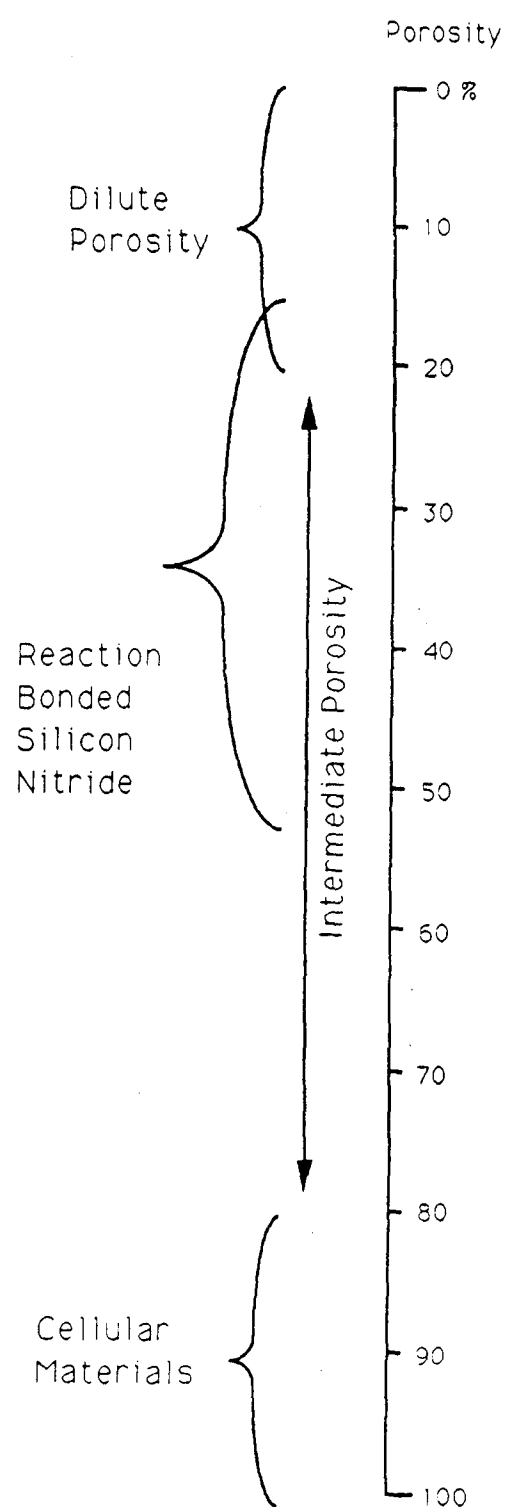
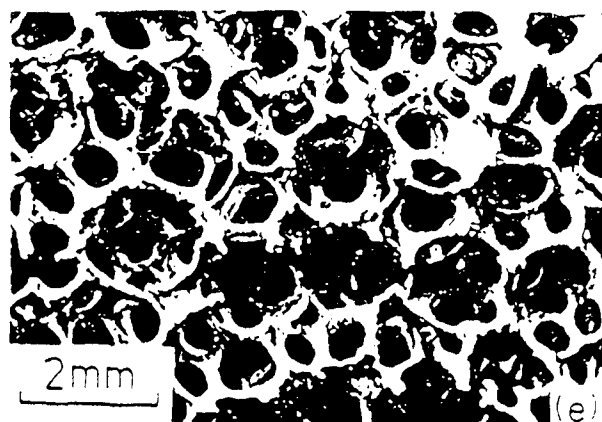
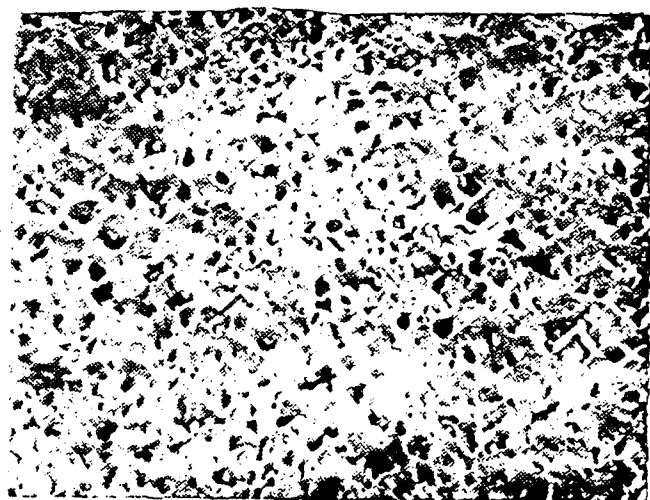
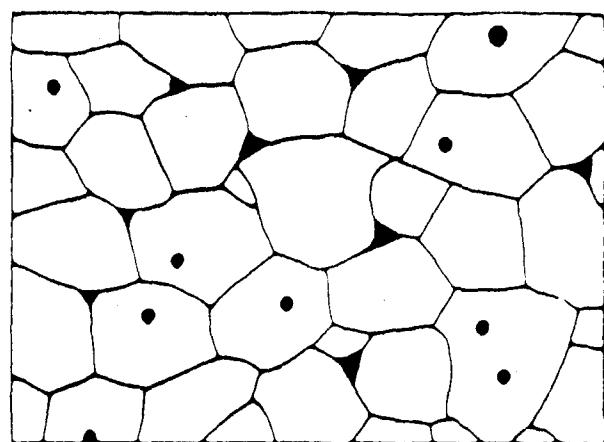


Figure 1 Material classification based upon average porosity.

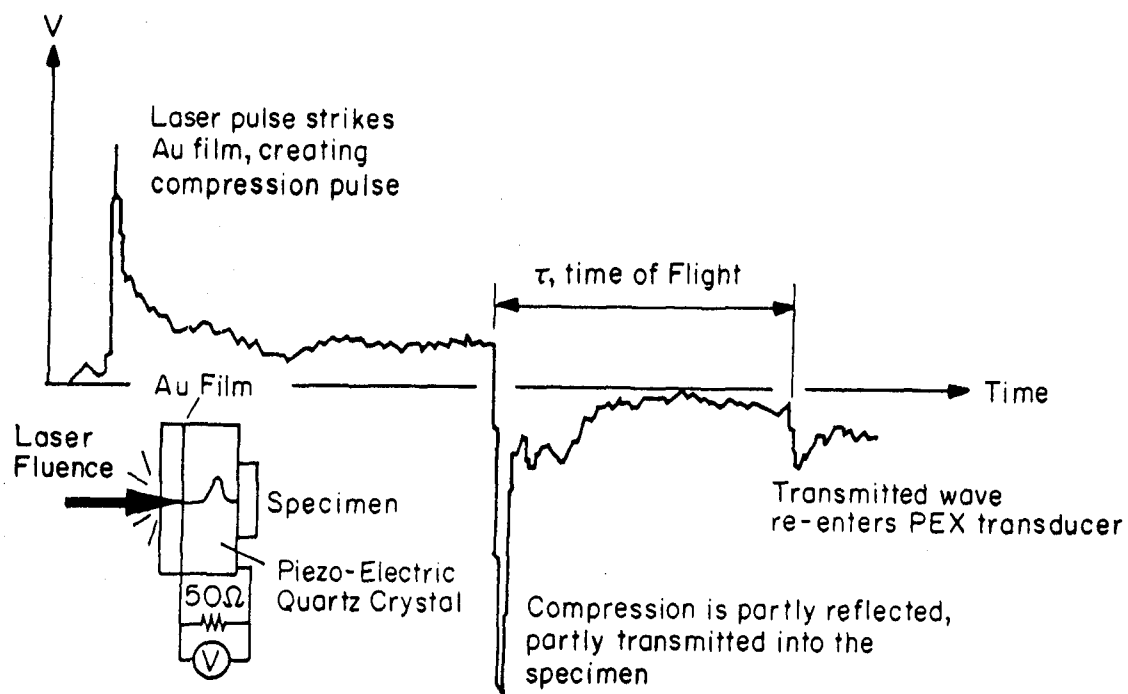


Fig.2. The pulse-echo method of modulus measurement by means of a piezo electric transducer.

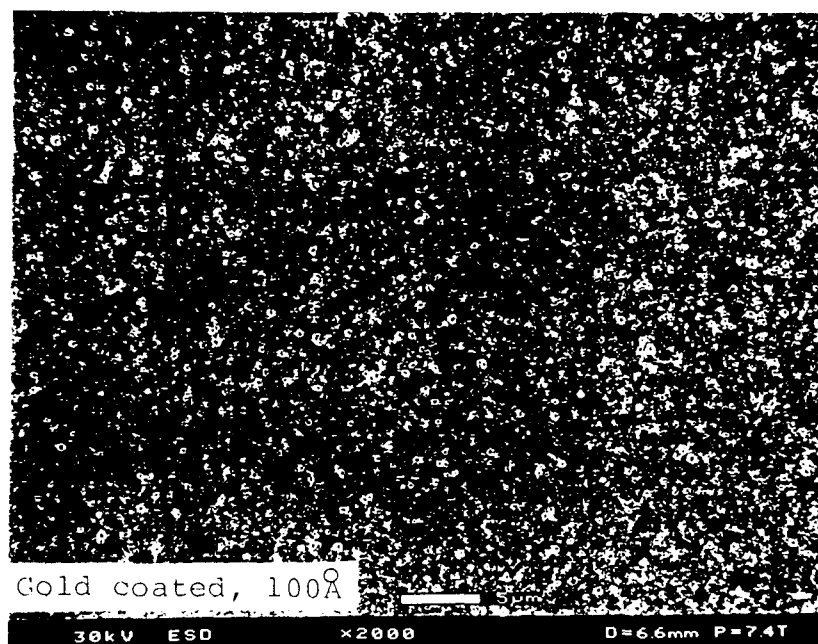
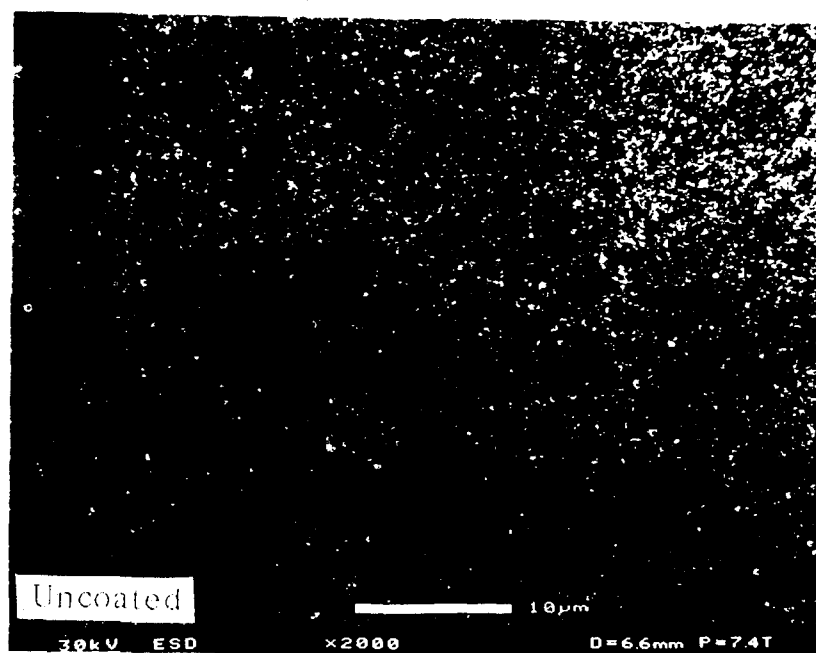


Fig.3. Material C observed in the SEM with an uncoated surface (a); and with a surface coated with a 20nm Au film (b).

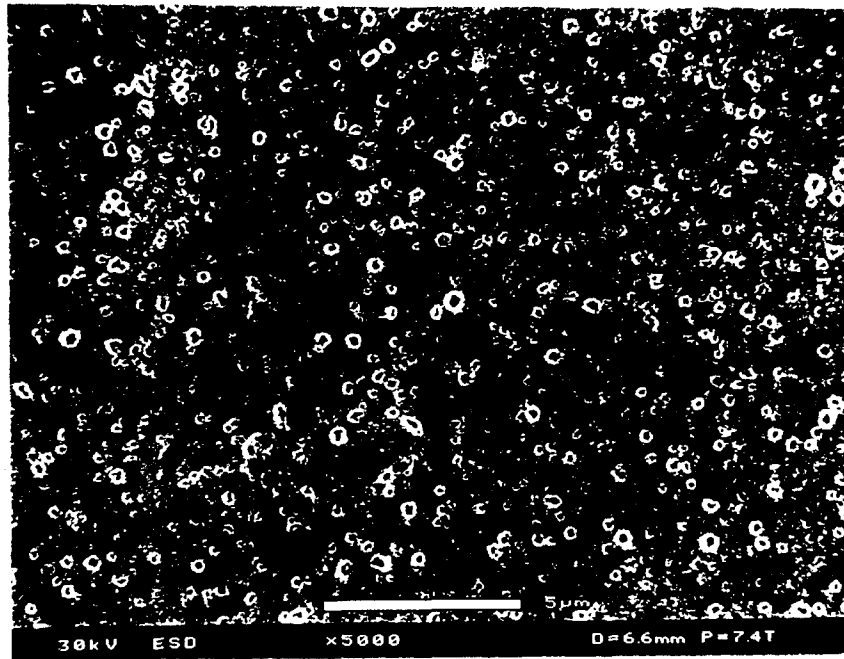


Fig.4. Typical microstructure of RBSN showing quasi-uniformly distributed submicron pores.

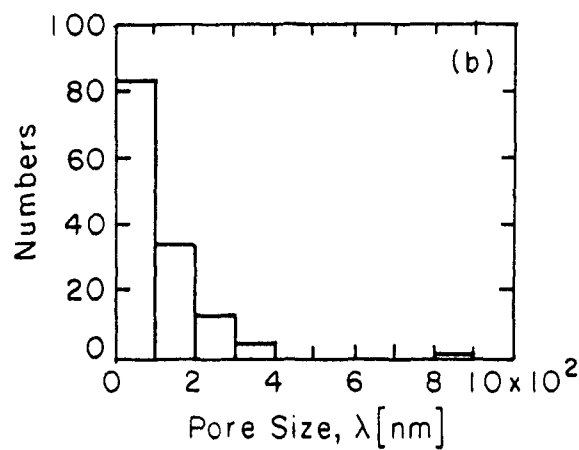
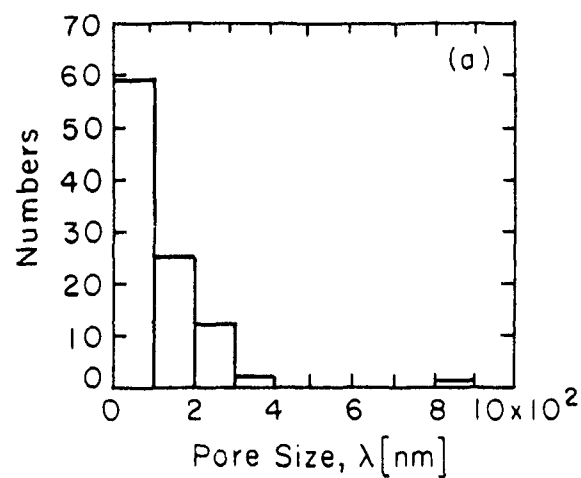


Fig.5. Two typical examples of pore size distribution in materials on the extremes of the porosity range: (a) material M with 18% porosity; (b) material A with 30.5% porosity.

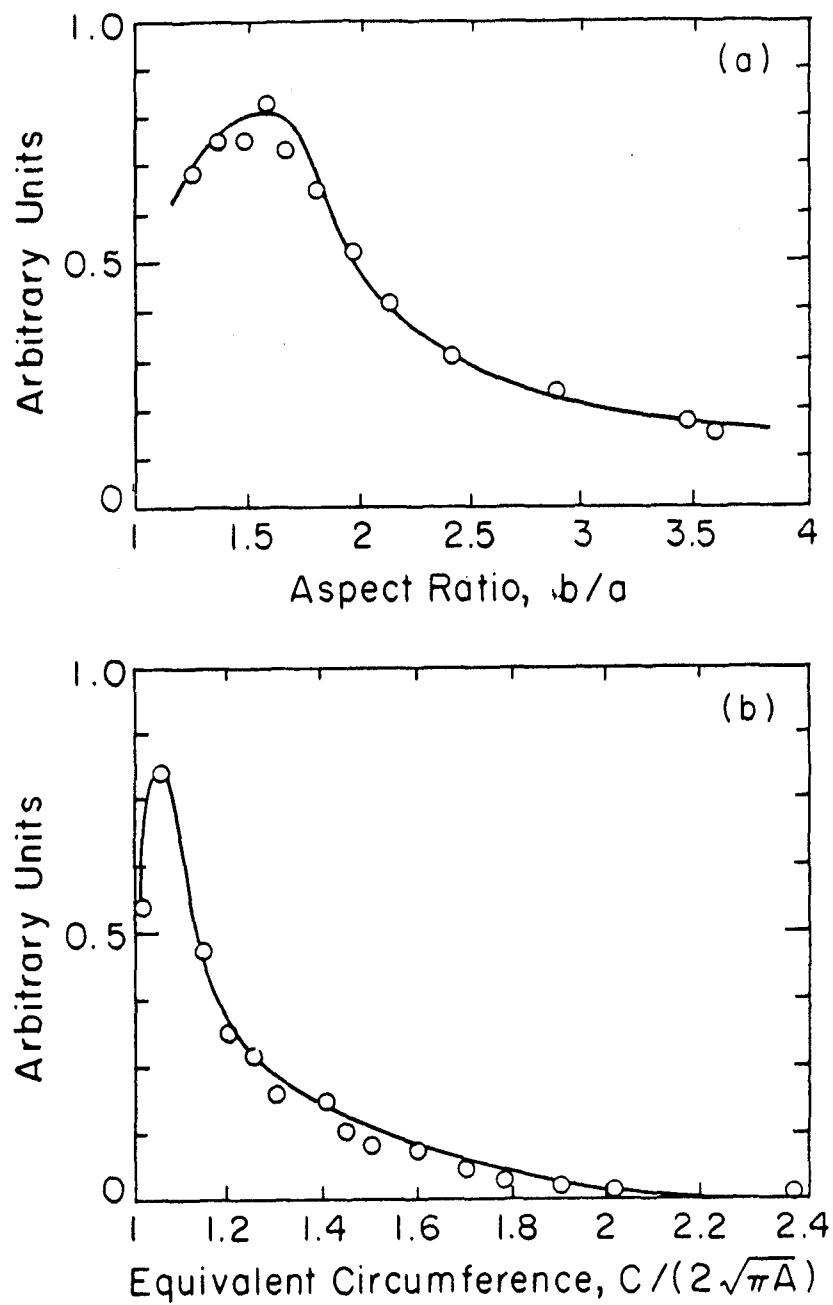
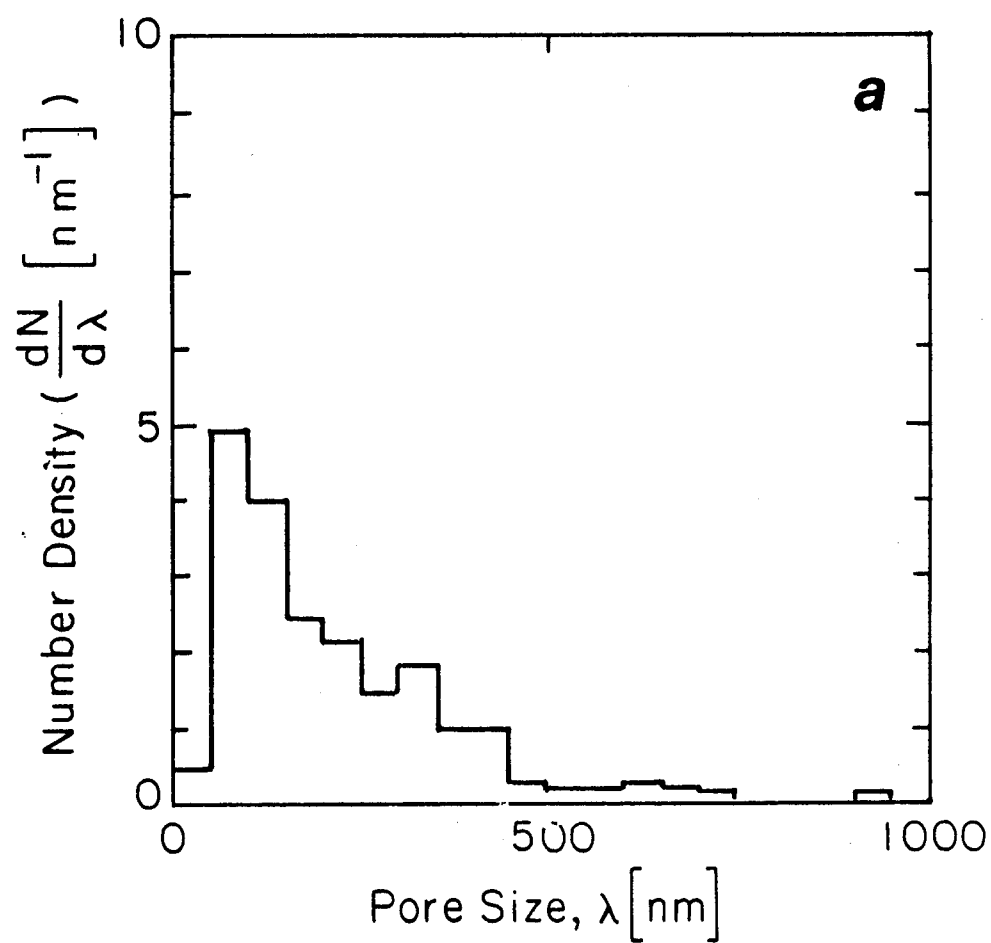
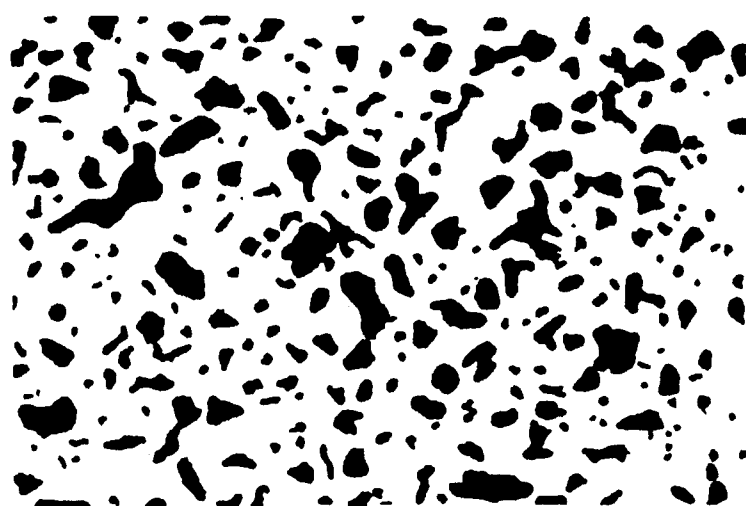


Fig.6. Typical distributions of pore aspect ratio (a); and pore circumference normalized with the circumference of a circle with equal area. (b).





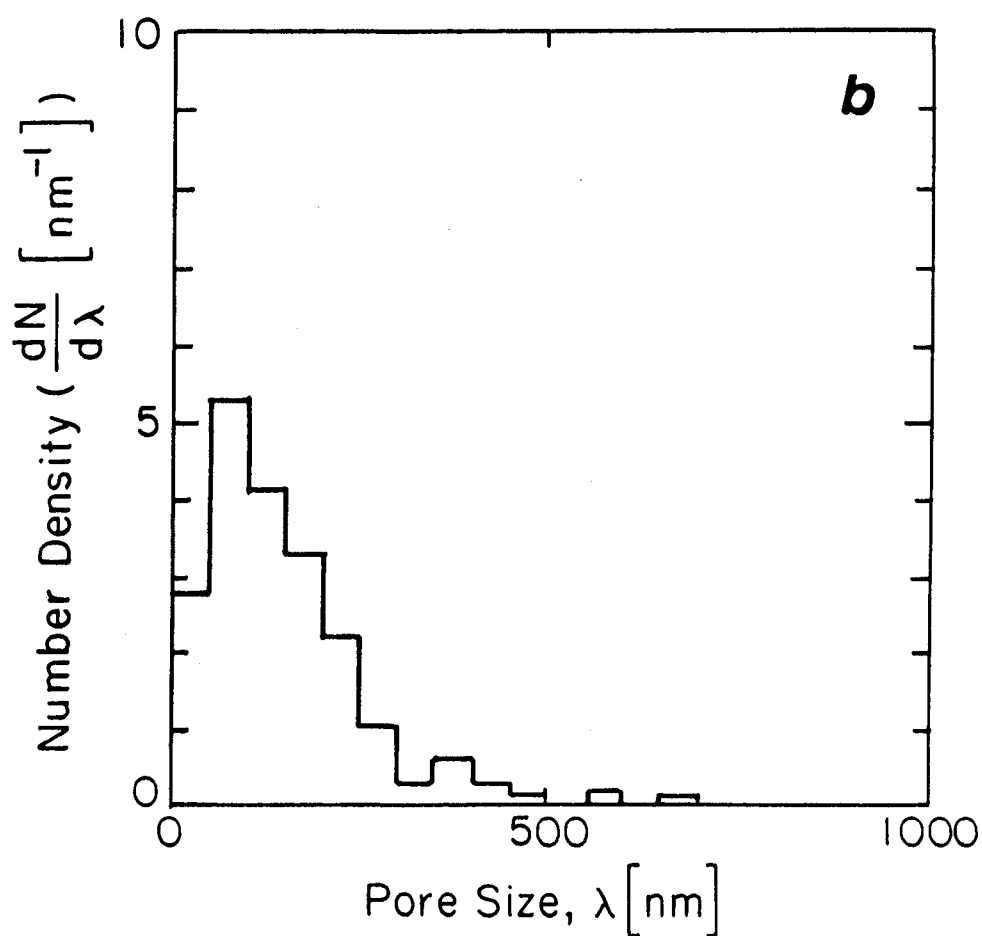
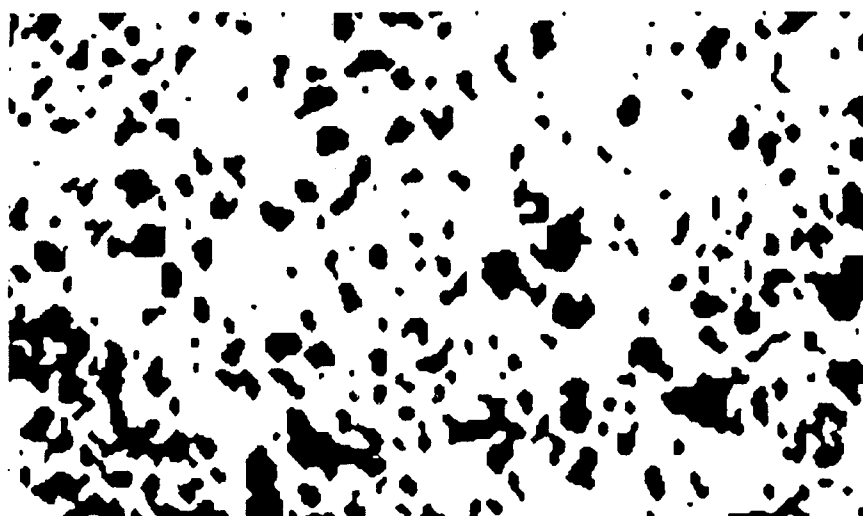


Fig. 7. Comparison of methods for determination of pore characteristics: (a) porosity characterized from manually edited micrographs; (b) porosity characterized by automated image analyses.

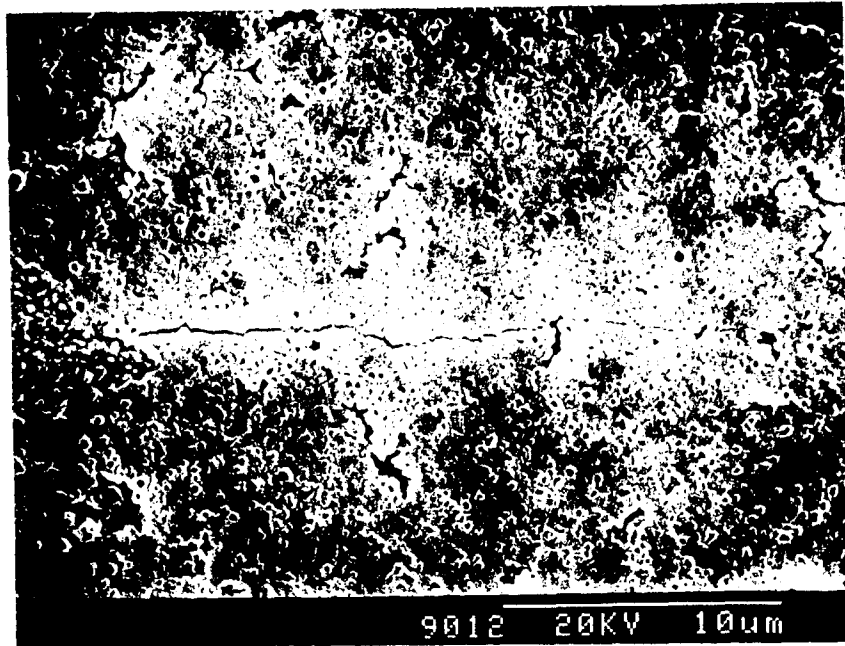


Fig.8. The pore microstructure in material G containing a population of elongated pores, shown being samples by a Vickers hardness indenter induced crack.

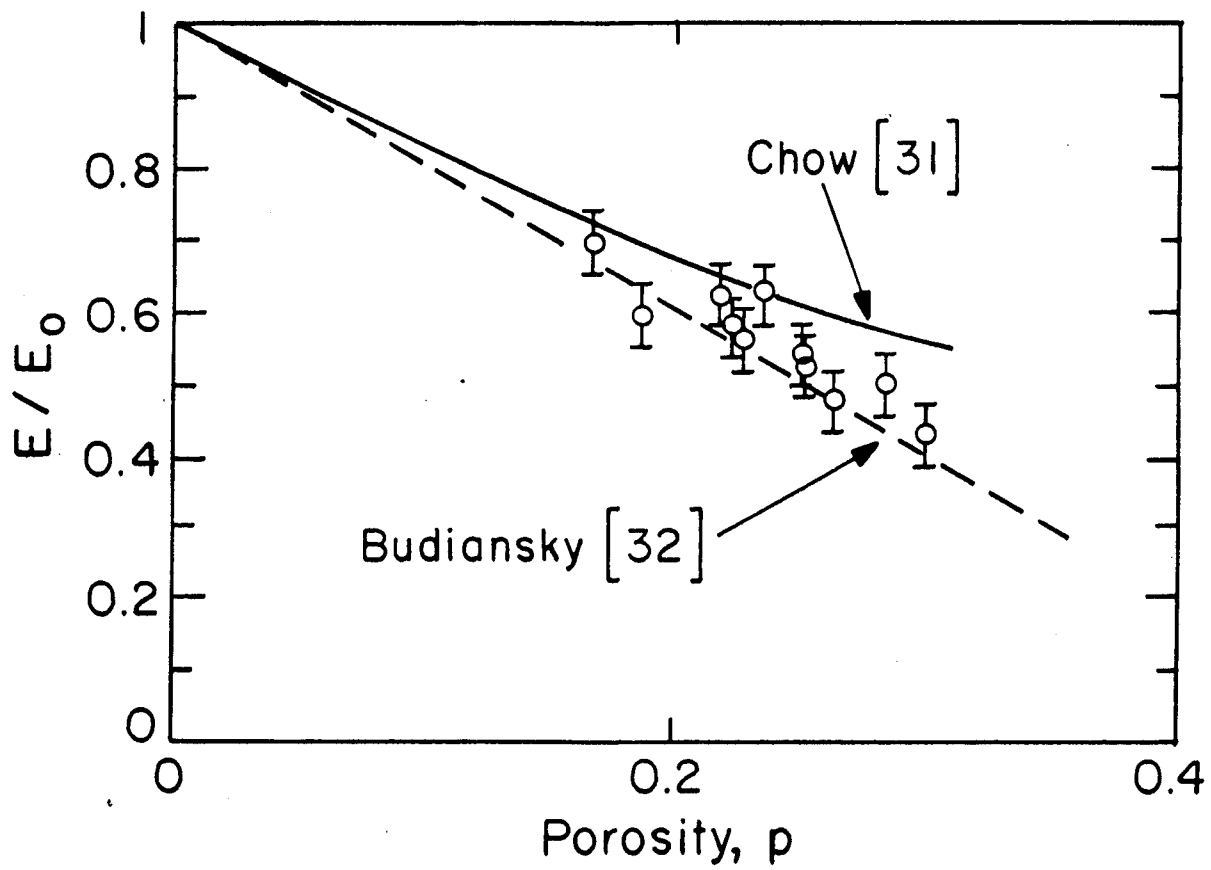


Fig.9. Effect of porosity on modulus is compared with two theoretical models: the Eshelby inclusion model of Chow [31] and the self consistent model of Budiansky [32].

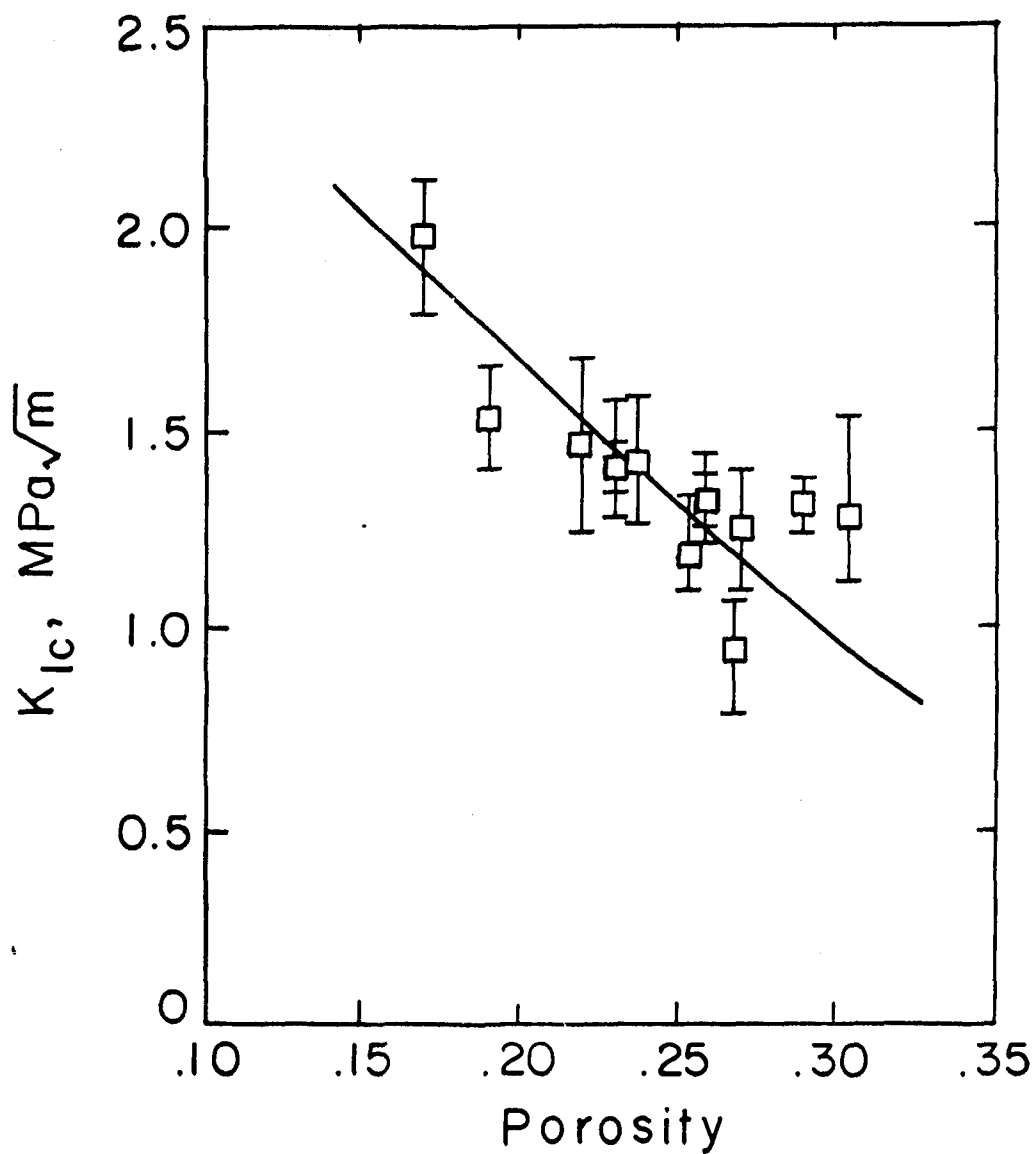


Fig.10. Dependence of fracture toughness of RBSN on porosity. The range of values for each material represents the local toughness variations and do not represent error bars of macro tests.

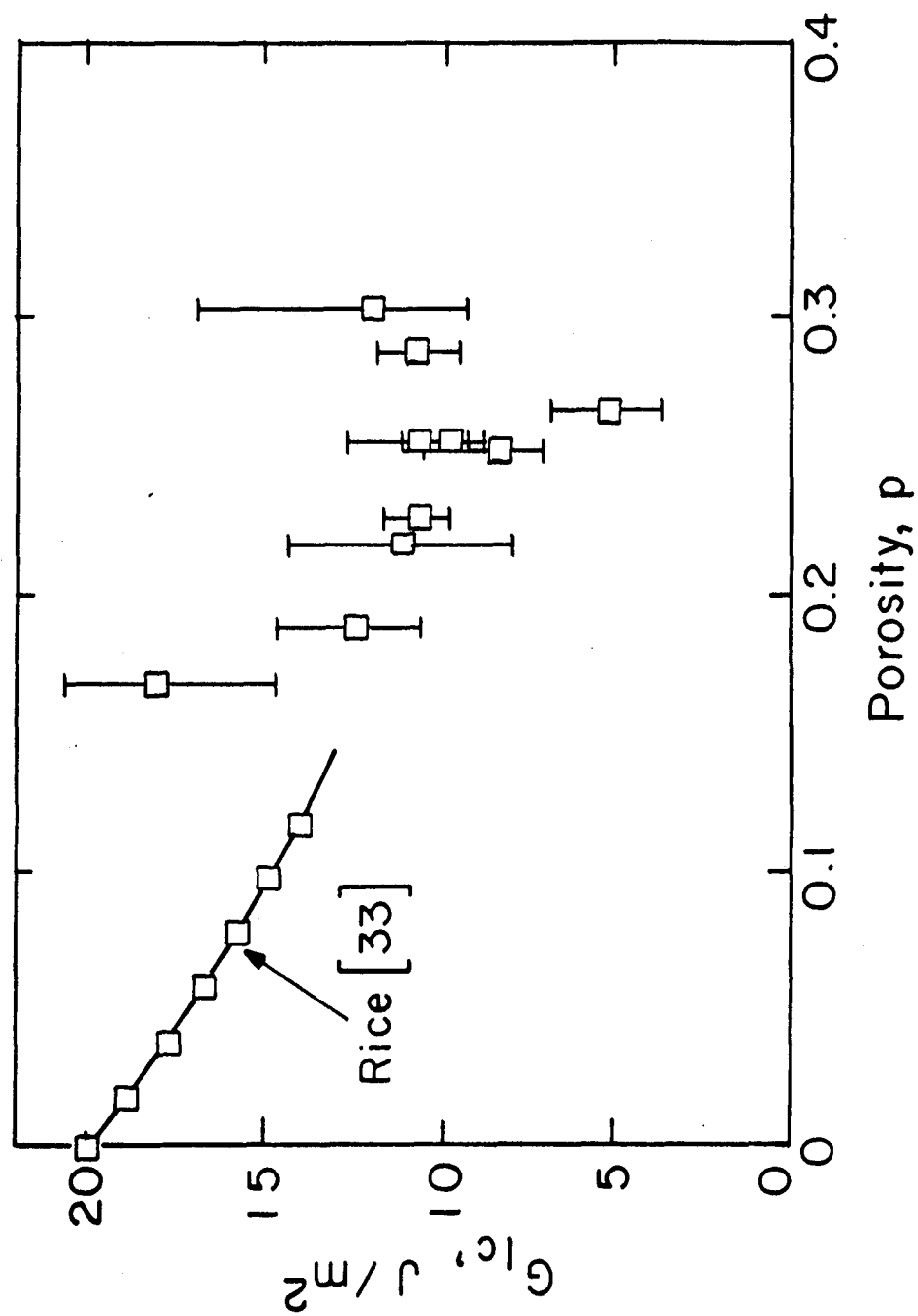


Fig.11.1. The fracture toughness results, as critical energy release rates, are compared with the published results of Rice [33] for material with lower porosity levels.



Fig.12.Fracture path through the highest porosity material (A), showing tortuosity and crack bridging arising from high local variability in fracture toughness.

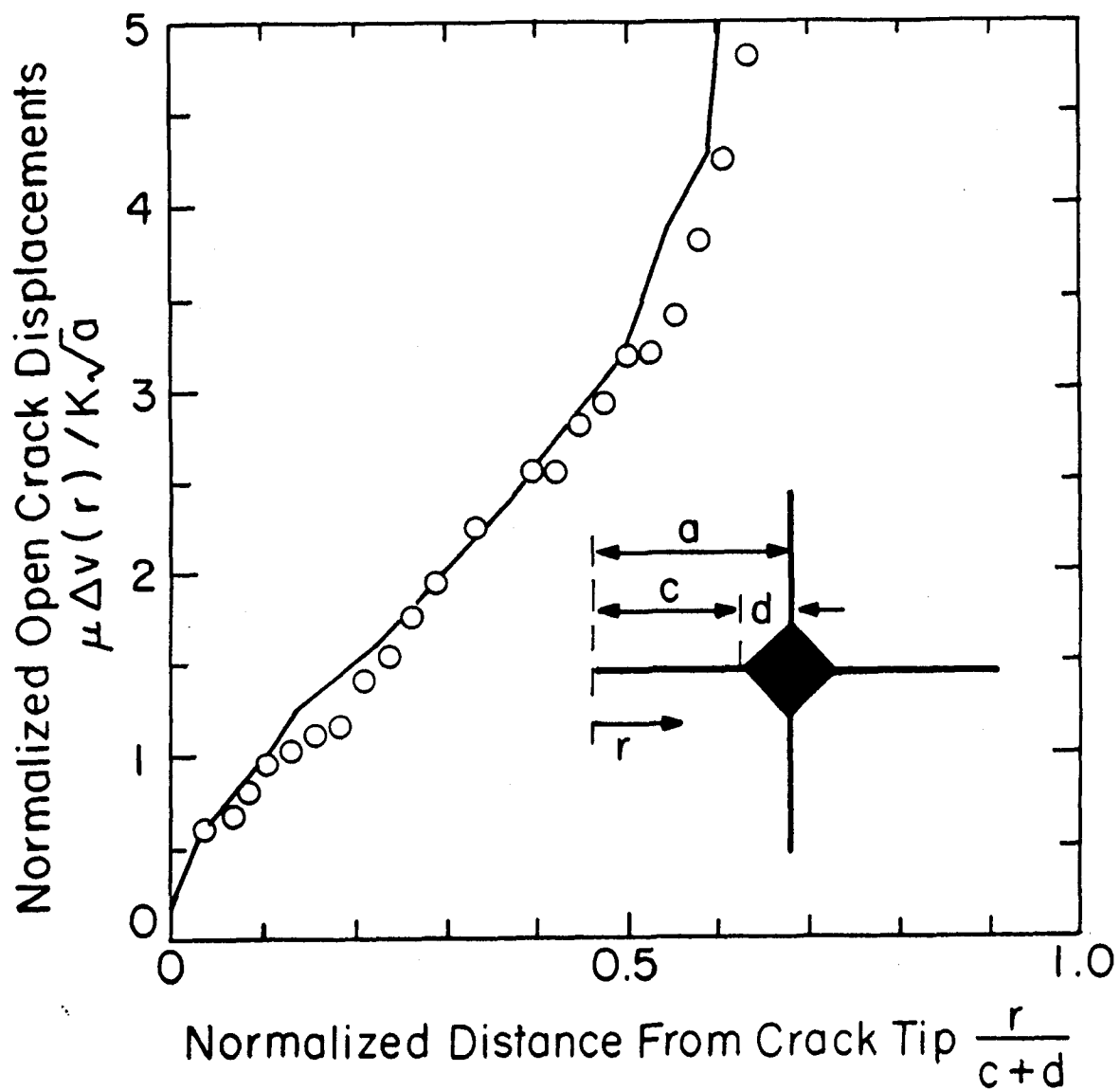


Fig.13. A specific test case fit for the determination of fracture toughness from open crack shape measurements in soda lime glass where a fracture toughness of  $K_{IC} = 0.55$  Mpa  $\sqrt{m}$  was determined from the fit of experimental results to the crack shape obtained by finite element computation.

APPENDIX C. "A New Method of Fracture Toughness Determination in  
Brittle Ceramics by Open Crack Shape Analysis"

F.G. Haubensak, and A.S. Argon,  
submitted to J. Materials Science.



# **A NEW METHOD OF FRACTURE TOUGHNESS DETERMINATION IN BRITTLE CERAMICS BY OPEN CRACK SHAPE ANALYSIS**

**F. Haubensak\* and A.S. Argon†**

**Massachusetts Institute of Technology, Cambridge, MA 02139**

## **ABSTRACT**

Improvement of the fracture toughness of high quality ceramics remains as one of the most important goals in materials development. An associated problem is the accurate measurement of fracture toughness in such brittle or semi-brittle ceramics, particularly in small samples encountered in material development. Previously used methods relying on measurement of the size of fracture mirrors, the indentation load and crack length in Vickers hardness induced cracking, and a variant of similar techniques have all been less than satisfactory in discriminating quantitative differences among materials. A hitherto unused technique of inferring the fracture toughness in samples from measurements of open crack flank displacements, which we have developed, avoids most of the theoretical and experimental difficulties of other methods. While it is somewhat intensive in terms of evaluation and requires high resolution of open cracks, the technique is fundamentally the soundest of all techniques and is capable of furnishing discriminating results. We present results of its application to the measurement of some model materials such as soda lime glass, single crystal silicon, alumina, and a reaction bonded silicon nitride whose porosity would ordinarily present difficulties with other methods.

---

\* Current address: Department of Materials Science and Engineering, Stanford University, Stanford, CA 94305-2205

† Author for correspondence.

## 1.0 INTRODUCTION

In the development of materials with superior fracture toughness the necessity of high resolution in the toughness measurements on small, laboratory scale specimens is paramount. In this pursuit, a number of methods have been applied in the development of high quality reaction bonded porous silicon nitride (RBSN) produced by Haggerty et. al. [1]. Nominally defect-free disk specimens initially were fractured in a ball-on-ring test configuration, and the fracture mirrors were measured and related to fracture toughness through the bend strength. These results showed broad trends, albeit with large uncertainty [2]. Standard indentation-toughness techniques, well described in the literature [3,4], were also used, but proved to lack sensitivity. An experimental technique to pry open cracks emanating from circular holes in plate specimens produced excellent results in model materials, but was limited in use with the high stiffness silicon nitride material of interest. Large corrections in the induced displacements, due to compression of the wedging mechanism, while calculable, became larger than the actual displacements, with the result that inaccuracies became too large to be acceptable.

Finally, it is known that the crack tip stress field can be deduced from the boundary conditions and the crack flank opening displacements, if the elastic properties are known. Therefore, this methodology was developed further and for the special boundary value case of the internally pressurized half penny shaped surface crack associated with the radial cracks of Vickers indentations. The development of this technique and its use in measuring  $K_{IC}$  in RBSN is the subject of the present communication.

## 2.0 METHODOLOGY

### 2.1 Theoretical preliminaries.

In a Mode I crack tip field for a crack under impending motion,  $K_I = K_{IC}$  can be determined from:

$$K_{IC} = \frac{(COD) \cdot E}{F(r/a)\sqrt{a}} \quad (1)$$

where  $F(r/a)$  is a non-dimensional characteristic crack shape factor dependent on the geometry and the mode of loading,  $a$  is the crack length, and  $E$  is the Young's modulus. The function can be determined by FEM methods for a crack of a given geometry and mode of loading under a unit  $K_1$ ,  $\sqrt{a}$  and  $E$ . An example is presented in Fig. 1a for the case of a Vickers indentation of interest in an elastic, isotropic material. It was found that the shape of the open cracks qualitatively fit best with the solution for an internally loaded crack with point loads at the positions corresponding to the corners of the indentation. This can be seen in Fig. 1b, where various open crack COD solutions are compared with measurements from indentations produced in a glass.

A fundamental assumption here is that indentation of material misfit or comminution chips under the indenter keep the crack open at the shape for its impending propagation. There are reasons to believe this to be the case in many circumstances [5-7], and various experimental observations [8], and analytical [9] modeling support the notion that the residual stress state upon the removal of the indentation load is sufficient to extend the radial cracks during the unloading process to conditions of crack arrest.

Nevertheless, because of such possible relaxations from a critically stressed crack state the determined fracture toughness values must be regarded as low toughness estimates.

## 2.2 Method of Observation

Determination of the crack length and opening shape was done primarily by standard scanning electron microscopy (SEM) techniques, in order to attain high enough resolution, typically up to  $2 \times 10^4$  magnification. However, other methods such as atomic force microscopy and sometimes even light optical microscopy, have the potential to generate a similar quality of data.

Elastic properties were obtained either from the literature for the model materials, or were measured with a pulse-echo technique described elsewhere [10].

## 2.3 Measurement of Open Crack Shapes from Micrographs

While other methods exist for determining crack flank opening displacements, a standard SEM was utilized for the measurements obtained here. The relative opening displacements were taken manually from the micrographs. Since the edges of the crack faces are not perfectly defined, upper and lower limits were estimated in the following manner. An upper limit was determined based on the notion that beyond a certain dimension, the contrast of the image does not change and represents the contrast of the surrounding solid. In the same way the estimate of the lower limit was determined by considering the contrast inside the crack.

The resolution of the measurements is fundamentally limited by the resolution of the micrographs. However, the capability of measuring multiple crack opening displacements permits this to be improved. Obtaining a well documented shape of a single crack reduces the errors in comparison with a single measurement. Typical uncertainties associated with the measurement of the fracture toughness obtained from one crack, as defined by the standard error parameter was found to be 3%.

#### 2.4 Results of Calibration Experiments in Standard Materials.

In order to determine the overall accuracy of the method, the measurement procedure was applied to three model materials: silica glass, an alumina single crystal and a silicon single crystal. The crack opening displacement data are shown in Figs. 2,3, and 4. The corresponding fracture toughness values are plotted in Fig. 5 for the data from the glass with the above described procedure, and shows an independence of the toughness with position along the crack. This implies a good match between the calculated and measured shape of the open crack dimensions.

Furthermore, the numerical values of fracture toughness correspond well with the accepted values for the three model materials, as shown in Table 1.

### **3.0 RESULTS**

Figures 6 and 7 show micrographs of the porous RBSN with indentation induced cracks, demonstrating the open crack configurations. Figure 7 shows an example of the frequently observed bridging phenomenon of a ligament across the crack faces.

These indentations in the RBSN were produced by Vickers hardness indenters with 400g loads, in materials which ranged in porosity from 10 to 30%. In each case, cracks were consistently produced with well formed shapes, i.e., four straight radial cracks emanating at right angles from neighboring cracks.

The calculated fracture toughness values as a function of porosity are shown in Fig. 8. As has been found in other porous material systems, fracture toughness values depend on the average porosity in an exponential fashion [11]. If the fracture toughness is a function of the porosity:

$$K = K_o \exp(-bp) \quad (2)$$

where  $p$  is the average porosity, then  $b$  is found to be 2.3, and compares well with data found in the literature where  $b=2.4$  a range of silicon nitrides. Energy release rates show this trend more clearly in Fig. 9. However, at the high porosity extreme, the toughness values tended to deviate considerably from the overall trend. This deviation correlates with the observation of a discernible increase in crack tortuosity in the highest porosity materials, as seen in Fig. 7.

The two exceptions to the overall trend are due to distinctly different processing steps. In material (a) a binder was added that increased the final density, and was postulated to create a final microstructure with more integrity. Material (b) exhibited large scale channel shaped pores which provided preferential fracture paths. Nominally, this material was produced with a slightly higher concentration of fine agglomerates which reduced the overall material homogeneity.

#### 4.0 DISCUSSION AND CONCLUSIONS

In the present experimental study we have utilized a theoretically well known tool for determining the critical stress intensity for crack growth from the measurement of open crack shapes. The method has been shown to possess good accuracy with some chosen model materials with well defined toughness values and has higher resolution than some previous methods involving measurement of indentation crack lengths associated with indentation load measurements. In the latter determinations of fracture toughness based on indentation loads, large uncertainties often exist resulting from frictional resistances which have no role in the propagation of the indentation induced cracks. In comparison, the crack shape measurement employed by us avoids such pit falls by relying entirely on the direct

measurement of relative displacement gradients along the crack which are linked to the critical crack tip stress intensity. The clear advantage of the method which has uncertainties less than 3%, are to some degree offset by the increased effort required in preparing high resolution micrographs.

The method of measuring  $K_{IC}$  through measurement of crack shape was utilized here to determine influences of specific processing steps on the fracture toughness of a series of porous silicon nitrides based primarily on their relative porosities. While other methods of measuring the fracture toughness on small size RBSN specimens indicated negligible differences, small, but definite, fracture toughness differences could be reliably resolved with the new technique. The measurements established a definite trend of decreasing toughness with increasing average porosity which has been commonly found in other studies as well [11]. However, at the highest levels of porosity where high crack tortuosity was found, fracture toughness values deviated significantly upward from this decreasing trend. This effect appeared to be due to increased occurrence of crack deflection and of crack face bridging ligaments in the high porosity materials.

### **Acknowledgment**

This research was supported by the AFOSR under Grant AFOSR-91-0263C. For this support we are grateful to Drs. G. Haritos and W. Jones of that agency.

### **References**

1. J.S. Haggerty, A. Lightfoot, J.E. Ritter, P.A. Gennari, and S.V. Garvey, *J. Am. Ceram. Soc.*, **72**: 1675 (1989).

2. S.V. Nair, P. Cai, J.E. Ritter, A. Lightfoot, J.S. Haggerty, "Indentation Residual Stresses in RBSN and RBSN Composites", 16th Annual Conf. on Composites and Advanced Ceramics, American Ceramic Society, Cocoa Beach, FL., Jan, 1992.
3. Z. Li, A. Ghosh, A.S. Kobayashi, and R.C. Bradt, *J. Am. Ceram. Soc.*, **72**: 904, (1989).
4. I.J. McColm., "Ceramic Hardness", Chapter 5, *Plenum Press*, New York, 1990.
5. A.G. Evans and E.A. Charles, *J. Am. Ceram. Soc.*, **59**: 371, (1976).
6. G.R. Anstis, P. Chantikul, B.R. Lawn and D.B. Marshall, *J. Am. Ceram. Soc.*, **64**: 539 (1981).
7. B.R. Lawn, A.G. Evans, and D.B. Marshall, *J. Am. Ceram. Soc.*, **63**: 574, (1980).
8. R.F. Cook and G.M. Pharr, *J. Am. Ceram. Soc.*, **73**: 787 (1990).
9. S.S. Chiang, D.B. Marshall, and A.G. Evans, *J. Am. Ceram. Soc.*, **53**: 298, (1982); *Ibid.*, 312, (1982).
11. F.G. Haubensak, A. Lightfoot, and J.S. Haggerty, *J. Mater. Sci.*, submitted for publication.
12. R.W. Rice in "Treatise on Materials Science and Technology", Vol II, edited by R.K. MacCrone, page 199, *Academic Press*, N.Y., 1977.



**Table 1. Values of  $K_{IC}$  for Model Materials**

Material	Measured Fracture Toughness	Previously Reported Fracture Toughness
Soda Lime Glass	$0.81 \pm 0.025$	0.40 - 0.85
Si - single crystal [110]	$0.84 \pm 0.03$	0.87
$\alpha$ -Alumina single crystal [110]	$2.86 \pm 0.10$	2.93*

\* value for hcp alumina

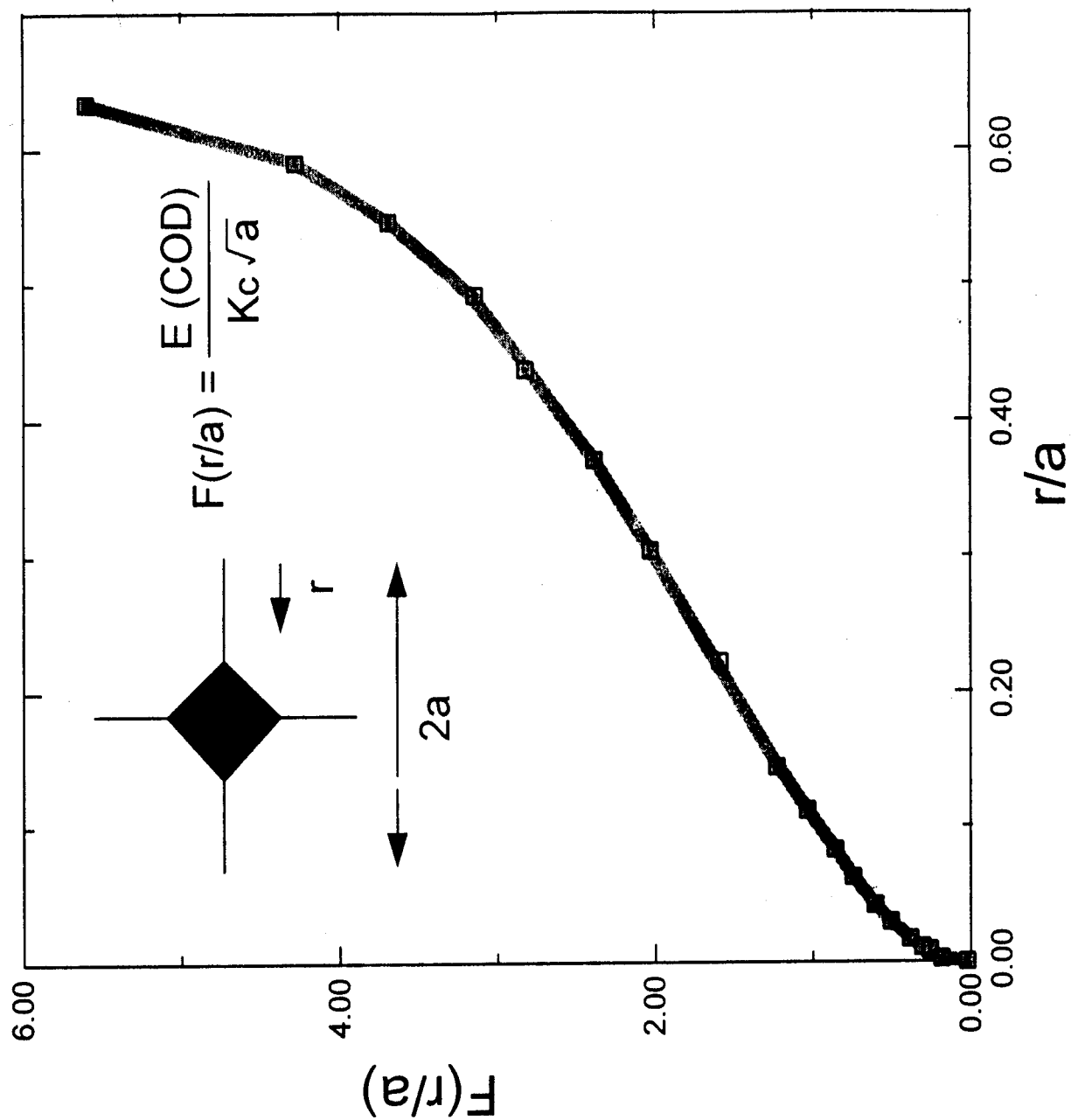


Figure 1a. The non-dimensional open crack displacement function for an isotropic elastic 2-D material. In this calculation, the application of the point load dipole occurs at  $r/a = 0.65$ .

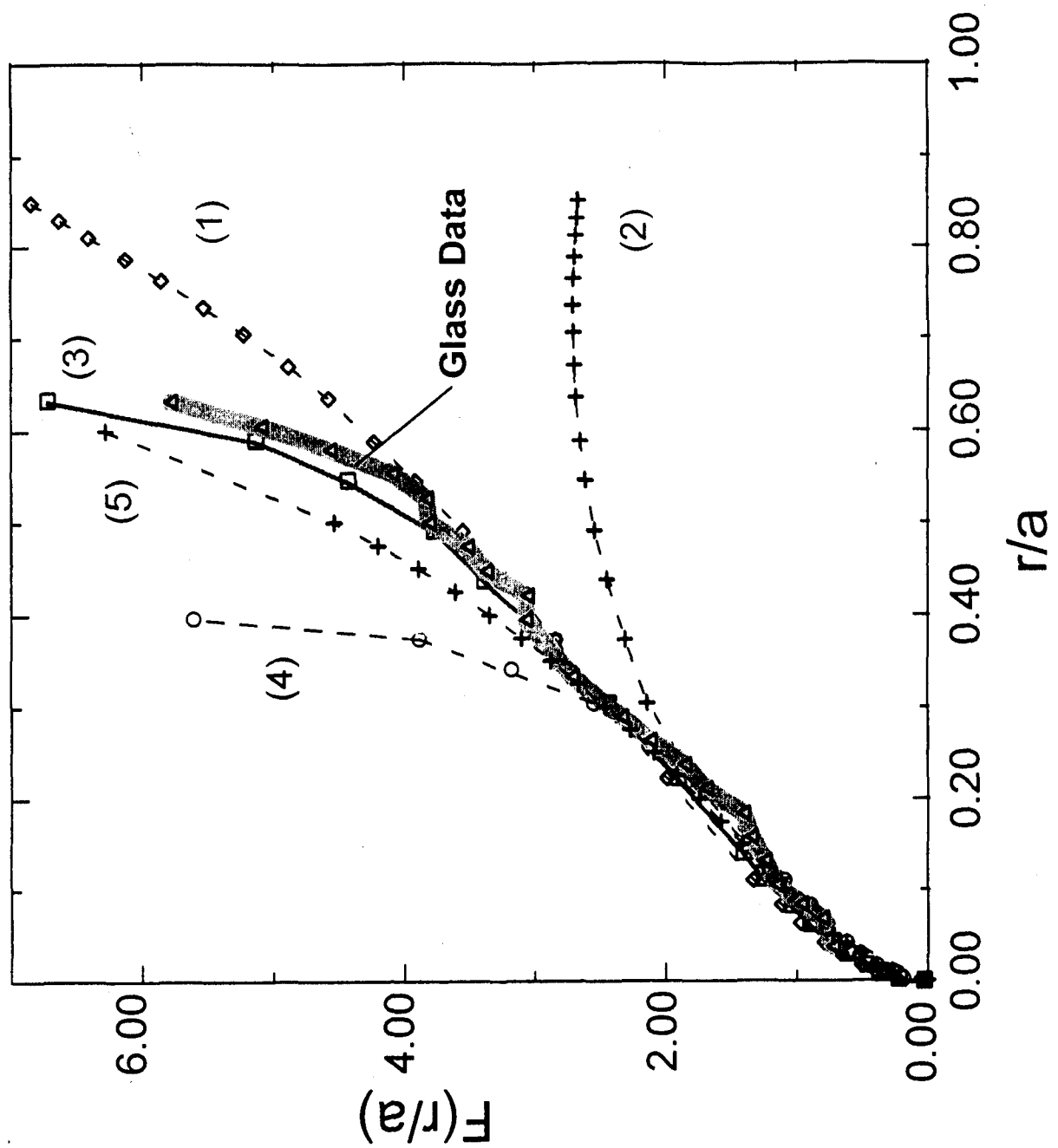


Figure 1b. Comparison of various open crack shape solutions for internally loaded surface cracks. Solution (1) is a center loaded point force, (2) is for uniform internal pressure over the portion of the crack representing the indentation impression ( $0.65a < r < a$ ), (3) is for symmetric point loading about the impression at  $r/a = 0.65$ , similarly (4) is for point loading at  $r/a = 0.40$ , and (5) is for a centrally loaded 3-D penny crack.

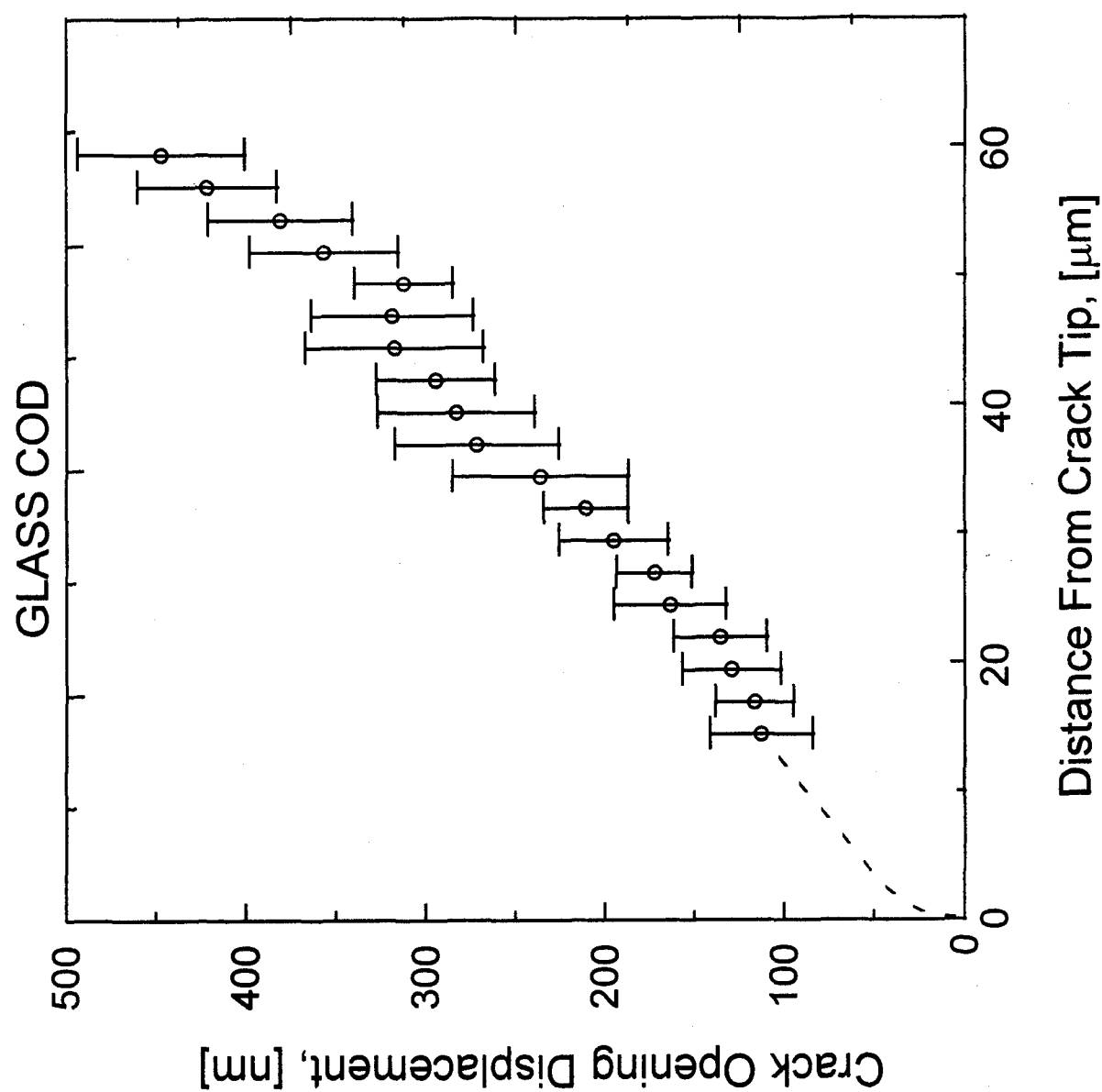


Figure 2. Open crack displacement data from indentation induced cracks in silica glass.

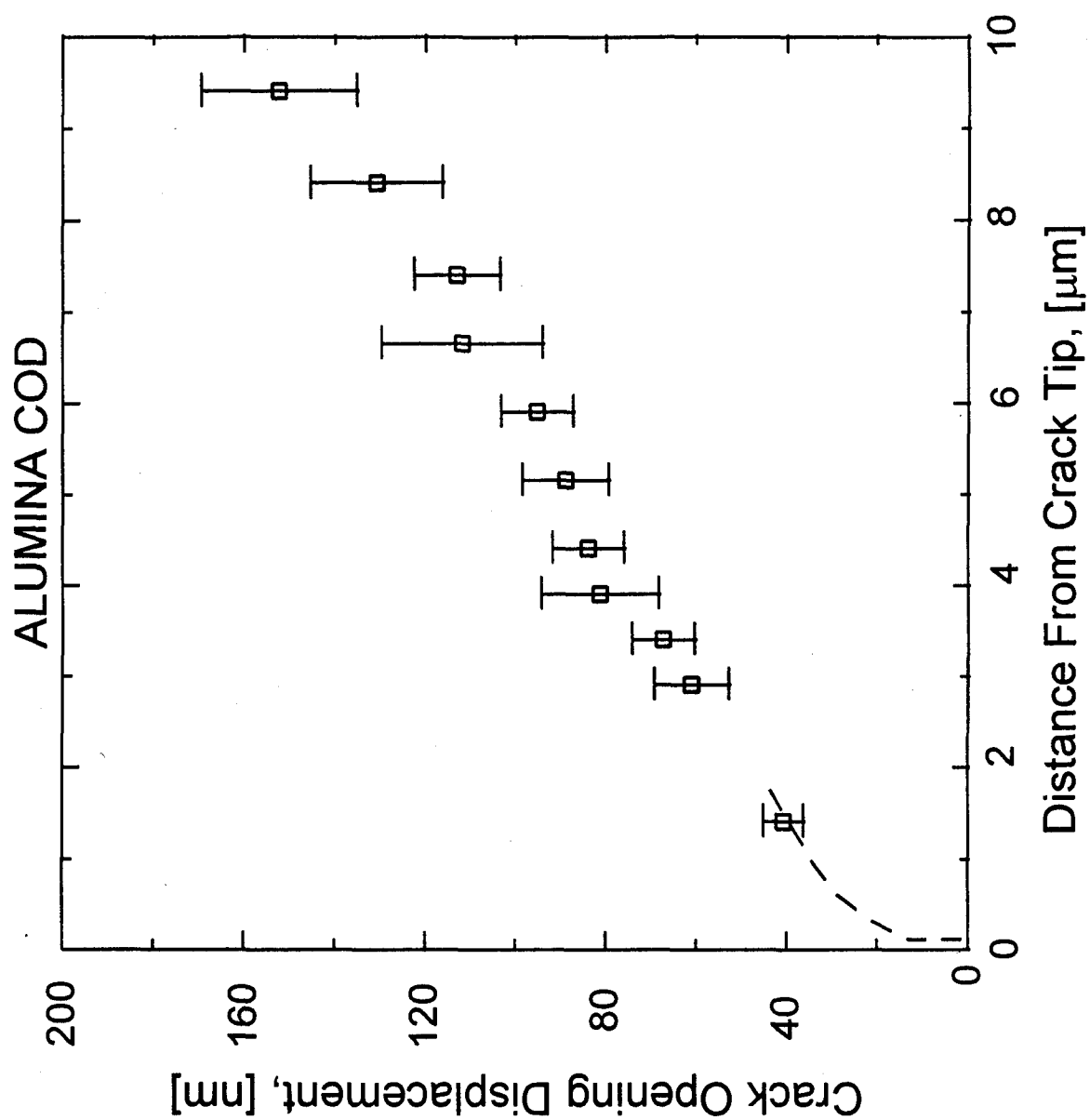


Figure 3. Open crack displacement data from indentation induced cracks in single crystal alpha alumina.

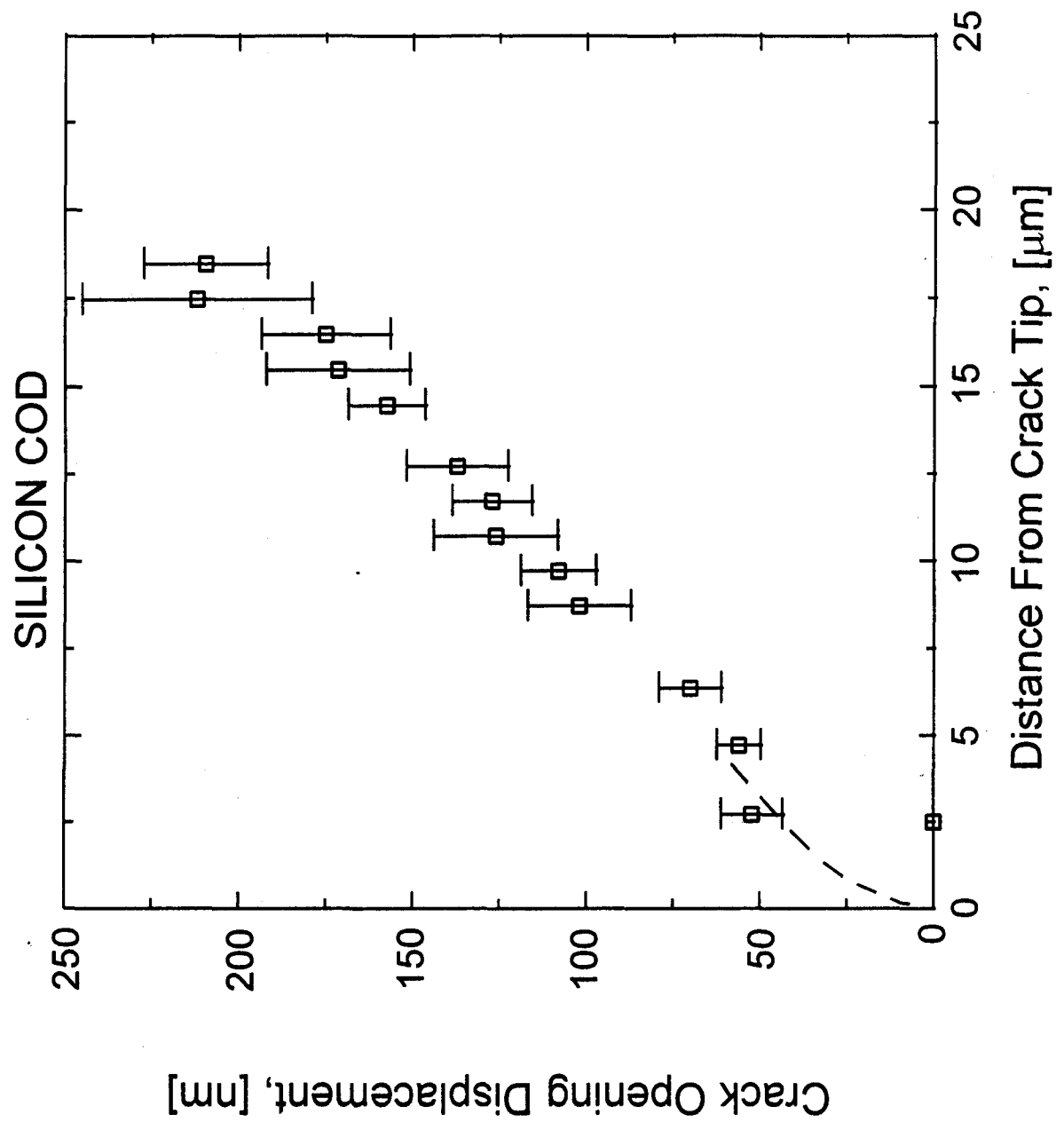


Figure 4. Open crack displacement data from indentation induced cracks in single crystal silicon.

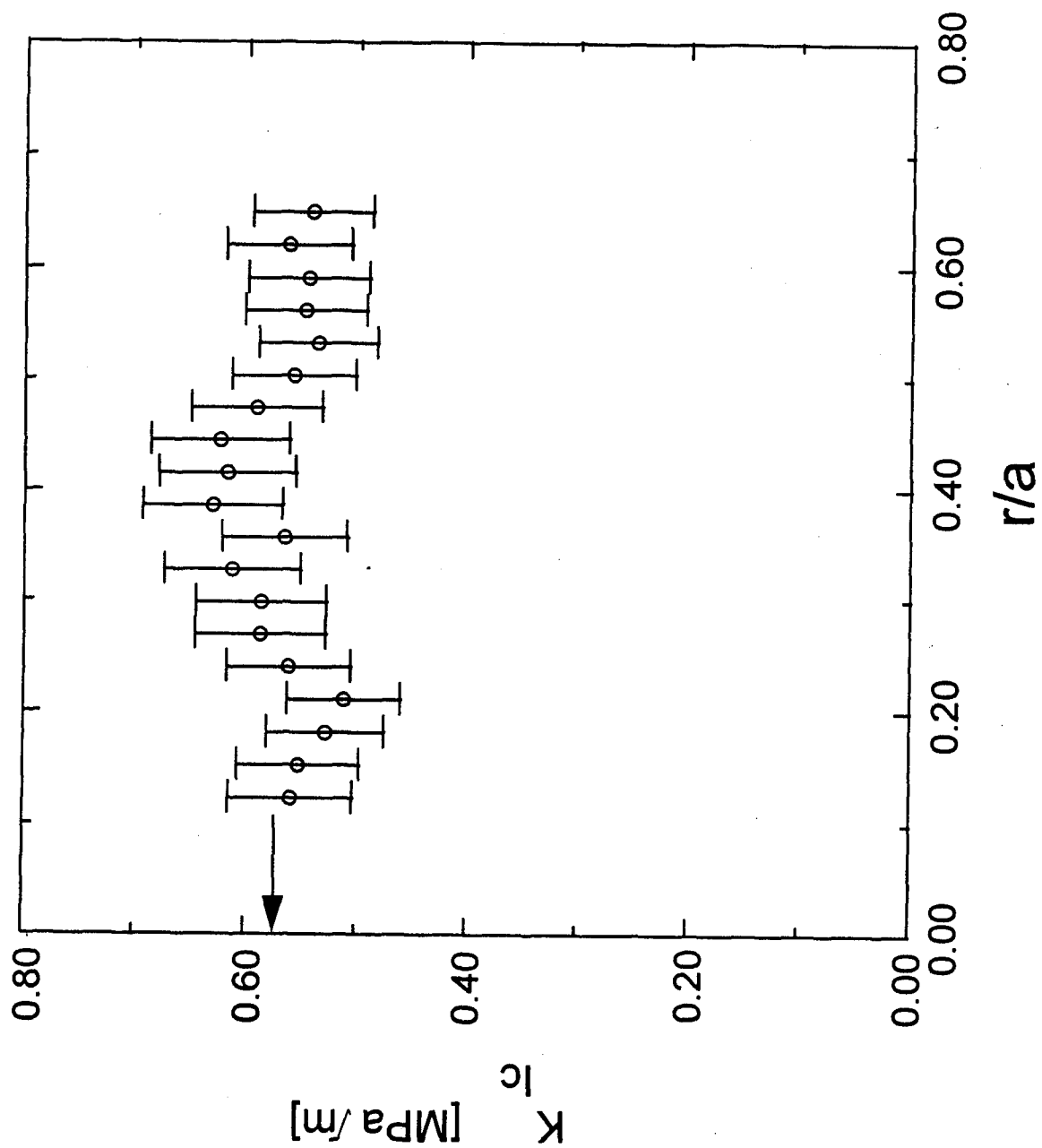


Figure 5. Fracture toughness values obtained from open crack shape measurements in glass. The independence of the toughness values from position along the crack indicates a good match of the calculated crack shape with measurements.



Figure 6. Micrograph of indentation induced radial crack in RBSN.





Figure 7. Micrograph of indentation induced radial crack in high porosity RBSN sample exhibiting high crack deflection and evidence for bridging ligaments.

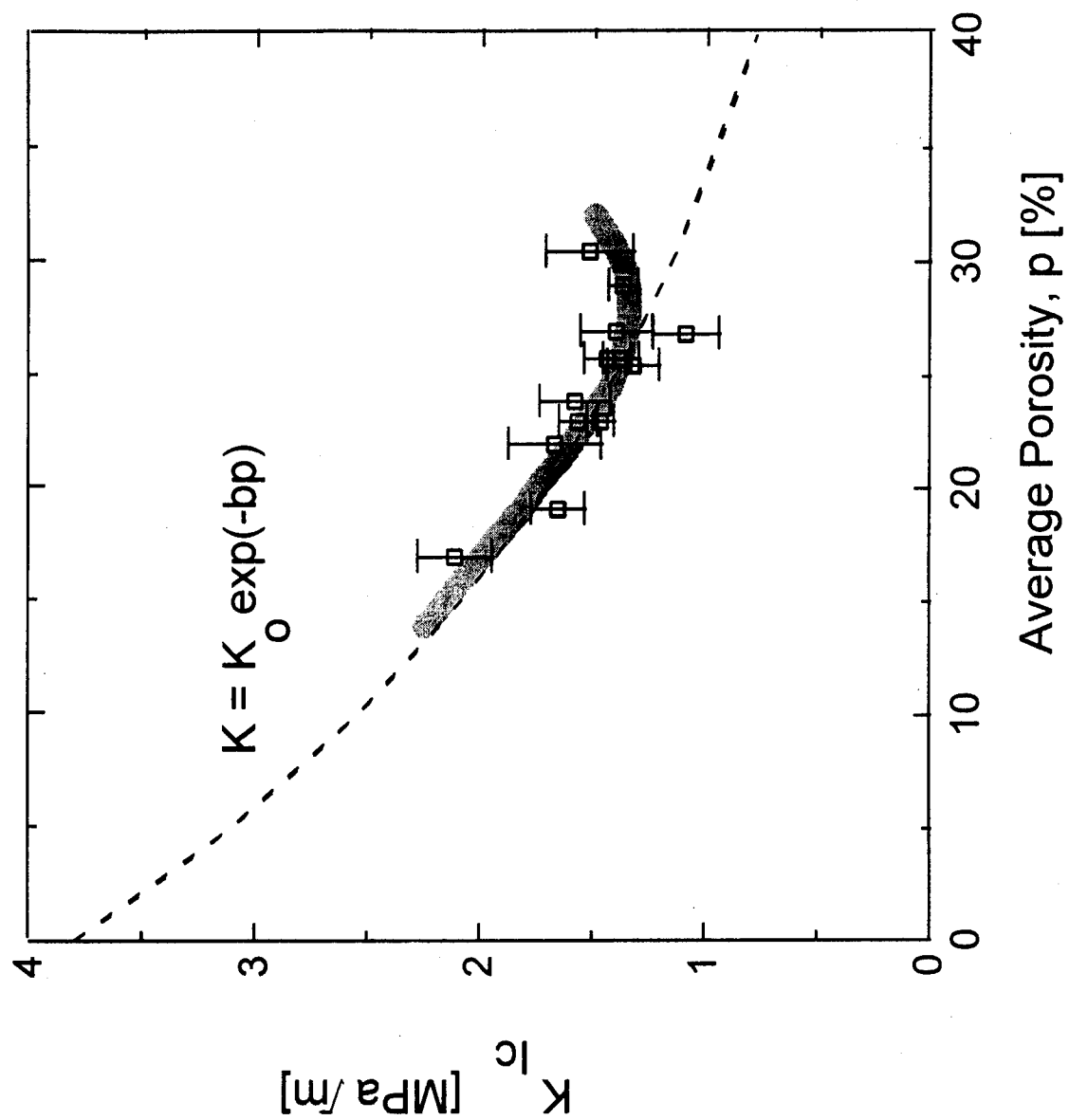


Figure 8. Dependence of fracture toughness on porosity in RBSN.

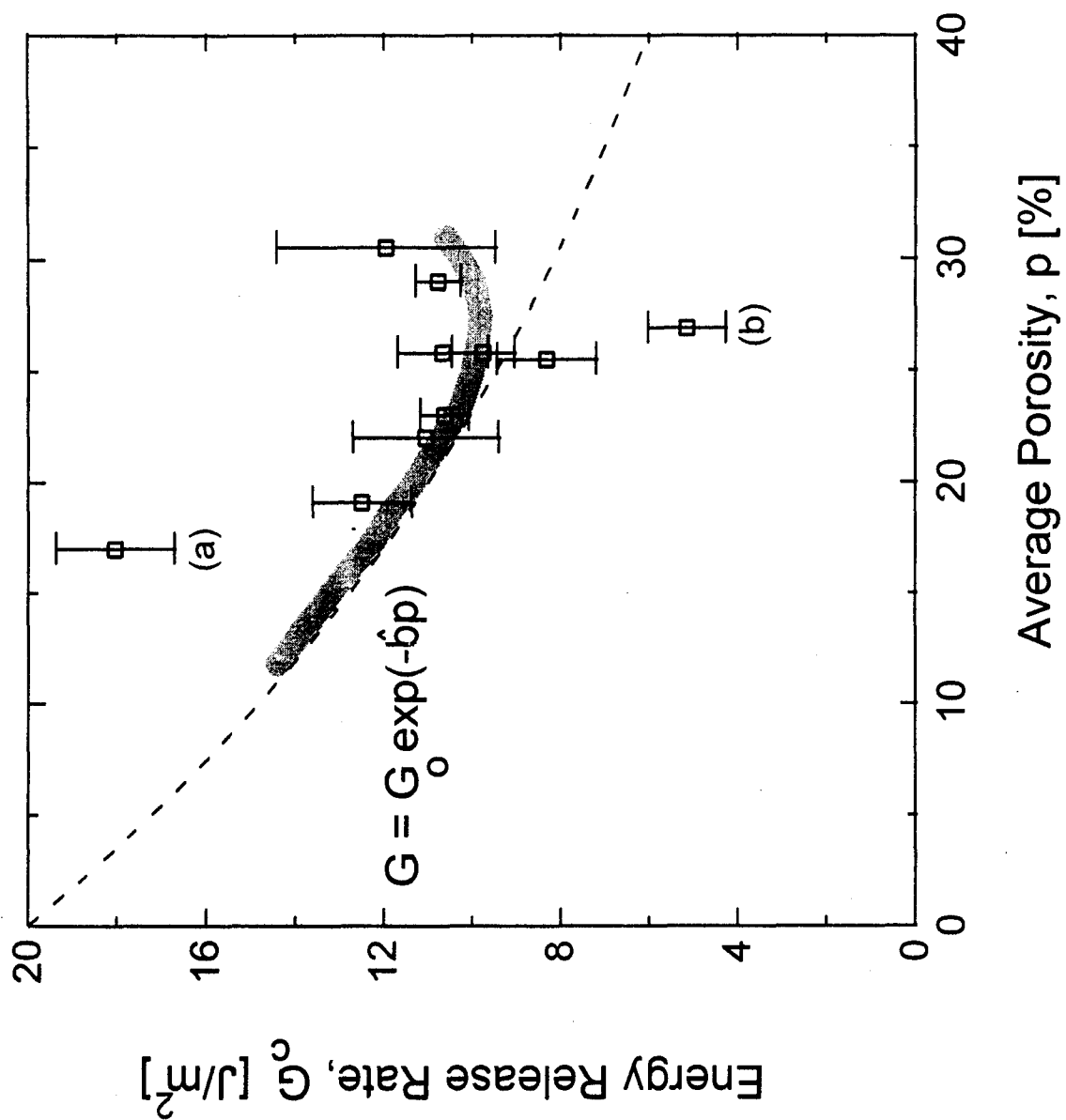


Figure 9. Dependence of energy release rate on porosity in RBSN.

APPENDIX D. "A Simulation of the Reaction Bonding of  $\text{Si}_3\text{N}_4$   
to Generate Porous Microstructures"

F.G. Haubensak, V.V. Bulatov, and A.S. Argon,  
submitted to J. Computer Aided Materials Design.

# A SIMULATION OF THE REACTION BONDING OF $Si_3N_4$ TO GENERATE POROUS MICROSTRUCTURES

F. G. Haubensak,\* V.V. Bulatov, and A.S. Argon\*\*  
Massachusetts Institute of Technology, Cambridge, MA, 02139

## ABSTRACT

A stochastic numerical technique is presented that has been used to study the formation of reaction bonded porous silicon nitride (RBSN). Like many reaction bonded materials, RBSN is a structural ceramic which has a naturally occurring porosity of approximately 25% resulting from the unique kinetics of formation. Since such porosity is usually unavoidable, it is of interest to discover its relevant measures, such as the size distribution and degree of homogeneity of pores, and the factors that govern the formation of these, in order to understand and optimize the crack propagation resistance of such materials. The probing of the fracture toughness of the generated microstructures by computational means is described in the companion communication.

The primary purpose of the simulated reaction was the generation of realistic microstructures incorporating the major features of reaction bonding. In this manner it is possible to generate objective, systematic variations of similar microstructures. With such microstructures, crack nucleation and propagation mechanisms can be observed and processing parameters which control fracture toughness can be identified.

In the present study, we outline the details of the reaction kinetics model, demonstrate its ability to generate realistic microstructures, and report some additional observations on some topological phenomena resulting from the reaction, such as those which control the formation of large pores in the final structure. In yet a separate communication of a related experimental study we present the microstructures of the actual RBSN. We will use the findings of the latter here for making some comparisons.

---

\* present address, Department of Materials Science, Stanford University, Stanford CA

\*\* author for correspondence

## 1.0 INTRODUCTION

The cause-effect relationship between microstructure and mechanical properties of materials, particularly their fracture toughness has been of interest for some decades. In most instances, a material with a given microstructure is studied by probing it with a number of more or less conventional tests. The results are then related and justified through a mechanistic model based on micromechanical analysis. In a few instances the findings of the microstructure-property connection is used to create different microstructures which should have better properties. In a complementary approach, that is usually only taken on paper, more ideal microstructures are considered which through the existing models should lead to superior performance. The usual constraint on this latter approach is the inadequacy of the available degrees of freedom in processing to achieve the sought after ideal microstructures. In a hybrid approach which we have taken, the microstructure-property connection is studied experimentally while in a parallel computer simulation the processes that control the microstructure and the mechanisms that control the property are modeled. This is pursued until a close correspondence is reached with the actual experimentally probed system through a systematic variation of the parameters that control the simulated microstructures. Once a proven cause-effect relationship is reached in the simulations that parallels the experimental one, it becomes possible to use the computer simulations to explore other conceivable microstructure-property connections and determine the possible benefits of pursuing new developments in processing to achieve such microstructures.

In the present communication we develop a numerical model of the gas phase reaction that results in porous RBSN for the principal purpose of generating non-arbitrary microstructures that are topologically similar to those of the real RBSN, that have been reported by Haggerty and co-workers [1-3]. In a companion communication we have explored the fracture resistance of these computer generated microstructures by means of a separate simulation of tensile fracture and of crack propagation through these porous microstructures to develop the microstructure-property connection [4]. This pair of simulations has given a detailed and valuable understanding of the gaseous reaction that forms the porous RBSN, and the mechanical worth of the specific porous microstructures.

Figure 1 shows a typical microstructure of porous RBSN as produced in the Ceramics Processing Research Laboratory at MIT. The pores are equiaxed with relatively smooth

surfaces indicating that during the formation of the RBSN there is a finite amount of time for some smoothing of the surfaces by diffusion. The phase content and grain size, as determined by TEM and x-ray techniques were found to be predominantly of the  $\alpha$  phase at 75-80% which in some cases tended to form whisker-like shapes, while the remainder was  $\beta$   $Si_3N_4$  in typically larger and rod-like morphology. The TEM observations indicated, however, more equiaxed grains of a size roughly equal to the size of the small pores in the final reacted microstructure. Moreover, a small residual concentration of unreacted silicon was also detectable which, however, is difficult to capture on micrographs. The experimental observations of fracture paths established that fractures follow predominantly along grain boundaries [3].

In the present pursuit, the process of interest has been the reaction bonding of silicon nitride (RBSN). In a closely related experimental program, Haggerty and co-workers [1,2] have produced a high quality porous RBSN from sub-micron size spherical  $Si$  powder. The microstructure and mechanical properties of this RBSN, including its fracture toughness, have been studied in considerable detail [3,5]. An intriguing aspect of these experiments was the measured fracture toughness which ranged from 1.0 to 2.7  $MPa\sqrt{m}$  and appeared to be related to different and reproducible features of the microstructure [3]. Since the experimentally observed fracture paths showed some evidence of crack deflection, crack bridging and possibly even crack tip shielding, resulting from some surrounding redundant microcracking, the possibility of improving the fracture toughness further by deliberate microstructure manipulation became of interest. Such a pursuit becomes possible in the pair of computer simulations of microstructure and crack propagation, presented here and in the companion study [4].

## 2. METHODOLOGY

### 2.1 Reaction Chemistry

In order to generate realistic porous microstructures of RBSN, it is important to include all the major features of consequence of the reaction bonding process in the simulation. The reaction begins with the formation of discrete  $Si_3N_4$  nuclei which become established over an initial incubation period [1]. These nuclei grow at the expense of the evaporating silicon and form individual grains in the final microstructure. Under typical processing conditions the chemical pathway for the formation of silicon nitride is elemental silicon, undergoing sublimation and a subsequent gas phase reaction with nitrogen:



where the subscripts  $g$  and  $s$  indicate the gaseous and solid nature of the reactants and the product. This process is essentially similar to a chemical vapor deposition process with product formation on previously formed silicon nitride. The free surface of silicon nitride serves as a reaction catalyst. Although the complete reaction may include intermediate steps such as formation of silicon monoxide vapor which then acts as a silicon carrier, here these details are not of interest but rather a single all-encompassing composite reaction is developed. The formation of a reaction product on previously existing silicon nitride gives rise to a growing product front which is in competition for space with the silicon particles, in the process of receding by evaporation. The balance between these two processes is one of the phenomena which most strongly affects the reaction rate and morphology of the unique porous microstructure.

Silicon transport by solid state diffusion has been suggested by some investigators [6] however this is kinetically unfavorable. Solid state diffusion is too slow to account for the observed "fast" reaction rates [7,8]. In addition, it has been pointed out that the silicon vapor pressure of  $10^{-3}$  atmospheres at typical processing temperatures, is more than adequate to sustain the observed nitridation rates [9].

The assumption of fast nitrogen vapor transport has been verified experimentally [1]. For 1 atmosphere  $N_2$  and samples two millimeters thick, complete nitridation has been observed at the center of samples of average thickness in the millimeter range for temperatures from



1150 to 1350°C over typical reaction periods of 5 to 60 minutes [10]. Therefore, in the present simulation, a constant partial pressure of nitrogen is used, and the silicon vapor is the rate limiting medium, adjusting to new conditions instantaneously.

Popper and Ruddlesden [11] recognized that the exothermic nature of the reaction could cause melting of the unreacted silicon unless the heating rate was carefully controlled. However, such melting effects are considered inessential and have not been incorporated in the present model. Isothermal conditions are assumed for simplicity.

Lastly, acknowledging that the silicon nitride grains exhibit anisotropic growth, we have allowed for preferential growth directions. The degree of anisotropy is dependent upon which of two silicon nitride phases dominate;  $\alpha$  or  $\beta$ . While the precise control of phase content is currently a topic of debate, it has been observed that the  $\alpha$  phase is favored for vapor phase reaction processes at lower temperatures, and for relatively pure silicon powders. Its morphology has been observed to range from equiaxed to whisker-like. The  $\beta$  phase has an elongated morphology, though not whisker-like, and is typically larger in size. It is prominent in materials processed with either impurities such as iron or at higher temperatures where liquids are prevalent.

## 2.2 The Numerical Technique

Cellular automata methods have been developed for modeling microscopic physical processes to study fluid dynamics [12,13], solid state diffusion [14] and critical points in phase transitions [15]. Recently, this technique has also been used to address the issues in the complex coupled problems of reaction/diffusion associated with materials processing. Dab and Boon [16] have presented results for a more sophisticated microscopic process than the usual simple collisions in the previous models, by introducing the existence of chemical reactions in the medium. The model of an autocatalytic reaction incorporating diffusion, displayed essential features in qualitative agreement with systems involving non-discrete reaction-diffusion as described by analytical solutions of such processes. More recently, Srolovitz and co-workers have demonstrated good agreement between experiment and three dimensional Monte Carlo simulations of grain coarsening [17].

In the present study the modeling of the reaction has been performed in the spirit of the cellular automata (CA) approach, where the simulation volume is divided into cells, each of

which is allowed to exist in one of few discrete states. The state of a given cell changes in steps, as determined by its current state and that of its nearest neighbors. However, unlike the classical CA approach, where evolution of states is deterministic, here the cell in any given state has more than one possible transformation alternative.

To choose between the several possible outcomes in the reaction, a random number generator was employed. Thus, the approach used here has features common to both CA and Monte Carlo algorithms. However, deterministic CA evolutions may be thought of as limiting cases of the present stochastic simulation, when probabilities of all but one outcome are set to zero. This is why we associate the present simulations with the CA approach.

The reaction model that has been used is a 2-D cut out of a 3-D dense random packing of spheres in space, as will be expanded on below in Section 2.3. The choice of resolution of the mesh was based on maintaining equiaxed particle shapes, therefore, the cell dimension was a small fraction of the initial silicon particle size. The total mesh dimension was limited only by computational resources. At maximum resolution, we have obtained fully reacted structures spanning 1000 by 1000 cells or approximately 130 particle diameters or equivalently a volume of  $2 \times 10^6$  particles. In order to expedite generation of larger number of structures, a mesh of an edge length of 64 cells was chosen for most simulations. This insures the packing of enough silicon particles into the mesh (about 100) and provides an acceptable representative volume element (RVE) for a relevant microstructure.

## **2.3 Motivation and Limitations of the Model**

As already stated, the motivation for developing the present numerical model was to generate microstructures for subsequent fracture studies, rather than to develop a fully detailed study of the reaction kinetics. The limitations of the model, primarily its two dimensional nature and its fixed resolution, restrict our conclusions to indications of trends. Nevertheless, it has been possible to obtain meaningful trends of fracture toughness that could be identified with specific processing parameters. In addition, it appears possible to obtain some insight into such complex phenomena as the spatial competition between the growing silicon nitride particles and the silicon particles receding by evaporation of silicon, and the effects these processes have on the fracture toughness of the material.

In the present model any internal stresses arising from such effects as densification through

sintering or volume changes arising from the reaction, other than from the stoichiometry of the chemical process, are not specifically considered. Incorporation of this effect would have required a substantial expansion of the model to include simultaneous considerations of mechanical equilibrium and elastic strain energies. We compensate for this omission by assuming certain parameters governing the strength of interfaces in our fracture simulation [4].

### 3. THE MODEL

#### 3.1 Overall Outline

The following features of the model will be described operationally: the packing of the unreacted green body; the placement of initial silicon nitride nuclei which become single grains in the final microstructure; and finally the chemical conversion into reaction bonded silicon nitride (RBSN).

#### 3.2 Packing of Unreacted Silicon Particles

To avoid artificial clustering phenomena and excessive porosity arising from the two dimensional nature of our model, the initial unreacted silicon particles were actually modeled as a three dimensional random close packed structure of uniform sized spheres. This approximation is well suited to the actual spherical *Si* particles used in the RBSN produced by Haggerty and co-workers [1,2] and for its qualitative similarity to the usual green body packings (i.e. the existence of expected naturally occurring packing defects and lack of long-range periodicity [18]) with its similar packing density,<sup>1</sup> (62%).

The particle coordinate data was generated by a molecular dynamics (MD) technique using periodic boundary conditions. Many methods can be utilized to generate dense random packing of spheres, but the MD technique [19] is efficient and provides packings which have the spatial distribution of the random close packed structure as demonstrated by the radial pair distribution function of particle centers in Fig. 2.

This 3-D structure of dense random packed spheres was subsequently sectioned by a geometrical plane to obtain a two dimensional arrangement of circles of a well known size distribution. This information was then discretized using on a hexagonal planar mesh.

Figure 3 shows a typical planar section through the 3-D initial dense random packing of spheres which was taken for the 2-D model. Figure 4 shows schematically how the 2-D plane arrangement of material in circular disc form and surrounding voids are discretized

---

<sup>1</sup>Dense random structures have the most efficient packing of uniform sized particles without long range periodicity.

into reacting cells for the reaction model.

### 3.3 Nucleation of Silicon Nitride

Once the geometry of the sectioned particle field is mapped on the 2-D mesh hexagonal, the cells of the mesh that represent surface sites of  $Si$  particles are located (i.e.  $Si$  cells with at least one neighboring empty site). A given number of these surface sites were then randomly chosen to be the initial  $Si_3N_4$  nuclei and were replaced by  $Si_3N_4$ . The number of such nuclei was small, typically 1-10 per particle, (i.e. 100-1000 nuclei compared to typically 10,000 total cells).

In some instances, a given proportion of these nuclei were assigned to have preferential growth directions to simulate anisotropy of grain growth. Growth directions were chosen randomly from among three discrete directions corresponding to the three-principal symmetry axes directions of the mesh.

### 3.4 Conversion Reaction to $Si_3N_4$

#### 3.4.1 Basic components

Given the green structure of  $Si$  particles, the probabilities were computed for each of the following possible events at each individual surface cell site: (a) the evaporation and condensation of silicon; (b) the reaction and growth of silicon nitride; (c) grain coarsening and surface diffusion.

#### 3.4.2 The condensation and evaporation of silicon vapor to and from free silicon surfaces

For every site that represents  $Si$ , each nearest neighbor was checked for an empty cell. If one existed, the  $Si$  site was labeled as a surface  $Si$  site, and was a possible candidate for evaporation. The incremental probability for evaporation,  $\delta P_{\text{evap}}$ , was taken to be proportional to the increment in time,  $\delta t$ , chosen for all processes, i.e.

$$\delta P_{\text{evap}} = E \cdot \delta t, \quad (2)$$

where  $E$  is a kinetical rate constant discussed further below. If evaporation was deemed to occur, the cell was transformed into an empty cell and the silicon vapor pressure was incremented.

Condensation was taken to be the reverse of evaporation for which an empty cell located next to a  $Si$  cell was a candidate for condensation, where the probability for the condensation transformation was taken to be proportional to the silicon vapor pressure.<sup>2</sup>

### 3.4.3 The conversion reaction and growth of $Si_3N_4$ from previously grown free $Si_3N_4$ surfaces

In a similar manner as for the evaporation and condensation processes presented above, empty cells neighboring on  $Si_3N_4$ , were allowed the possibility of undergoing a transformation to  $Si_3N_4$ , thereby extending the growth front. The incremental probability,  $\delta P_{\text{reaction}}$ , of growth of  $Si_3N_4$ , was taken to be proportional to the partial pressure  $p_{\text{siiv}}$  of silicon vapor (the rate limiting species), a rate constant  $R$ , and the time step,  $\delta t$ :

$$\delta P_{\text{reaction}} = R \cdot p_{\text{siiv}} \cdot \delta t. \quad (3)$$

Once growth occurred, the vapor phase was reduced in a stoichmetrically appropriate way.<sup>3</sup> It is important to note that this generic growth law does not specify the mechanism of growth. Only that previously grown  $Si_3N_4$  is allowed to continue to grow further, and that the growth rate is proportional to the concentration of the critical vapor species of silicon, as well as the reaction constant  $R$ . It is assumed that  $N_2$  is present in abundance as an infinite reservoir, requiring no separate  $N_2$  balance.

### 3.4.4 Grain boundaries and surface tension

Surface tension and "grain boundary tension" were incorporated into the model in order to give more realistic appearing structures. Although sintering processes are thought not to be very influential in the low temperature processing regime ( $T < 1350^\circ\text{C}$ ), micrographs (both TEM and SEM) give the impression of relatively smooth grain boundaries and pore

<sup>2</sup>The amounts of silicon evaporation and condensation are implicitly a function of the amount of silicon free surface because each individual surface particle is given a chance to evaporate or adsorb silicon vapor.

<sup>3</sup>The volumetric expansion of  $Si$  reactant in the reaction bonding process with  $N$  gas to final  $Si_3N_4$  is 1.22. Therefore in order to conserve  $Si$  mass, to produce 1 volumetric unit of  $Si_3N_4$  product, 0.82 fractional units of one solid cell of  $Si$  is effectively consumed, from the vapor phase.

surfaces. Therefore, surface tension and boundary tension parameters were introduced for the silicon nitride material. For grain boundary motion, the silicon nitride cells with neighboring cells of silicon nitride of another grain orientation were given a finite probability to transform to the orientation of the other grain. In the case of the free surface, a surface cell was allowed the possibility of translating to a neighboring empty surface site that is adjacent to the same grain of silicon nitride. The specific details are presented in Appendix I.

#### *3.4.5 Implementation of the reaction model*

In practice, the simulation began by sectioning of the 3-D particle packing and mapping the resulting cross-section onto the 2-D mesh followed by the placing of the  $Si_3N_4$  nuclei as outlined above. Once this was accomplished, the global variables, time  $t$ , and silicon vapor pressure,  $p_{siv}$  were initialized to  $t = 0$  and  $p_{siv} = 0$ . After this initialization, time was incremented by  $\delta t$ . The choice of  $\delta t$  was made by computing incremental probabilities for all processes and by making  $\delta t$  to be a small fraction of the inverse rate constant of the fastest process. In this manner, all processes were scaled consistently, so that the transformation of a particular cell was maintained to be exclusively a function of the current state of its surrounding neighbors. With this choice of  $\delta t$ , for each cell, all incremental transformation probabilities were computed and certain events were chosen to take place, all based upon the use of a random number generator. In the cases of evaporation, condensation and reaction of  $Si_3N_4$ , the mass balance of  $Si$  was accounted for by appropriately incrementing and decrementing the parameter  $p_{siv}$ . As already stated, the transport of  $N_2$  was assumed to be easy in comparison to  $Si$ , so that no mass balance was kept for it. Moreover, isothermal conditions were assumed requiring no adjustments of the rate constants in the course of the simulations.

## 4. RESULTS

### 4.1 Overview of Results

Many features of the reaction kinetics process are mirrored in these simulations. For example, the basic trends of the extent of the reaction with time and the pore to particle size ratio are in quantitative agreement with experiments as we will demonstrate below. Moreover, the effect of the initial *Si* particle positions on the final pore positions is also in qualitative agreement with experimental observations.

Making due allowances for some noted assumptions, we utilize the fact that the simulations presented here have some connection with the real process, and report observations of the effects of the reaction on microstructure. Throughout the discussion below, attention will be paid to microstructural features as they relate to the various reaction parameters, in particular grain and pore size and shape, as well as the effect of packing defects on the final microstructure.

### 4.2 Comparison with Experimental Observations

In Fig. 5, the comparison of the normalized number density distribution of pore sizes (in units of particle size) for the simulated and actual microstructures reveals comparable average dimensions and qualitative agreement between the size distributions. Other comparisons of pore aspect ratio and pore circumference distributions between the model and experiments is given in Fig. 6. The ratio of the average grain size,  $D$ , to the initial *Si* particle size,  $d$ , for initial density of nuclei,  $N = 14.4$ , per *Si* particle, in a 2-D cross section is 0.45 in the model, compared to the expected ratio of 0.439 as presented in Appendix II. The  $Si_4N_4$  grain and initial *Si* particle sizes were determined experimentally with a combination of electron microscopy and x-ray techniques [20].

Additional agreement between the model and actual reaction kinetics behavior can be found in the time dependence of the extent of the reaction. The simulated extent of the reaction follows the Johnson-Mehl-Avrami form of:

$$X = 1 - \exp(\alpha N t^n) \quad (4)$$



where  $X$  is the total fraction transformed,  $N$  is the constant density of nuclei,  $\alpha$  includes the growth rate constant and geometric factors,  $t$  is time, and  $n$  is the time exponent. Figure 7a shows the simulated dependence of  $X$  on  $t$ , which compares well with the form of the Johnson-Mehl-Avrami model, giving an exponent of  $n = 1.5$ . Figure 7b shows thermogravimetric data by Sheldon and Haggerty [1], given here for comparison with the simulation data. A key difference between the simulation and experiments is in the nucleation regime with its varying waiting times, followed by the sigmoidal trend of the JMA model in the actual experiments, which were discussed by Sheldon and Haggerty [10]. In a possible further refinement of the model such incubation times representing nucleation barriers could have been readily incorporated by effectively re-scaling the origin of time in a stochastic manner. Here this was not of interest, since the principal goal was not modeling the reaction in all its detail but only to generate non-arbitrary microstructures. The fact that this simple model follows this form and produces realistic microstructures reinforces the notion that the model incorporates correct key features of the reaction bonding process – albeit, without a nucleation barrier.

In the following sections the trends of pertinent microstructural features obtained by the simulation are presented with dimensionless ratios of the reaction parameters, followed by a discussion of the mechanisms which appear to control the formation of large pores in the final microstructure.

### 4.3 Reaction of $Si_3N_4$ vs Evaporation of $Si$ Rates

The competition between the reaction rate of  $Si$  and  $N_2$  and the rate of evaporation of  $Si$  on active surfaces is the most relevant consideration in the topological competition of growing  $Si_3N_4$  and the receding, evaporating  $Si$  particles. A large ratio of reaction rate constant,  $R$ , to evaporation constant,  $E$ , subsequently referred to as  $R/E$ , indicates immediate reaction to form silicon nitride and a high degree of accentuation of the kinetics compared with purely geometrical impingement of the silicon nitride on the more slowly receding silicon.

For this reason of increased impingement of the reaction product on the  $Si$  particles at high reaction rates, there is some correlation between the positions of the initial silicon particles and final pores of sizes comparable to the initial particle size. This is illustrated in Fig. 8a and 8b for two extreme  $R/E$  ratios of 0.3 and 300. Figure 8c gives for comparison

the initial position of the  $Si$  particles. The above mentioned effect of replacement of particles with pores is evident in the case with the high  $R/E$  ratio of 300.

Large pores in the initial packing are observed to be the locations of large final pores for both high and low reaction rates. The packing of the initial particles in Figs. 8a and 8b, unlike the other simulations, were performed in two dimensions instead of in three dimensions as previously described. This was done to illustrate the agglomeration effects of packing of circular shapes of equal diameter in 2-D, and the associated larger packing defects which arise. However, the high reaction rate microstructure to some extent has "healed" the largest pores associated with the large packing defects. This is because the  $Si_3N_4$  growth has been stifled by its impingement with neighboring  $Si$  particles everywhere except where the growth front had ample space to grow, i.e., at the large packing defects. Thus, conditions with large  $R/E$  provide for high growth rates for those nuclei which are growing unimpeded in the space of the large voids. This effect is shown clearly in the shrinking of the large pore in the upper right quadrant of Fig. 8b and in Figs. 9a and 9b which show representative microstructures of a larger scale for the two cases shown in Figs. 8a and 8b, respectively.

Finally, the amount of residual trapped silicon increases for high  $R/E$  ratio conditions due to increased impingement of  $Si_3N_4$  with the attendant encapsulation of the evaporating  $Si$ , and the reduction of the  $Si$  surface available for evaporation, as in the case of Fig. 8b for the  $R/E$  ratio of 300. Note that the unreacted  $Si$  is located in the most densely packed region of the initial particle packing, where impingement is expected to be the greatest. Conversely, a low value of the  $R/E$  ratio implies that ample silicon vapor is created and impingement is reduced. Figures 10a and 10b show the separate process kinetics plots for  $R/E$  of 0.3 and 300. Clearly, a decrease in the reaction rate  $R$  by 1000 at constant  $E$ , which spans the transition from impinging to non-impinging reactant/product fronts, results in radical differences. For the case of the  $R/E$  ratio of 300 where  $Si$  evaporation is followed by immediate consumption of the vapor by the silicon vapor starved reaction, the time for completion of the reaction is, nevertheless, shortened to only 1/4 of the time for the case of  $R/E$  ratio of 0.3.

#### 4.4 Evaporation vs Condensation Rates

A high evaporation to condensation rate ratio  $E/C$  produces higher vapor pressures and a proportionately higher reaction rate. This effect is quite strong as can be seen in Figs. 11a and 11b for the  $E/C$  ratios of 0.1 and 10 respectively. For a 100 fold increase in the  $E/C$  ratio, with all other parameters held constant, the time for completion of the reaction is shorter by a factor of 300. The additional amplification by a factor of 3 of this effect appears to be due to reduced impingement of growing  $Si_3N_4$  interfaces with the  $Si$  particles. Impingement can be reduced if the  $Si$  reactant can be effectively "stored" in the mobile vapor phase. Figure 12 shows the unreacted  $Si$  in the microstructure resulting from the increased impingement for a low evaporation rate.

#### 4.5 Density of $Si_3N_4$ Nuclei on Particles

The number,  $N$ , of initial reactive nuclei on particles, influences the reaction rate, the amount of unreacted  $Si$  and both the scale and the homogeneity of the final microstructure. At the initial stages of the reaction, a large number of nuclei per particle will increase the reaction rate due to the larger number of reaction sites. However, once a comparable amount of  $Si_3N_4$  is generated, the growth rates are equivalent. This effect is shown in Fig. 13 in terms of reaction history, microstructures, and distribution of grain and pore size distributions, for two different cases of the initial number of  $Si_3N_4$  nuclei per particle for the same  $R/E$  and  $E/C$  ratios of 3 and 1, respectively. In Fig. 13a the reaction history and the resulting distributions of grain and pore sizes together with the associated microstructure are shown for a case of high density (10) of nuclei per particles while Fig. 13b show the same corresponding information for a low density of nuclei. Extremely high density of nuclei for which the  $Si$  evaporation is blocked, stops the reaction prematurely.

If the density of nuclei,  $N$ , is low enough, fewer than 10 per particle in our observations, and the nuclei are distributed randomly, there is a statistically relevant probability for forming green structure regions with zero nuclei, resulting in large voids in the final reacted structure. Such a case is shown in Fig. 14 and Fig. 13b, with large, interconnected pores

having tortuous borders. Conversely, a large density of nuclei,  $N$ , reduces this probability and distributes the reaction product more uniformly as is clear from Fig. 13a. Note that the number of grains or nuclei per particle in real microstructures is observed to be approximately 7 in a 2-D cross section, which is close to the critical density for formation of large scale voids.

Finally, with fewer nuclei, the final average grain size is larger, because each nucleus at the initial stage represents a grain in the final stage, with the total amount of reacted material divided among those fewer grains. Quantitatively, the pore size scales with grain size, which becomes evident by the average grain to pore size ratio which remains constant (roughly at a level of 2) over a range of density of nuclei,  $N$ , from 1.0 to 10 per particle.

#### 4.6 Packing Defects

Shapes of larger pores are observed to be related to three types of defects in the packing of unreacted particles. Some of these defect types are shown in Fig. 15, and include: (1) regions of high density of packing, where there is highly restricted growth, as shown in region A of Fig. 15; (2) large scale pores, on the order of multiple particle diameters as shown in region B of the figure, where an initially low density of particles results in a large final pore; or (3) low density of nuclei which was discussed above. All three types of defects have been observed in the simulations to produce large pores in the final microstructure. The first and second cases are shown to coexist in Fig. 15, which shows the resulting microstructure with and without the particle overlay.

There is reason to believe that the large scale packing defects in the green structure such as cases 1 and 2 above exist in real structures. Large samples of uniform size powders are likely to be aggregates of dense and highly ordered crystalline domains, with a lower density of randomly packed particles in between [21,22]. A key difference between the ideal random close packing procedure and the real pressed green compacts is that the latter experience interparticle friction and associated concentrations of pressure resulting in possible localized densification.

## 5. DISCUSSION

The simulation presented here primarily provides an objective means for generating realistic appearing microstructures of reaction bonded porous silicon nitride. The fact that the grain and pore sizes and shapes appear to closely resemble those of real microstructures and that the simulation mirrors other features of the reaction process, places more credence on this technique. Moreover, the physical basis of the model implies that these microstructures can be altered in an objective manner by varying parameters which are identifiable with physical quantities of the reaction. In addition, it can be noted that, it is possible to obtain some insight into such complex phenomena as the spatial competition between the growing silicon nitride and the receding, evaporating silicon. The observed reaction mechanisms depend not only on elementary reaction rates, but on these structural effects.

The most prominent parameters in the model which govern the microstructural homogeneity, pore and grain shape and size are the reaction to evaporation ratio  $R/E$ , the evaporation to condensation ratio  $E/C$ , and the initial density of silicon nitride nuclei on particle surfaces. All of these parameters directly affect the degree of product/reactant impingement, the time for completion of the reaction and the homogeneity of the microstructure. Specifically, for the cases of low density of nuclei, high  $R/E$  ratio and low  $E/C$  ratio, significant product impingement is found to occur. In this regime, the following effects are observed: reduced overall reaction rates, a high correlation between initial  $Si$  particle positions and final pore positions, and a tendency for faster product growth in regions of lower packing density, i.e., "healing" of packing defects.

Several severe assumptions limit the present method of simulation of the complex reaction processes to the creation of schematic processing maps. Foremost, is a lack of specific functional forms for reaction rates. Therefore, we have tailored the analysis in terms of non-dimensional ratios of specific reaction constants and limited the results to trends. Also, the limit of resolution of the mesh and the two dimensional nature of the model place some degree of artificial constraints on the simulated processes. The resolution of the mesh is less problematic if the continuum processes can be thought of occurring smoothly during the discrete time increments and if the typical microstructural feature is sufficiently larger than the mesh resolution. The two dimensional nature of the simulation has been compensated for partly by using a 2-D section of a true 3-D packing of particles for the starting condition

and by appropriately adjusting the density of  $Si_3N_4$  nuclei to conserve the grain size to  $Si$  particle size. Since the microstructure is certain to evolve in all three dimensions in a statistically similar way, we have compensated for the lack of three dimensionality in an effective manner in the simulation of crack propagation through the microstructure by the introduction of an effective 3-D element based on a specific grouping of near neighbors of microstructure elements. This we describe in the companion communication [4].

Two situations are too complex to simulate to justify the relatively small effects which would be predicted to occur. The first is the isolation of large regions to either  $Si$  vapor or  $Ni$  gas reactants. The approximation of small  $Si$  vapor gradients is valid when the evaporation of the  $Si$  particles occurs homogeneously throughout the reaction. However, if structurally a reaction product (or unreacted  $Si$ ) forms a barrier around a volume larger than one particle, which can be accounted for by the simulation, the reaction within the region will naturally be choked off. Because in the typical reaction case, nearly complete nitridation is reached [10], the likelihood of the occurrence of many reactant starved regions is minimal. A second situation of considerable complexity which we have not considered is the development of reaction induced internal stresses of misfitting material. This requires a simultaneous solution of mechanical equilibrium and introduces interactions such as the effect of pressure on reaction rates. In spite of the additional insight this would have provided, the associated complexities outweigh the advantages. In the companion fracture simulation we have compensated, in part, for the absent effects of development of internal stresses by introducing material strength and stiffness variability.

With these observations and the ability to generate unique microstructures which would be difficult (if not impossible) to produce or precisely vary in the laboratory, one can then proceed to sample the fracture properties of these microstructures. In this way, not only can trends of fracture toughness be associated with processing variables, but also a mechanistic understanding of the reasons for the observed trends can be brought to the material design problem to introduce pre-selected microstructural design criteria for subsequent material processing iterations. The results of the companion fracture paths study, however, show that the degrees of effective freedom are not larger in manipulating material toughness. [4]

## 6. CONCLUSIONS

The kinetics simulation presented here captures many of the salient features of the reaction bonding process in terms of considerations for determining fracture toughness. Primarily, the generated microstructures resemble actual reaction bonded silicon nitride microstructures, in terms of the grain and pore to particle size ratios. The observed microstructural evolution mechanisms depend not only on elementary reaction rates, but also on such complex spatial, structural phenomena such as the competition between the growing  $Si_3N_4$  and the receding, evaporating  $Si$  which are summarized below.

- Key dimensionless reaction variables control the competition between the growth of the product and the recession of the reactant, specifically the reaction to evaporation ratio, the evaporation to condensation ratio, and the number of initial  $Si_3N_4$  nuclei per  $Si$  particle.
- The final pore positions are related to the particle positions in the unreacted green structure when the product growth is inhibited due to impingement of growing  $Si_3N_4$  with the  $Si$  reactant.
- Three types of packing defects may give rise to large pores in the final structure:
  1. Packing flaws on the scale of multiple particle dimensions will tend to remain as large pores in the final microstructure. This effect can be reduced, and defects can be "healed" to some extent, if the reaction takes place in a regime where the reaction rate limit is geometrical and not of a chemical kinetics nature.
  2. Densely packed regions, which are known to exist in real structures, retard growth at the early stages due to strong impingement.
  3. Regions of low density of nuclei may form statistically if the average density of nuclei is lower than some threshold. Interstitial regions which have no nuclei associated with them will be shielded from the growing reaction product, and could remain as unreacted inclusions.

## ACKNOWLEDGMENTS

This research was supported by the AFOSR under Grant AFOSR-91-0263C. For this support we are grateful to Drs. G. Haritos and W. Jones. We acknowledge many stimulating discussions with our collaborator Dr. J.S. Haggerty of the MIT Materials Processing Center, whose experience with this material was invaluable. We also thank Professor H. Frost of Dartmouth College for the data on the particle coordinates in dense random packed spheres.



## REFERENCES

- [1] B.W. Sheldon and J.S. Haggerty, *Ceramic Engng. Sci. Proc.*, **9**, (1988), 1061.
- [2] J.S. Haggerty, "Synthesis and Properties of Reaction Bonded Silicon Nitride Made from High Purity Si Powders", in *Ceram. Trans*, **42**, *Si-Based Structural Ceramics*, edited by B. Sheldon and S. C. Danforth. American Ceramic Society, Westerville: OH, p. 29, (1994).
- [3] F. Haubensak, A. Lightfoot, A.S. Argon and J. S. Haggerty, *J. Mater. Sci.*, submitted for publication.
- [4] F. Haubensak, V.V. Bulatov and A.S. Argon, *Journal of Computer-Aided Materials Design*, in this issue.
- [5] A. Lightfoot, J. Sigalovsky, and J.S. Haggerty, *Ceram. Eng. Sci. Proc.*, **13**, (1992), 1024.
- [6] A.J. Moulson, *J. Mater. Sci.*, **14**, (1979), 1017.
- [7] K.Kijima, and S. Shirasaki, *J. Chem. Phys.*, **65**, (1978), 2668.
- [8] B.W. Sheldon, "Determination and Analysis of Rate Controlling Mechanisms During the Formation of Reaction Bonded Silicon Nitride from Laser-Synthesized Silicon," Sc.D. Thesis, MIT, Cambridge, MA, (1988).
- [9] F. Riley, *Mater. Sci. Forum*, **47**, (1989), 70.
- [10] B.W. Sheldon, and J.S. Haggerty, *Ceram. Eng. Sci. Proc.*, **10**, (1989), 784.
- [11] P. Popper and S.N. Ruddlesden, *Trans. Brit. Ceram. Soc.*, **60**, (1961), 603.
- [12] L. Kadanoff, *Physics Today*, **39**, (1986), 7.
- [13] A.J.C. Ladd and D. Frenkel, in "Cellular Automata and Modeling of Complex Physical Systems", edited by P. Manneville, N. Boccara, G.Y. Vichniac, and R. Bidaux, Springer Proceedings in Physics: New York, **Vol. 46**, (1990), p. 243.

- [14] B. Chopard and M. Droz, "Cellular Automata and Modeling of Complex Physical Systems," edited by P. Manneville, N. Boccara, C. Y. Vichniac and R. Bidaux, Springer Proceedings in Physics: New York, **Vol. 46**, p. 130 (1990)
- [15] R. Bidaux, N. Boccara and H. Chate, in "Cellular Automata and Modeling of Complex Physical Systems", edited by P. Manneville, N. Boccara, G. Y. Vichniac, and R. Bidaux, Springer Proceedings in Physics: New York, **Vol. 46**, p. 73 (1990).
- [16] D. Dab and J. P. Boon, in "Cellular Automata and Modeling of Complex Physical Systems", edited by P. Manneville, N. Boccara, G.Y. Vichniac, and R. Bidaux, Springer Proceedings in Physics: New York, **Vol. 46**, p. 257 (1990).
- [17] M.P. Anderson, G.S. Grest and D. J. Srolovitz, *Phil. Mag.*, **59**, (1989), 293.
- [18] H. J. Frost, *Acta Metall.*, **30**, (1982), 889.
- [19] J. L. Finney, *Proc. Royal Soc.* **319A**, (1970), 479.
- [20] A. Lightfoot, J. Sigalovsky and J.S. Haggerty, *J. Am. Ceram. Soc.* submitted for publication.
- [21] W. R. Rhodes, *J. Am. Ceram. Soc.*, **64**, (1981), 19.
- [22] E. A. Barringer and H. K. Bowen, *J. Am. Ceram. Soc.*, **65**, (1982), C199.

## APPENDIX I. SURFACE TENSION AND GRAIN BOUNDARY TENSION OF $Si_3N_4$ .

The excess interface energy  $\Delta E$  is a thermodynamic driving force providing for the smooth grain boundaries appearing on the micrographs. This energy is essentially the source of the surface tension in the case of a grain-pore interface, and of the grain boundary tension in the case of a grain-grain interface. In both cases, substantially large  $\Delta E$  will tend to reduce the interface area (perimeter in the 2-D case). It is rather straightforward to incorporate such interface tension effects in the present reaction model by introducing an energy penalty for the transformations that result in an increase of the interface perimeter.

More specifically, the diffusion of a grain-grain interface is described here as a net result of stochastic transformations of the silicon nitride cells near the boundary of a grain with one orientation into the silicon nitride cells of a neighboring grain with another orientation. If we introduce an energy penalty,  $\Psi_{GB}$ , per unit increment of the grain boundary perimeter then the rates of such mass-exchange transformations are computed as

$$\delta P_{GB \text{ motion}} = C \exp\{-A\Psi_{GB}\Delta n_{GB}\}\delta t, \quad (AI.1)$$

where  $\Delta n_{GB}$  is an increase in the number of the grain boundary segments associated with a given transformation,  $C$  and  $A$  are constants, and  $\delta t$  is a time step. The minus sign in the exponent will reduce probabilities of transformations resulting in an increase of the grain boundary perimeter ( $\Delta n_{GB} > 0$ ); contrariwise ( $\Delta n_{GB} < 0$ ) will enhance the probabilities of transformation reducing the grain boundary perimeter. Clearly, such transformations will tend to make the grain boundaries smoother in a natural way.

In the case of the free surface, a single surface element is allowed a possibility of translating to a neighboring empty site that is adjacent to the same grain. Likewise, the kinetic rates for such translations are computed as

$$\delta P_{\text{surface diffusion}} = C \exp\{-A\Psi_S\Delta n_S\}\delta t, \quad (AI.2)$$

where  $\Delta n_s$  is an increase in the number of the grain surface segments associated with a given translation and  $\Psi_s$  is the energy per surface segment for such an increase to occur. By choosing appropriate values for  $C$  and  $A$ , the rates given by (AI.1) and (AI.2) can be adjusted relative to the rates of the nitridation reaction, evaporation, and condensation. On

the other hand, the two rates can be made higher or lower relative to each other by choosing parameters  $\Psi_{GB}$  and  $\Psi_S$  appropriately. Accordingly, by varying these parameters, grain boundaries and surfaces can be made smoother or rougher, as needed.

## Appendix II. Density of $Si_3N_4$ Nuclei

It is desirable to relate the 2-D equivalent density of nuclei,  $(N^g/N^p)^{2D}$ , to the 3-D experimentally measured density,  $(N^g/N^p)^{3D}$  where  $p$  stands for the  $Si$  particle, and  $g$  stands for the reacted  $Si_3N_4$  grain.

By standard stereology, when a cut is taken through particles packed into 3-D,

$$\frac{A^p}{A^{tot}} = \frac{V^p}{V^{tot}}, \quad (\text{AII.1})$$

where  $tot$  indicates the total section area and volume.

Assuming that the same is true for the fully reacted structure we obtain,

$$\frac{A^g}{A^{tot}} = \frac{V^g}{V^{tot}}. \quad (\text{AII.2})$$

Thus,

$$\frac{A^g}{A^p} = \frac{V^g}{V^p}. \quad (\text{AII.3})$$

In the 2-D section through the unreacted  $Si$  green structure and fully reacted structure,

$$A^p = N^p \bar{a}^p \quad (\text{AII.4})$$

$$A^g = N^g \bar{a}^g \quad (\text{AII.5})$$

where  $N^p$  and  $N^g$  are the number of particles and grains respectively,  $A^p$  and  $A^g$  are the total areas of the particles and grains respectively, and  $\bar{a}^p$  and  $\bar{a}^g$  are the average areas in the sectioned layer of the particles and grains.

Thus,

$$\left( \frac{N^g}{N^p} \right)^{2D} = \frac{\bar{a}^p A^g}{\bar{a}^g A^p} = \frac{\bar{a}^p V^g}{\bar{a}^g V^p} \quad (\text{AII.6}).$$

Then, using the approximation of spherical grains and  $Si$  particles, we obtain for the ratio of the maximum cross-sectional areas

$$\frac{\bar{a}^p}{\bar{a}^g} = \left( \frac{V^p}{V^g} \right)^{2/3}. \quad (\text{AII.7})$$

Assuming further that the ratio of the average cross-sectional areas is the same, it follows that

$$\frac{\bar{a}^p}{\bar{a}^g} = \frac{a^p}{a^g} = \left(\frac{v^p}{v^g}\right)^{2/3} = \frac{V^p/N^p}{V^g/N^g}, \quad (\text{AII.8})$$

where  $v^g$  and  $v^p$  are the volumes of  $Si_3N_4$  grains and  $Si$  particles respectively.

Combining equations (AII.6), and (AII.8), we obtain the result,

$$\left(\frac{N^g}{N^p}\right)^{2D} = \left[\left(\frac{N^g}{N^p}\right)^{3D}\right]^{2/3} \times \left(\frac{V^g}{V^p}\right)^{1/3}. \quad (\text{AII.9})$$

The term  $\left(\frac{V^g}{V^p}\right)$  is the ratio of the total volume of the reacted grains to the total volume of the initial  $Si$  particles, or simply the reaction volume expansion parameter 1.22.

For an average grain size of 100 nm and initial particle size of 250 nm, we obtain a 3-D nuclei density of 19.1 per  $Si$  particle and using equation (AII.9) we obtain an equivalent 2-D density of nuclei of 7.5.

- Figure 1      Representative microstructure of reaction bonded silicon nitride.
- Figure 2      Radial distribution function of coordinates for centers of spheres obtained from a molecular dynamics simulation of the structure of dense random packing of spheres, using the approach of Finney [19].
- Figure 3      Distribution of dense randomly packed spheres in 3-D obtained by a molecular dynamics program, subsequently sampled by a plane, giving a 2-D starting structure for the RBSN reaction simulation.
- Figure 4      The overlapping of the 2-D arrangement of random circles by a hexagonal mesh defining the cells for the cellular automata reaction simulation. The material inside the circles represents particles, black cells are  $Si_3N_4$  nuclei.
- Figure 5      Pore size distributions for real and simulated microstructures. The simulated structure had reaction parameters as follows:  $R/E = 0.3$ ,  $E/C = 1$ ,  $N = 25$  (initial density of nuclei).
- Figure 6      Distributions of pore shape parameters for real, (a), and simulated, (b), microstructures of RBSN. The simulated structure had reaction parameters as follows:  $R/E = 0.3$ ,  $E/C = 1$ ,  $N = 7.6$ .
- Figure 7      (a) Simulated history of completion of the RBSN reaction as a function of time ( $\chi$  is the total transformed fraction) showing Johnson-Mehl-Avrami kinetics; (b) experimental thermo-gravimetric results of Sheldon and Haggerty [1] for the RBSN reaction. The four curves are for four separate observations.
- Figure 8      Simulated microstructures for low ( $R/E = 0.3$ ): (a), high ( $R/E = 300$ ); (b), ratios of reaction/evaporation rates, and (c) showing positions of initial random packed particles. Packed particles were equal diameter discs packed in 2-D to illustrate agglomeration effects and the tendency of the high  $R/E$  simulation to "heal" packing defects. ( $E/C = 1$ , Nuclei density,  $N = 10$ .)

Figure 9      Simulated RBSN microstructure: (a), for  $R/E = 0.3$ ,  $E/C = 1$ ,  $N = 25$ ; and (b), for  $R/E = 300$ ,  $E/C = 1$ ,  $N = 25$ ;

Figure 10     Relative concentrations of various reaction species: (a), for low reaction/evaporation ratio ( $R/E = 0.3$ ); and (b), for high  $R/E$  ratio ( $R/E = 300$ ). ( $E/C = 1.0$ ,  $N = 25$ , mesh dimension =  $10^3 \times 10^3$  for both cases).



- Figure 11      Relative concentrations of various reaction species: (a), for high evaporation/condensation ratios ( $E/C = 10.0$ ); and (b), for low  $E/C$  ratio ( $E/C = 0.1$ ). ( $R/E = 3$ ,  $N = 10$  for both cases).
- Figure 12      Simulated microstructure for low evaporation to condensation ratio showing unreacted silicon and pore distribution for case given in Fig. 10 (a).
- Figure 13      Simulated microstructures, (a), grain size and pore distributions and kinetic curves of relative concentrations of reaction species for high number nuclei per particle ( $N = 10$ ); and (b) for low numbers of nuclei per particles ( $N = 1$ ) ( $R/E = 3$ ;  $E/C = 1$  for both cases).
- Figure 14      Simulated microstructure with density of nuclei  $N = 7.3$  ( $R/E = 300$ ,  $E/C = 1$ ).
- Figure 15      Simulated microstructure for high reaction evaporation ratio and low density of nuclei: (a), final microstructure, and (b), same as (a) with overlay of initial particle distribution. Notice the large pores in region A of high initial packing density, and in region B denuded of initial particles.

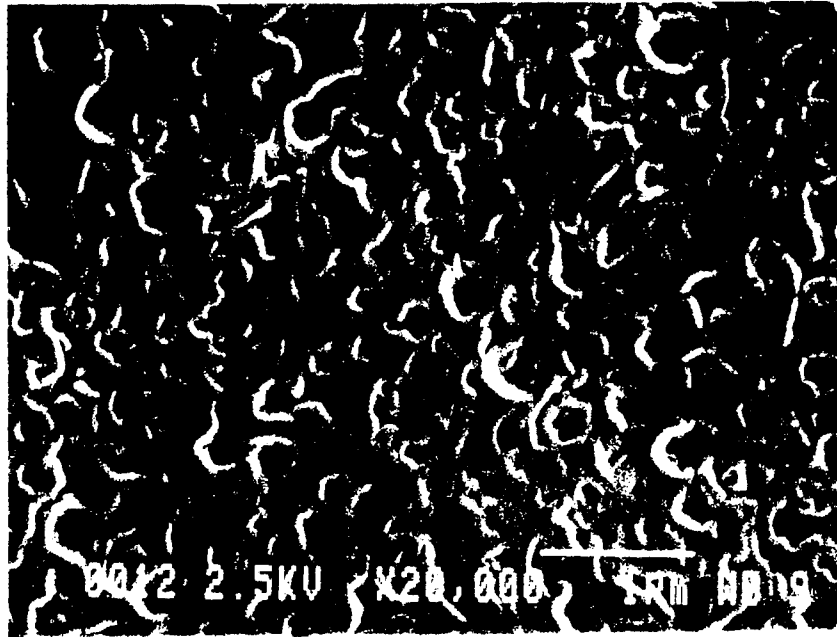


Figure 1      Representative microstructure of reaction bonded silicon nitride.

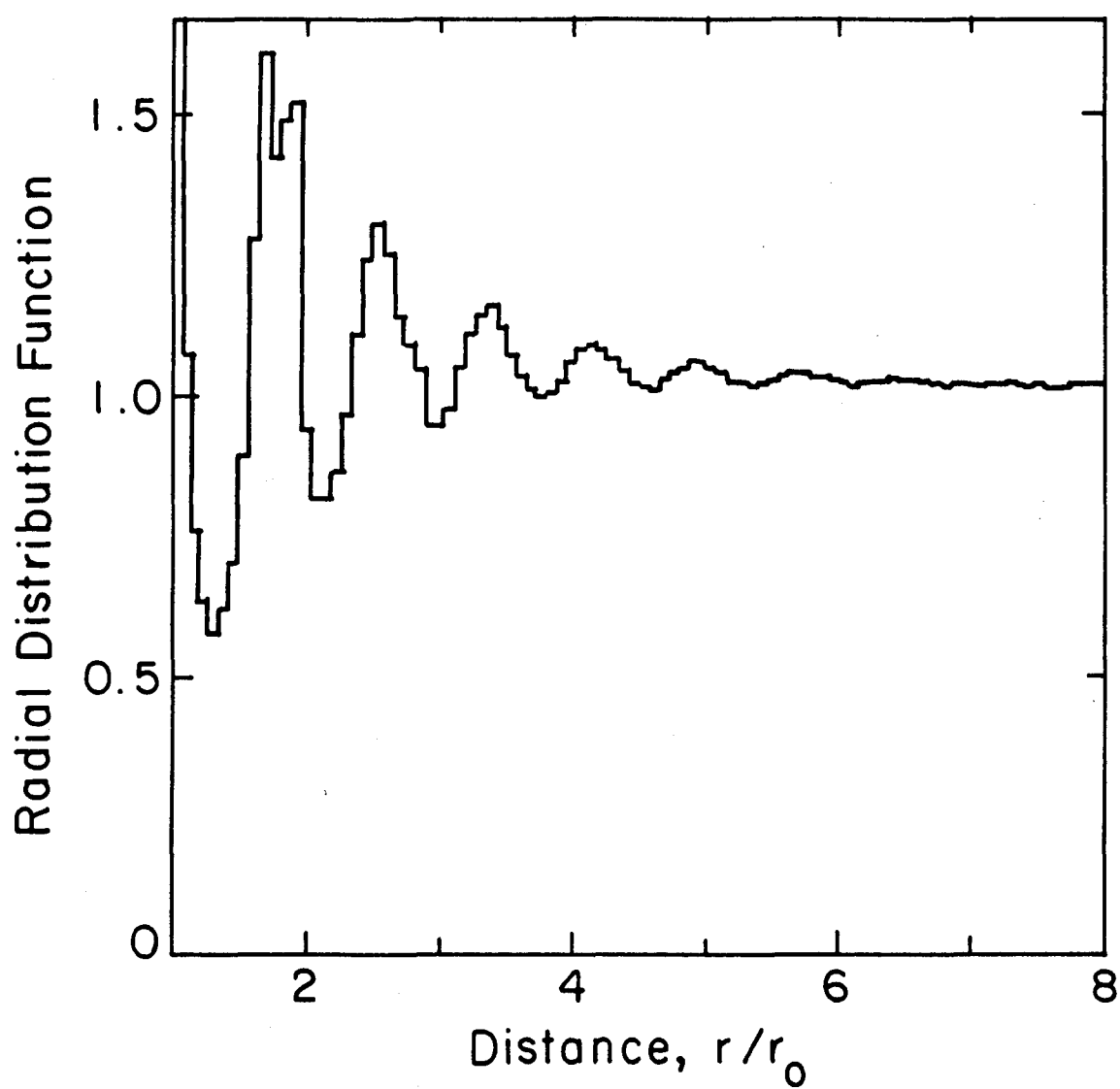


Figure 2

Radial distribution function of coordinates for centers of spheres obtained from a molecular dynamics simulation of the structure of dense random packing of spheres, using the approach of Finney [19].

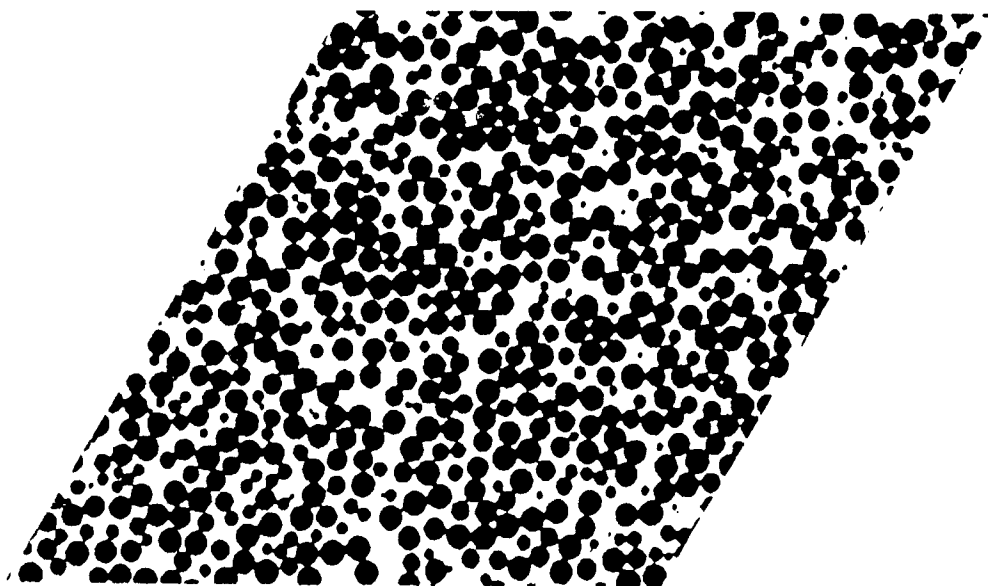


Figure 3      Distribution of dense randomly packed spheres in 3-D obtained by a molecular dynamics program, subsequently sampled by a plane, giving a 2-D starting structure for the RBSN reaction simulation.

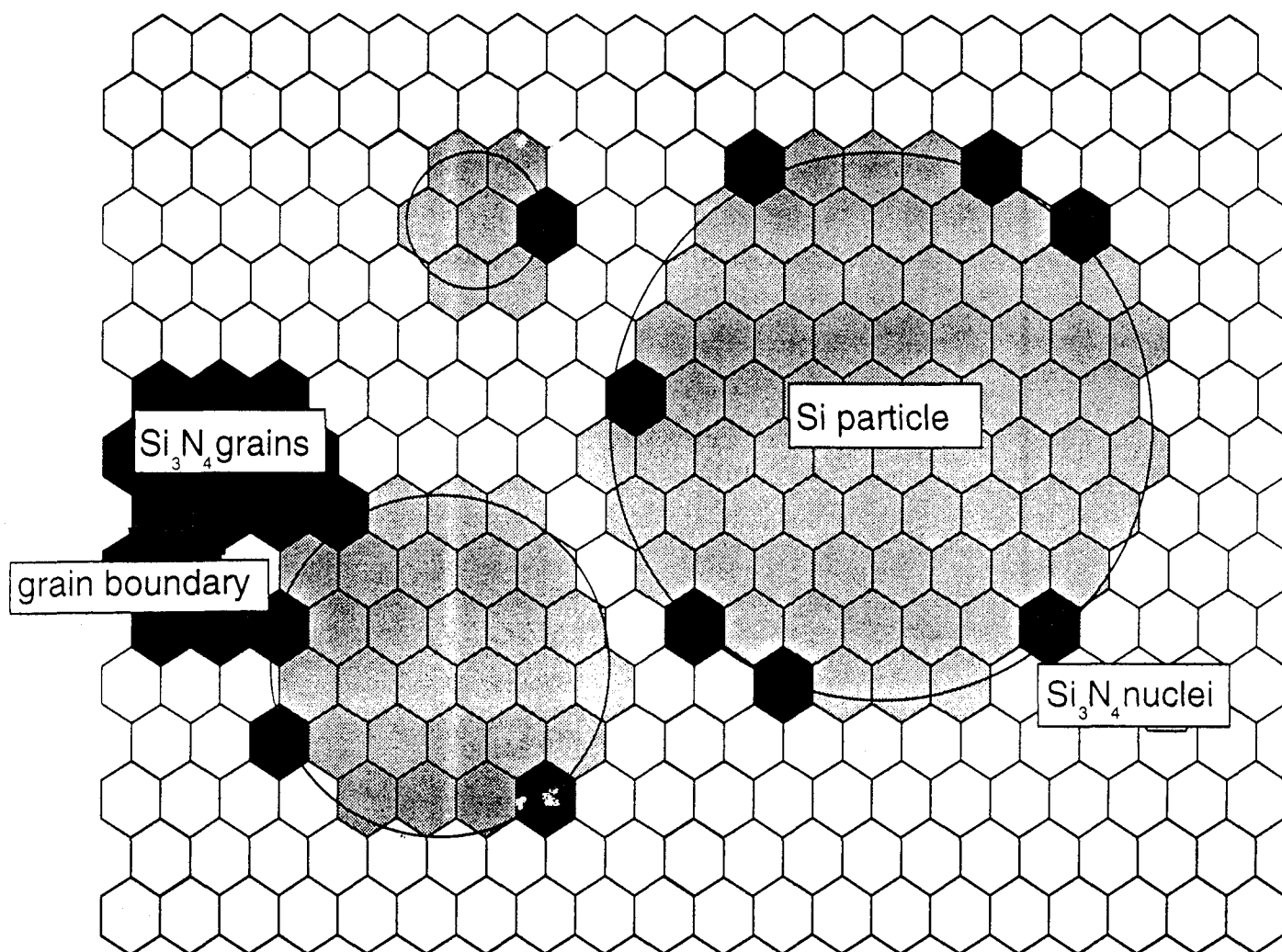


Figure 4 The overlapping of the 2-D arrangement of random circles by a hexagonal mesh defining the cells for the cellular automata reaction simulation. The material inside the circles represents particles, black cells are  $\text{Si}_3\text{N}_4$  nuclei.

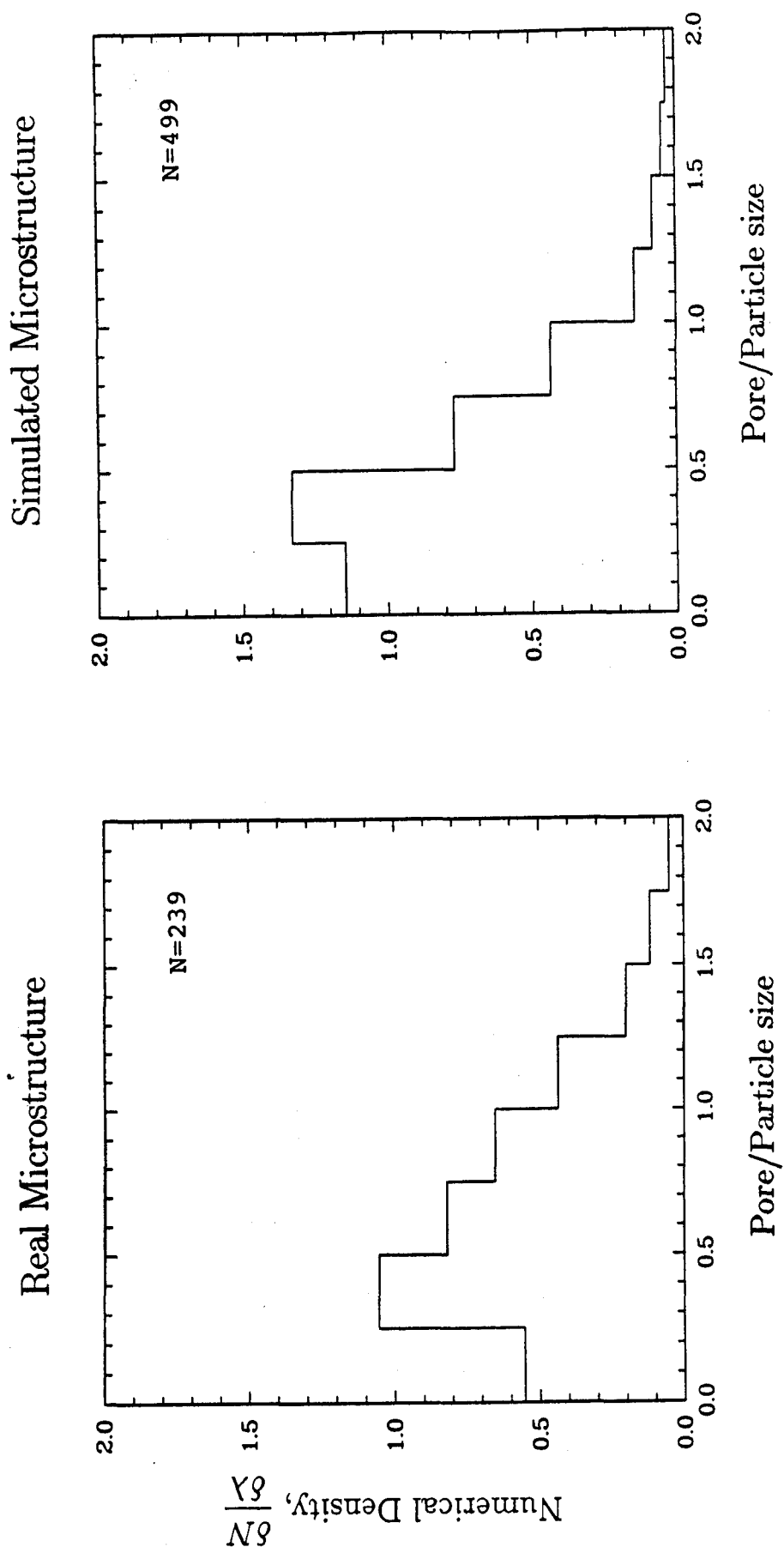


Figure 5 Pore size distributions for real and simulated microstructures. The simulated structure had reaction parameters as follows:  $R/E = 0.3$ ,  $E/C = 1$ ,  $N = 25$  (initial density of nuclei).

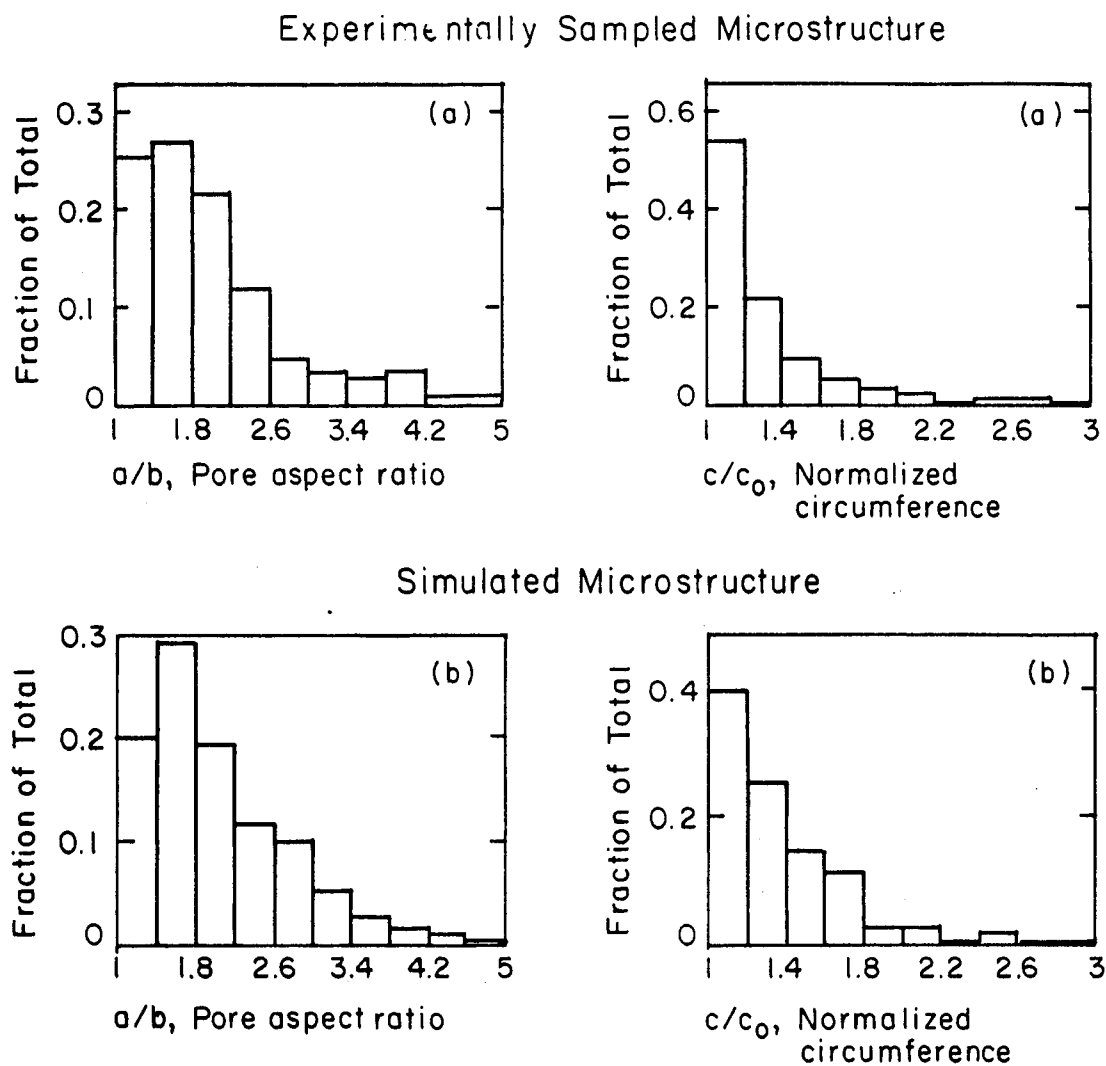


Figure 6 Distributions of pore shape parameters for real, (a), and simulated, (b), microstructures of RBSN. The simulated structure had reaction parameters as follows:  $R/E = 0.3$ ,  $E/C = 1$ ,  $N = 7.6$ .

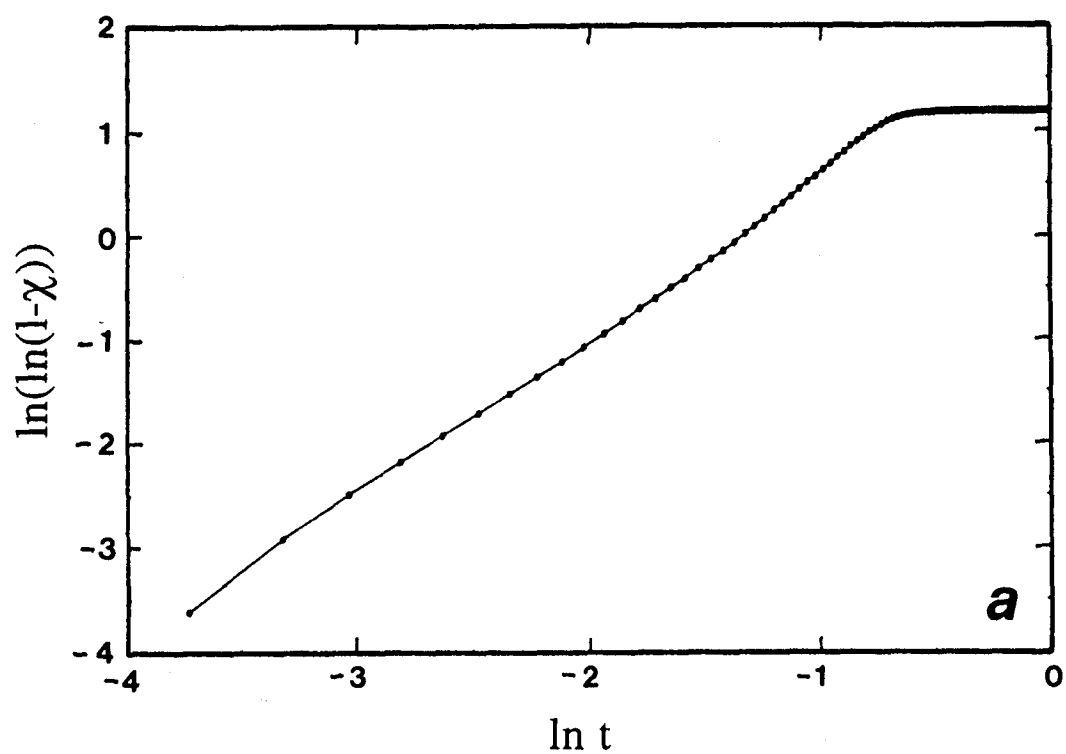


Figure 7

(a) Simulated history of completion of the RBSN reaction as a function of time ( $\chi$  is the total transformed fraction) showing Johnson-Mehl-Avrami kinetics; (b) experimental thermo-gravimetric results of Sheldon and Haggerty [1] for the RBSN reaction. The four curves are for four separate observations.



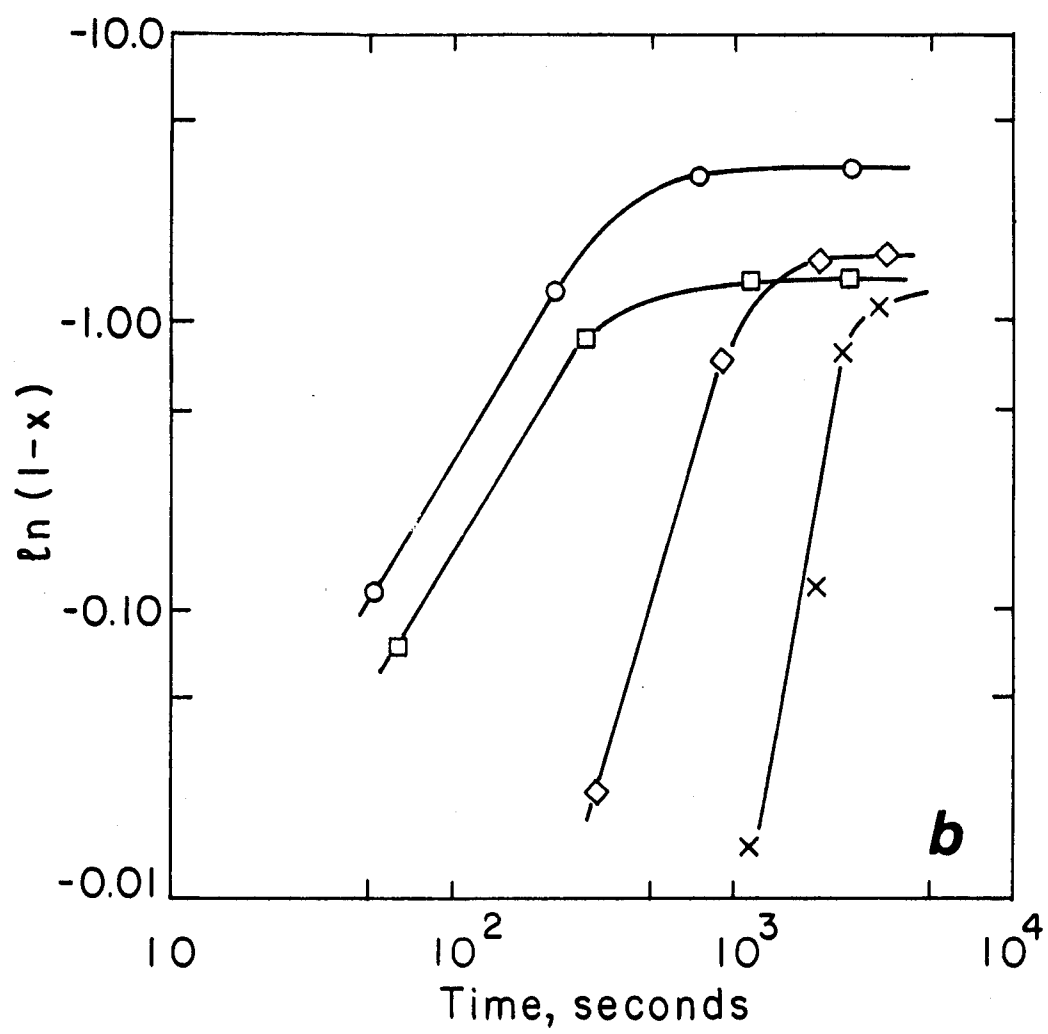


Figure 7(b)

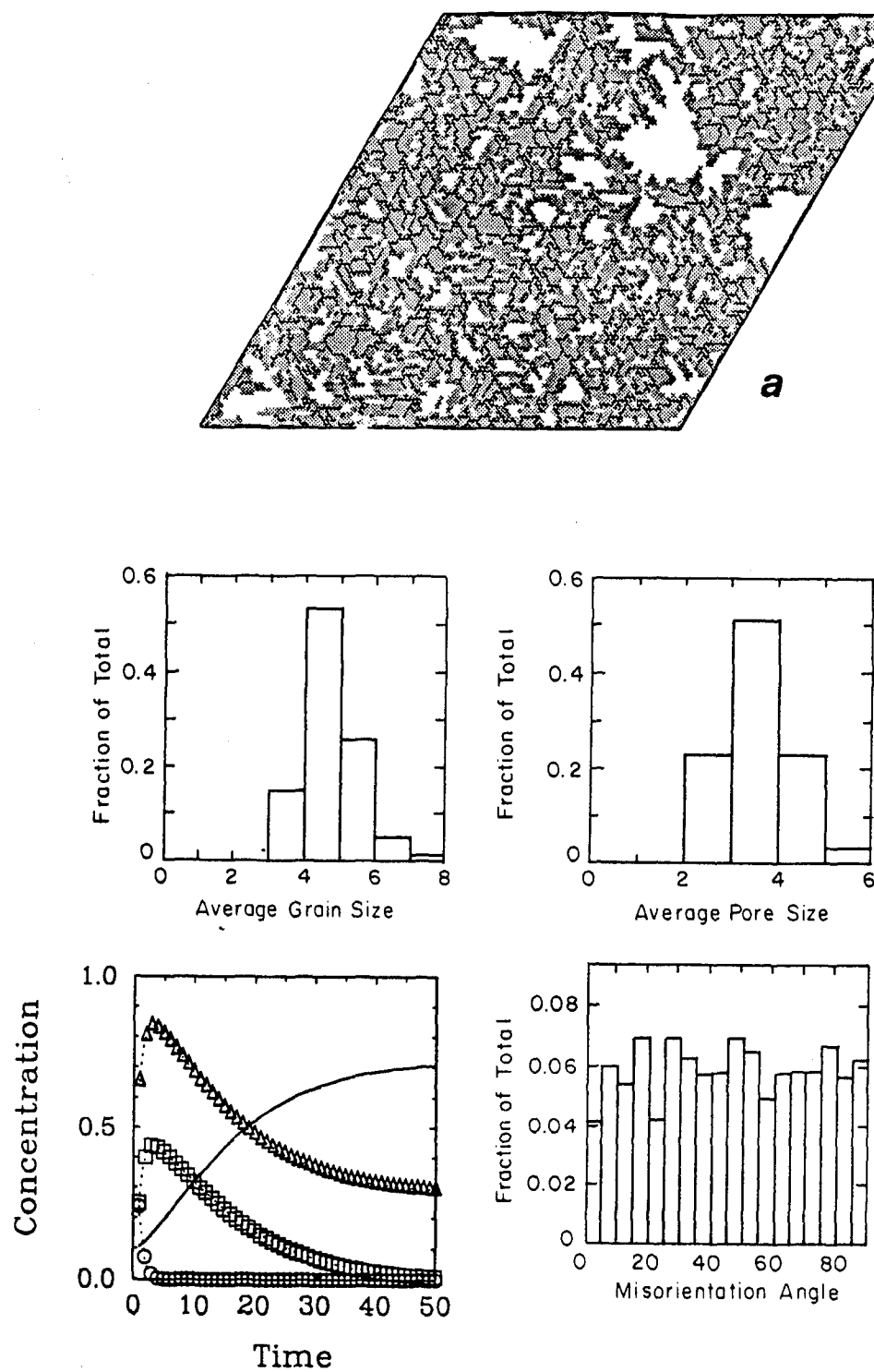


Figure 8 Simulated microstructures for low ( $R/E = 0.3$ ): (a), high ( $R/E = 300$ ); (b), ratios of reaction/evaporation rates, and (c), showing positions of initial random packed particles. Packed particles were equal diameter discs packed in 2-D to illustrate agglomeration effects and the tendency of the high  $R/E$  simulation to "heal" packing defects. ( $E/C = 1$ , Nuclei density,  $N = 10$ .)

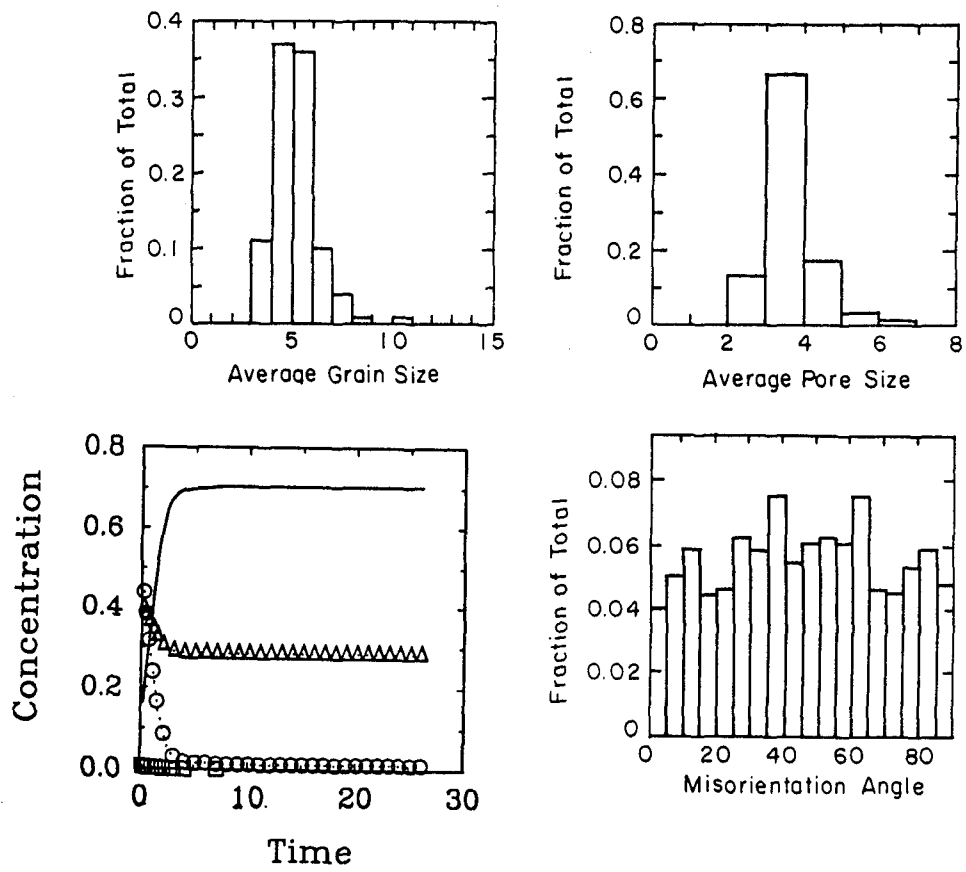
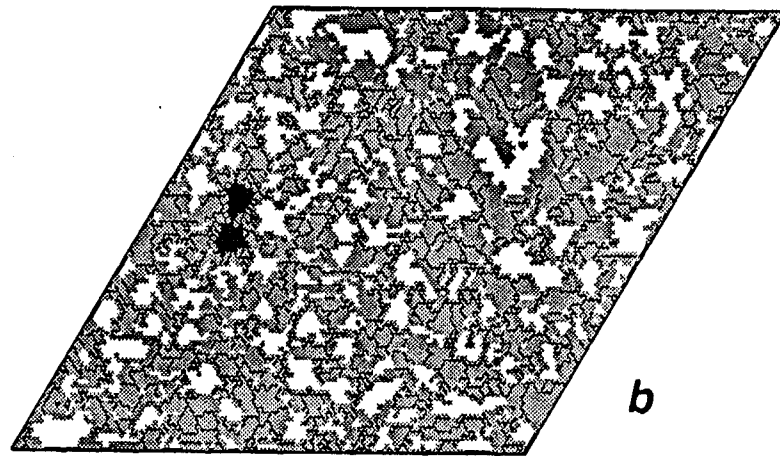


Figure 8(b)

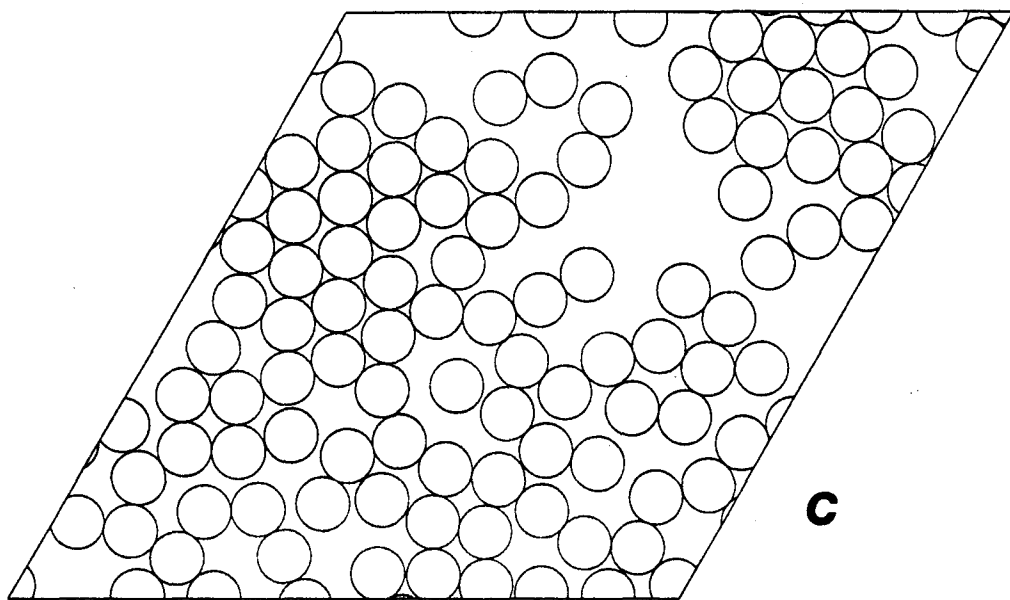


Figure 8(c)

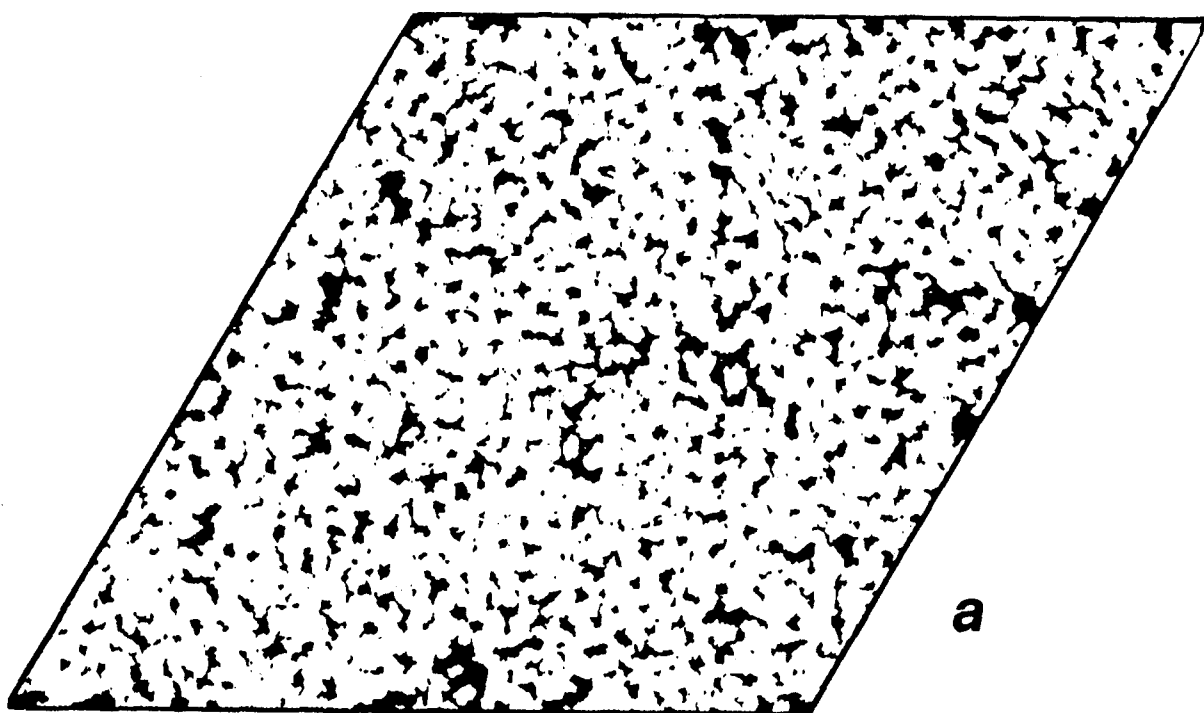


Figure 9 Simulated RBSN microstructure: (a), for  $R/E = 0.3$ ,  $E/C = 1$ ,  $N = 25$ ; and (b), for  $R/E = 300$ ,  $E/C = 1$ ,  $N = 25$ ;

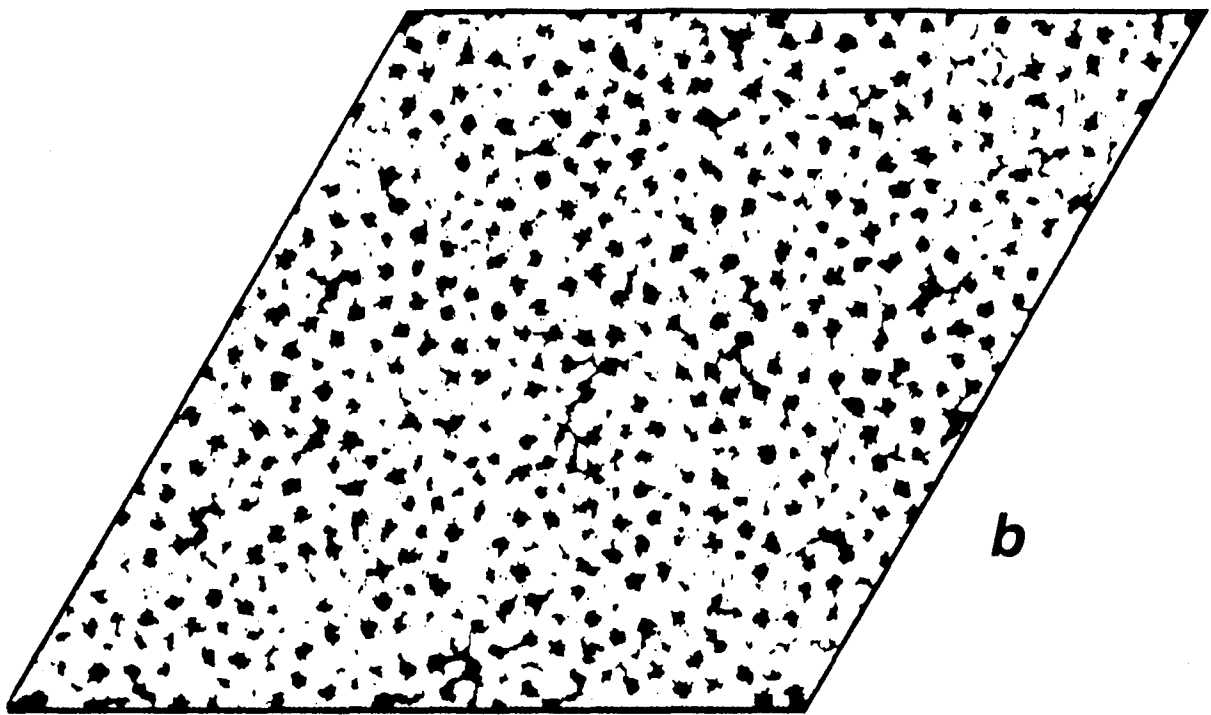


Figure 9(b)

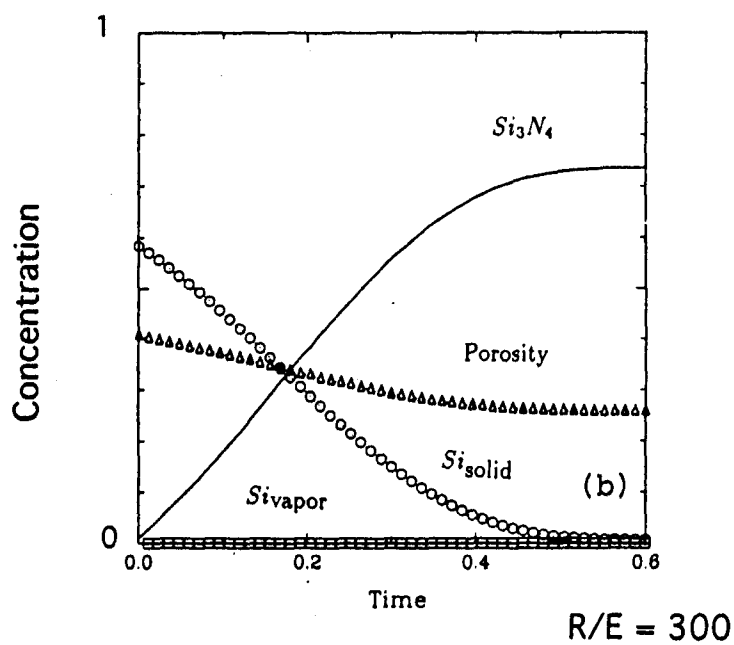
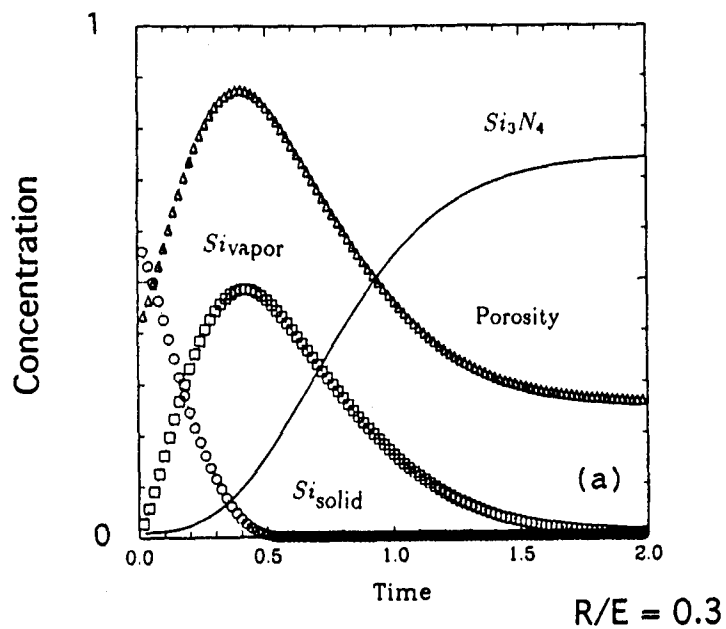


Figure 10 Relative concentrations of various reaction species: (a), for low reaction/evaporation ratio ( $R/E = 0.3$ ); and (b), for high  $R/E$  ratio ( $R/E = 300$ ). ( $E/C = 1.0$ ,  $N = 25$ , mesh dimension =  $10^3 \times 10^3$  for both cases).

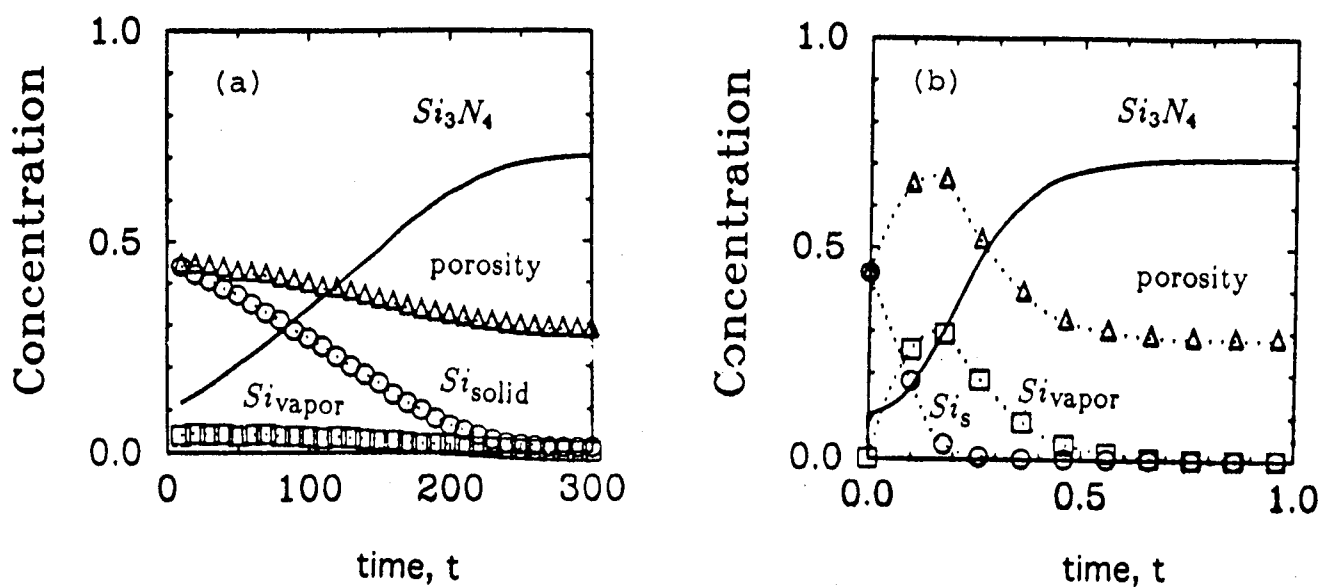


Figure 11 Relative concentrations of various reaction species: (a), for high evaporation/condensation ratios ( $E/C = 10.0$ ); and (b), for low  $E/C$  ratio ( $E/C = 0.1$ ). ( $R/E = 3$ ,  $N = 10$  for both cases).

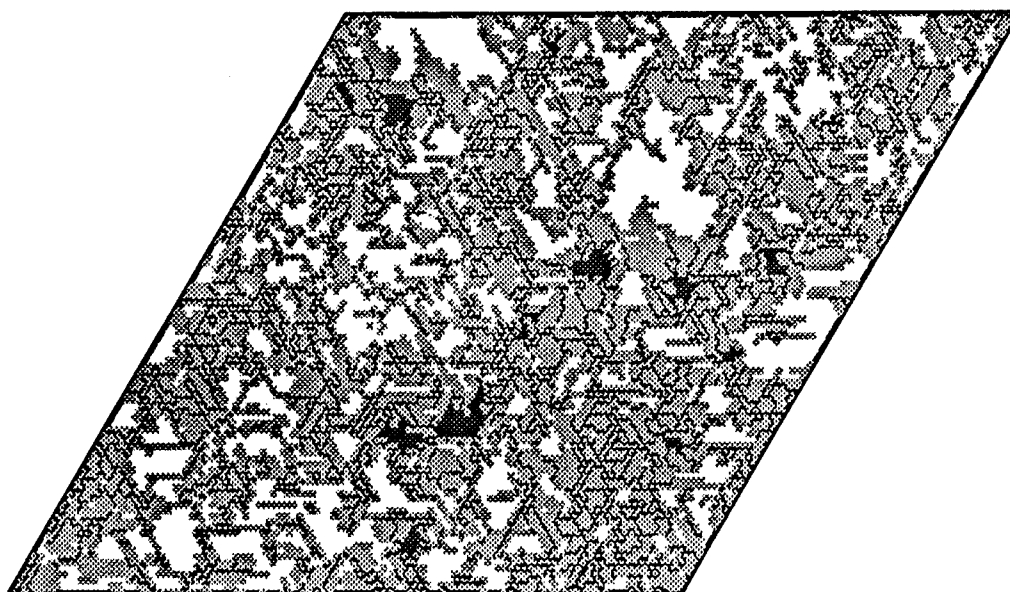


Figure 12 Simulated microstructure for low evaporation to condensation ratio showing unreacted silicon and pore distribution for case given in Fig. 10 (a).



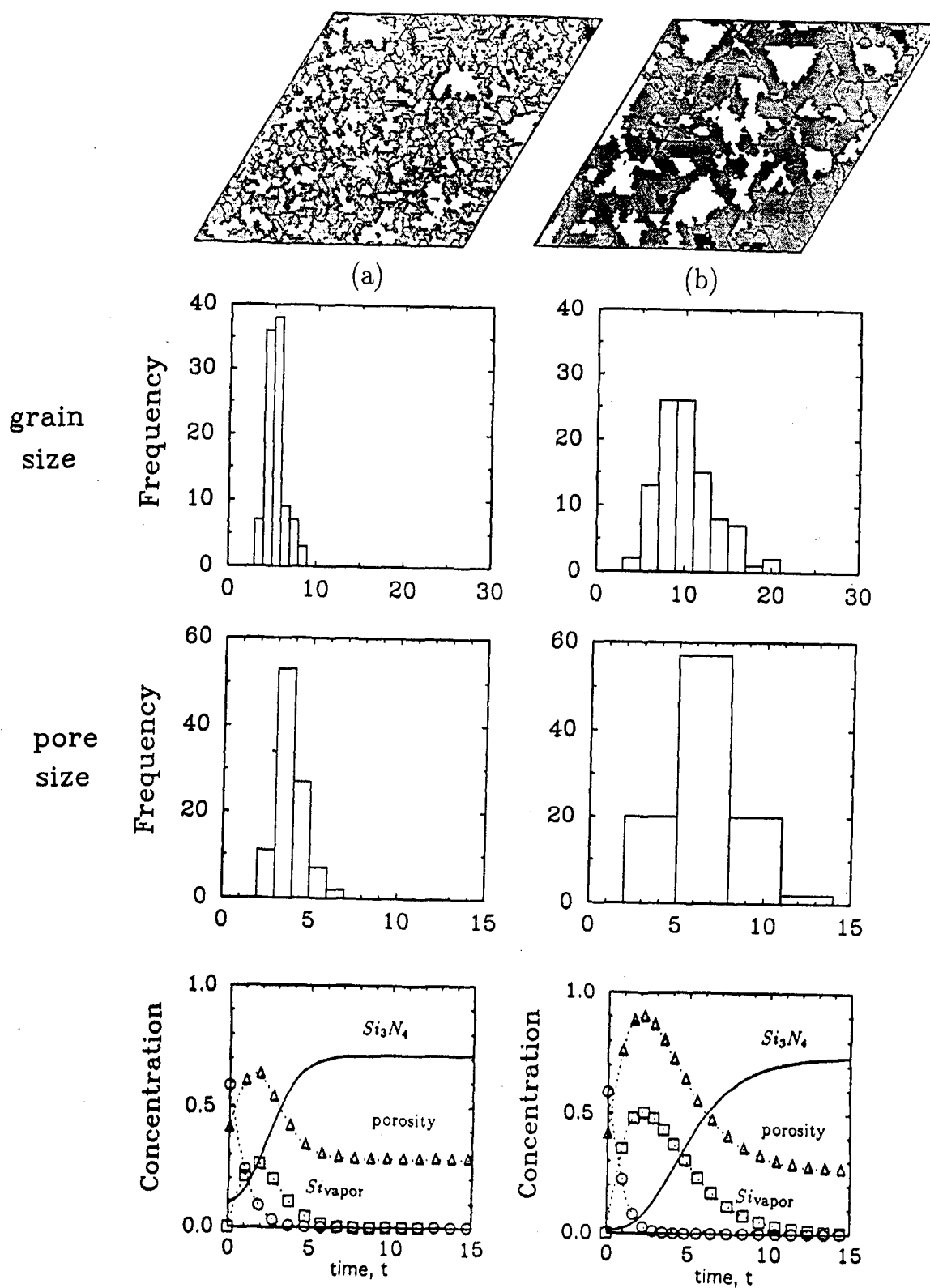


Figure 13 Simulated microstructures, (a), grain size and pore distributions and kinetic curves of relative concentrations of reaction species for high number nuclei per particle ( $N = 10$ ); and (b) for low numbers of nuclei per particles ( $N = 1$ ) ( $R/E = 3$ ;  $E/C = 1$  for both cases).

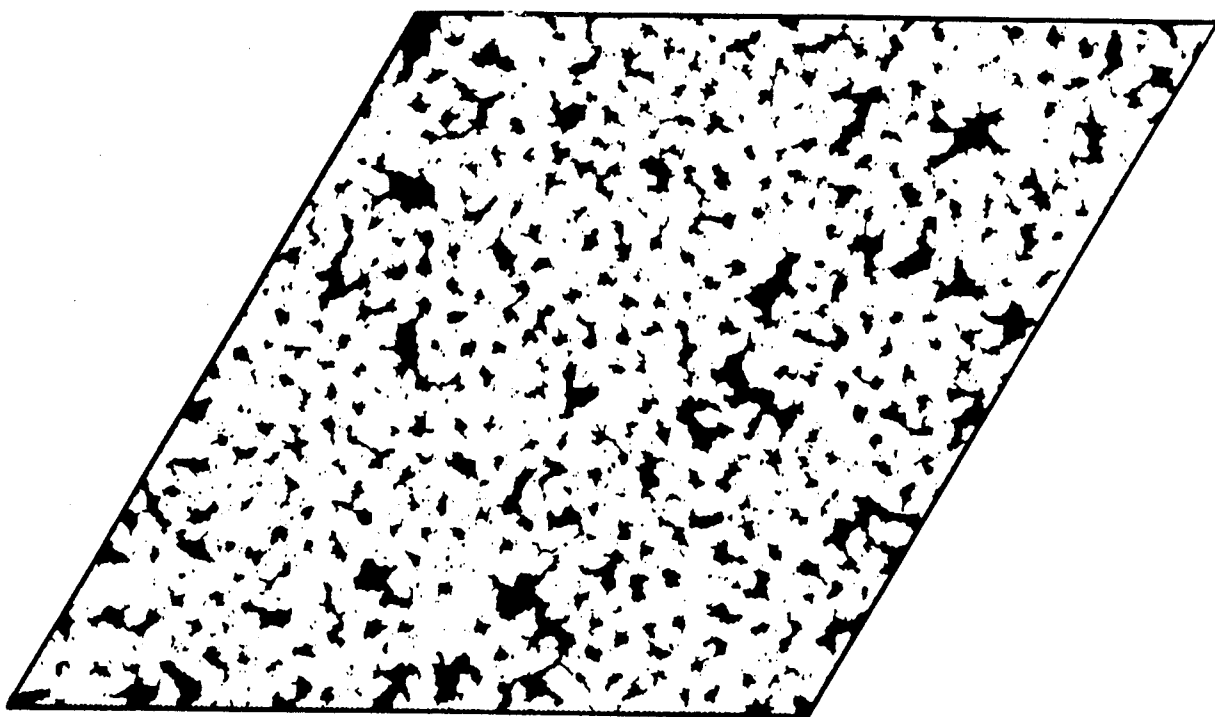


Figure 14 Simulated microstructure with density of nuclei  $N = 7.3$  ( $R/E = 300$ ,  $E/C = 1$ ).

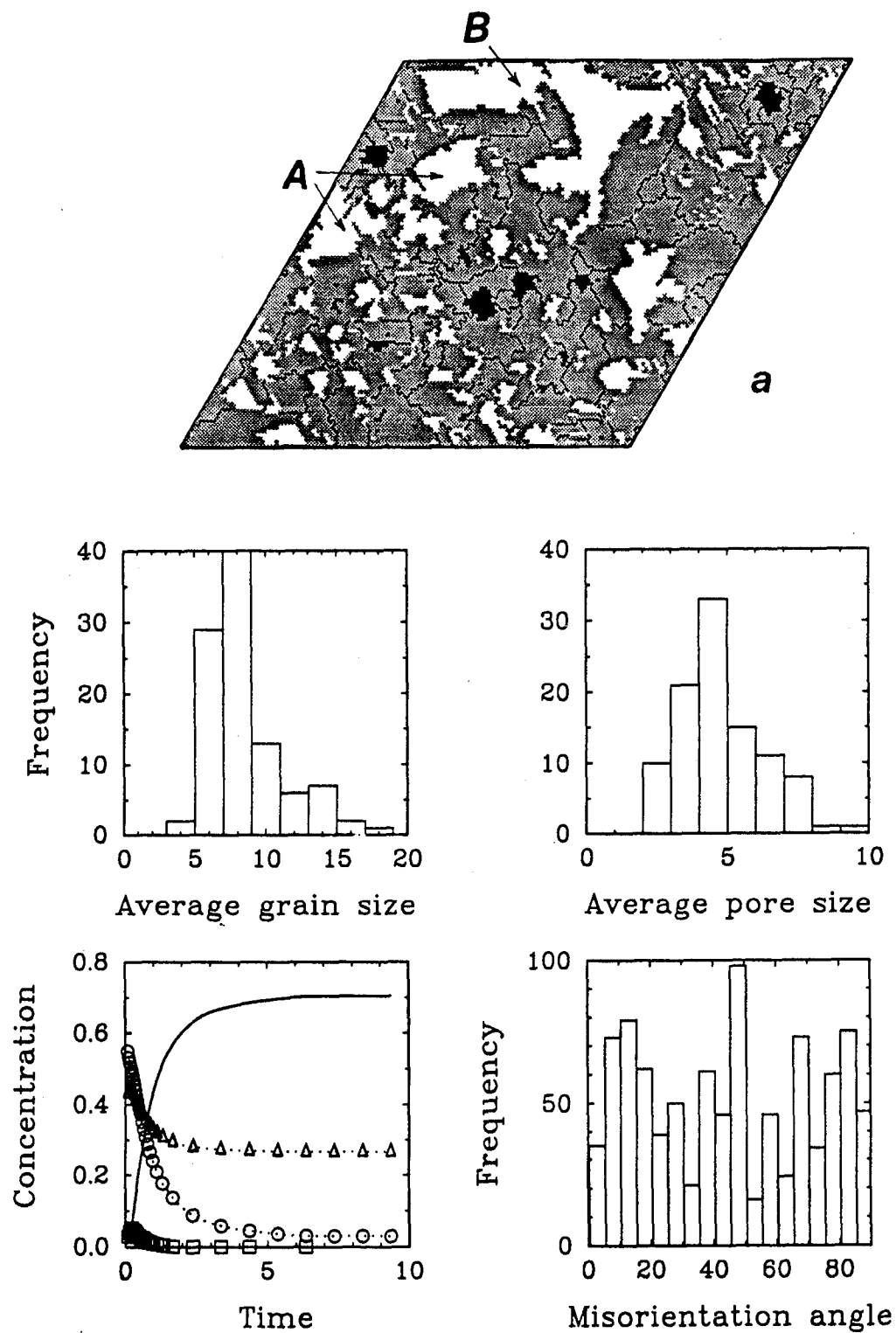


Figure 15

Simulated microstructure for high reaction evaporation ratio and low density of nuclei: (a), final microstructure, and (b), same as (a) with overlay of initial particle distribution. Notice the large pores in region A of high initial packing density, and in region B denuded of initial particles.

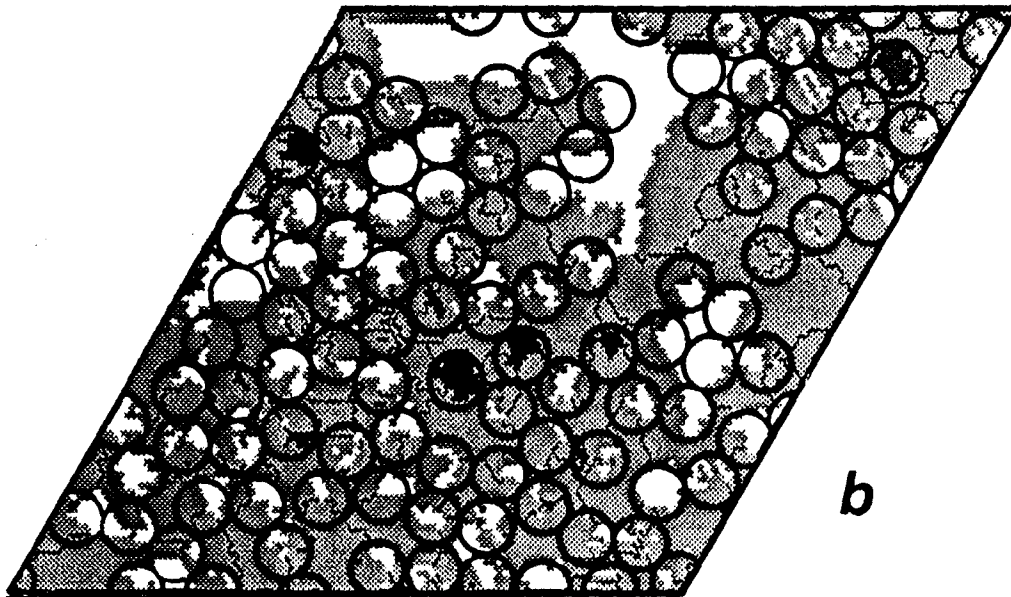


Figure 15(b)

APPENDIX E. "Simulation of Crack Propagation Resistance  
in Brittle Media of High Porosity"

F.G. Haubensak, V.V. Bulatov, and A.S. Argon,  
submitted to J. Computer Aided Materials Design

# **SIMULATION OF CRACK PROPAGATION RESISTANCE IN BRITTLE MEDIA OF HIGH POROSITY**

F. G. Haubensak,\* V. V. Bulatov, and A.S. Argon\*\*

Massachusetts Institute of Technology, Cambridge, MA 02139

## **ABSTRACT**

The crack propagation resistance through a porous or microstructurally heterogeneous brittle solid with local variability in strength and stiffness has been simulated. Specifically, the simulation probes the behavior of porous brittle materials in the range of porosity less than cellular materials and greater than microstructures which fall under the category of dilute porosity. The simulation plane consists of a triangular network of points interacting with each other through both linear central force springs and bond angle springs incorporating an appropriate element of a non-central force contribution. Explicit microstructural details were incorporated into the model and the simulation was first carried out under a condition of uniaxial tensile strain in order to investigate the mechanisms of sub-critical damage evolution leading to quasi-homogenous fracture. In order to investigate material strength and stiffness variability on the scale of a representative volume element for coherent fracture events in a crack tip stress gradient, the explicit microstructural results were incorporated into a simulation with boundary conditions characteristic of the displacement field of an infinite Mode I crack. To impart some 3-D realism to the primarily 2-D simulations a special 2-D super element was devised which incorporated variability information as might be sampled by a crack front in 3-D.

---

\* present address, Department of Materials Science, Stanford University, Stanford CA

\*\* author for correspondence.

For a given porosity, in general, only small differences were found between nominally diverse microstructures in terms of their tensile toughness, maximum strength and elastic moduli. The strongest dependence of the overall fracture toughness was found to come from the average porosity. The variability in local element strength and stiffness on the scale of the porosity produced highly tortuous crack paths roughly on the scale of the chosen representative volume element. The tortuosity of the crack was largest where local variability of strength and stiffness was uncorrelated. Examples of microcrack toughening and crack bridging were observed.

## LIST OF SYMBOLS

### SYMBOL DEFINITION\*

$A$	fracture surface area
$A_o$	total fracture surface area
$E$	Young's modulus
$E_o$	Young's modulus for fully dense material
$G_c$	critical energy release rate of porous material
$G_{co}$	critical energy release rate for fully dense material
$K_c^*$	fracture toughness of effective 2-D super element for 3-D application
$K(\sigma, k)$	fracture toughness of a microstructure having element strength $\sigma$ and stiffness $k$
$N$	number of nodes in simulation
$\mathcal{N}$	population size
$U^e$	elastic strain energy of bond extension
$U^\omega$	elastic strain energy associated with flexure of the angle between bonds $ij$ and $ik$
$a_o$	equilibrium bond length
$b$	empirical exponential pre-factor relating porosity and elastic modulus
$b_o$	equilibrium bond angle term
$c_{ijk}$	bond angle (watch spring) stiffness



$c(x)$	coefficient of variation of variable $x$
$\vec{f}_i$	force on a site due to pairwise and 3-body interactions
$f_b^*$	grain boundary bond strength
$f_m^*$	bulk (matrix) bond strength
$g_i$	energy release rate of RVE, ( $= wr_u$ )
$\bar{g}$	population average energy release rates of RVE's
$k_{ij}$	linear spring constant
$\bar{k}$	population average value of bond spring constant $k$ in large assemblies
$k_o$	peak stiffness of a microstructural element
$p$	average porosity
$r_{ij}$	scalar distance between sites $i$ and $j$
$r_u$	size of the RVE chosen to derive properties of effective 3-D super element
$s(x)$	standard deviation of variable $x$
$\vec{u}_{ij}$	unit vector connecting sites $i$ and $j$
$w$	tensile toughness, fracture work per unit volume of a microstructural element tested in tension
$\omega_i$	area per-site of the triangular spring network
$\omega_{ij}$	area per-bond of the triangular spring network
$\Phi$	total elastic strain energy

$\epsilon$	strain in bond or RVE
$\epsilon_c$	rupture strain of an individual matrix bond
$\epsilon_m$	terminal fracture strain of a microstructure element or RVE
$\nu$	Poisson's ratio
$\sigma_i$	stress tensor at a microstructure nodal element or RVE
$\sigma_{ij}$	stress on a bond connecting nodes $i$ and $j$
$\bar{\sigma}$	population average value of bond strength
$\sigma^*$	peak strength of an effective 2-D super element for 3-D application
$\sigma_c$	peak strength of individual matrix bond in the porous microstructures
$\sigma_o$	peak strength of a microstructure element
$\chi$	two variable correlation parameter

**\*Properties italicized are local properties, global properties are not italicized.**

## 1 INTRODUCTION

The understanding of the mechanical behavior of heterogeneous, and more specifically, porous materials, is of increasing technological interest. Research has concentrated mostly on materials with dilute porosity [1], and on highly porous cellular structures which have relative densities as low as 0.3 [2]. For each of these extremes of porosity there are mechanical models that are based on assumptions about the specific forms of the microstructure. In each case, extrapolations can be made to intermediate porosities with some limited success. However, there is a fundamental lack of understanding of behavior of materials within the intermediate range of porosities ( $0.15 < p < 0.85$ ), exhibited by reaction bonded ceramics.

The lack of understanding of the fracture behavior of materials within this intermediate range of porosities stems from the fact that the interaction of a macro-scale crack with heterogeneous microstructures is generally beyond the scope of analytical treatment. For a planar crack in the dilute porosity limit, two first order effects reduce the fracture toughness. The relationship,  $K_c = \sqrt{EG_c}$ , implies that the toughness is related directly to  $E$ , the elastic modulus, and  $G_c$ , the critical energy release rate. The average elastic modulus decreases roughly as  $E \sim E_o \exp(-bp)$  where  $E_o$  is the Young's modulus of the fully dense material,  $p$  is the average porosity and  $b$  is found experimentally to be typically 2-5 [3]. In the absence of other effects which disperse the action away from the parting plane, the critical energy release rate  $G_c$  for a planar crack is proportional to the fracture surface area,  $A = (1 - p)A_o$ , such that  $K_c = \sqrt{G_{co}E_o(1 - p)}\exp(-bp/2)$ , where  $G_{co}$  is the critical energy release rate of the fully dense material.

Any crack interaction with porosity which disperses the action away from the plane of fracture produces non-planar fracture that will modify this relationship, by such effects as microcracking, crack bridging, and other three dimensional shielding effects. As porosity increases and the elastic interaction based on pores becomes important, the approximation of isolated pores breaks down. This can be expected to occur roughly near a porosity of 16%, the percolation threshold of random porosity in three dimensional structures.

Similarly, cellular structure models can be extended with some success into the intermediate porosity regime [2]. However, the fracture of cellular materials, especially open cell structures for which no sharp crack tips exist, is qualitatively different from the fracture of higher density materials. The mechanism of crack propagation in cellular materials in tension is typically a

succession of localized breaks of individual cell ligaments or cell walls. Random microstructures with densities higher than the percolation threshold of random spheres in 3-D (16%), no longer require structural order in order to support load. Therefore, this limit also serves as an approximate reference point for the limit of applicability of cellular structure fracture models.

The material of particular interest in the present study is reaction bonded silicon nitride,  $Si_3N_4$  (RBSN), with a porosity roughly in the range of 0.25. Figure 1 shows a typical microstructure of RBSN interacting with a macro-crack. It shows relatively equiaxed pores with a relatively narrow pore size distribution in the submicron range. In addition to these widespread features, RBSN also contains a certain small concentration of unreacted  $Si$ , and in some cases larger pores, possibly resulting from initial packing defects among  $Si$  particles. Parallel experiments with RBSN revealed that cracks primarily propagate along grain boundaries, bridging the pores, as is shown in Fig. 1.

In a related companion computer simulation [4], we have presented a reaction kinetics model for the production of porous  $Si_3N_4$  to establish the important reaction parameters that give rise to microstructures similar to the real microstructures presented in Fig. 1, and to identify the most important factors of the reaction which control the microstructures. In the present simulation the fracture processes in such computer generated microstructures were explored with the goal of determining the cause-effect and mechanistic relationship between features of the microstructures and their toughness which can be translated to the real RBSN system, and can perhaps guide the further process developments for this material.

The approach taken here is to examine the fracture response of realistic porous microstructures of RBSN in as much detail as possible. The microstructural details are incorporated into numerical simulations by mapping them onto appropriate degrees of freedom of the spring network model, as described in Section 2. Also discussed in Section 2 is the implementation of numerical solutions and other pertinent simulation issues. In Section 3 we begin with simulations of the fracture behavior of brittle porous microstructures of RBSN modeled in detail. The results discussed in Sections 3.1 and 3.2 show that: (1) reliable estimates of the fracture toughness of RBSN from the detailed simulations of the crack propagation within the spring network model in a sample of reasonable size are hardly feasible because of the high computational cost; (2) evolution of damage in the porous microstructures involves sequences of fracture cascades leading to bridging of the inter-pore ligaments. While the first observation is rather discouraging, the second implies that substantial computational effort can be saved by using a less detailed description, where the porosity

is incorporated not explicitly but in the form of variations in local strength and stiffness on the scale of, pore clusters in a homogenized model. The results of simulations of crack propagation in such homogenized materials with prescribed variability in local properties are presented in Section 3.3. The first two sub-sections, 3.3.1 and 3.3.2, describe fracture patterns and qualitative trends in fracture toughness observed in simulations of spring network models with various idealized distributions of local strength and stiffness ranging from very large variations to no variations at all in one or both local properties, and from no correlation to perfect correlation of them. These results demonstrate the range of changes in the fracture properties as functions of the local property variations. To incorporate more realistic variations and co-variations of local properties of porous RBSN microstructures in the homogenized description, stiffnesses and strengths were sampled on large statistical ensembles of super elements of the size  $10 \times 10$  corresponding to the typical effective pore clusters (Sub-section 3.3.3). Then, this information was incorporated in crack propagation simulations of the homogenized model, now representing the porous RBSNs. The results discussed in Sub-section 3.3.4 show that local variations in stiffness and strength in RBSNs are strongly correlated in all cases. The origin of this correlation is in the porosity, which largely defines the overall fracture properties of the porous microstructures. Although interesting trends are observed and discussed in Section 4, the nature of the RBSN formation reaction, limits the possibilities of designing tougher materials by changing the reaction conditions.

## 2 MODELING FRACTURE IN A BRITTLE POROUS MATERIAL

### 2.1 Outline of the Numerical Model

The model for the elastic response of a solid in two dimensions that has been used in the simulations described here is based on the properties of a triangular network of springs, and is similar to the models used first by Kirkwood [5] and by Keating [6] and more recently by Srolovitz and co-workers [7]. The network is composed of a two dimensional triangular lattice of points connected by bonds. These bonds combine two different forms of interactions: first a two-point interaction in the form of linear harmonic springs, and a three-point interaction in the form of angular springs referred to as "watch" springs [7], associated with the angles formed by the adjacent linear springs originating from the network nodes, as shown in Fig. 2. This triangular network bond model of interconnected extensional springs and their angular flexing interactions, as used here, is adequate for obtaining numerical solutions for various problems in plane isotropic elasticity. In the form the procedure is used by us, it is well suited to provide stress and associated displacement field solutions for systems incorporating dispersed heterogeneities.

In brittle materials with quasi-homogeneously dispersed porosity the list of possible fracture toughening mechanisms that can be present include microcracking and other crack tip shielding mechanisms, such as: crack deflection, crack branching, and crack bridging analogous to fiber reinforcement by locally tough elements. These mechanisms do not involve plasticity. Therefore, in the present model we exclude any dissipative and non-linear effects such as stress induced shear transformations, fiber pull out, and large strain deformation, and consider only local variations in strength and stiffness of the representative components, as is the case with RSBN for which the model is principally intended.

The energy  $\Phi$  of the 2-D triangular network is made up of a sum of bond stretching and angle flexing forms:

$$\Phi = \frac{1}{2} \sum_i^N \sum_j^6 U^e(r_{ij}) + \sum_i^N \sum_{j,(k=j+1)}^6 U^\omega(r_{ij}, r_{ik}) \quad (1)$$

where  $r_{ij}$  is the distance between node (or site) "i" and any one of its nearest neighbor nodes "j",  $U^e$  represents the energy of bond extension, and  $U^\omega$  represents the energy associated with the flexure of the angle between bonds "ij" and "ik". The factor 1/2 in the first term accounts for the

double counting over all network nodal points  $N$ , in the entire field. The bond extension and angle flexing components of the elastic strain energy can be given specifically as:

$$U_{ij}^e = \frac{1}{2}k_{ij}(r_{ij} - a_o)^2 \quad (2)$$

$$U_{ijk}^\omega = \frac{1}{2}c_{ijk}(\mathbf{u}_{ij} \cdot \mathbf{u}_{ik} - b_o)^2 \quad (3)$$

where  $\mathbf{u}_{ij}$  and  $\mathbf{u}_{ik}$  are unit vectors pointing from the node “ $i$ ” to its nearest neighbors “ $j$ ” and “ $k$ ”,  $(\cdot)$  represents a scalar product,  $a_o$  and  $b_o$  are the equilibrium bond length and the cosine of the bond angle in the unstressed network, and  $k$  and  $c$  are the extensional and watch spring stiffness constants of the stretch and angle flexing interactions of the network nodes.

To relate the spring network response to the actual material elastic properties we note that the isotropic elastic properties of a homogeneous network can be given by its Young’s modulus  $E$  and Poisson’s ratio  $\nu$ , and that these can be expressed as functions of the two stiffness constants  $k$  and  $c$  [7]. Thus, the effective local isotropic elastic constants  $E$  and  $\nu$  for a uniform spring network model are given by:

$$E = 3ka_o^2 \frac{2ka_o^2 + 7c}{6ka_o^2 + 7c} \quad (4)$$

$$\nu = \frac{2ka_o^2 - 7c}{6ka_o^2 + 7c} \quad (5)$$

Therefore, by a proper choice of  $k$  and  $c$  the network represents the 2-D response of a linear elastic isotropic solid in the full range of Poisson’s ratios from  $-1$  to  $1/3$ . The hexagonal symmetry assures isotropy [8].

In order to reach mechanical equilibrium of the spring network model corresponding to a minimum of the energy function  $\Phi$ , the conjugate gradient method was used, which is known to be numerically efficient and robust [9]. This technique allows to systematically adjust the coordinates of the lattice cites by iteration, so that in the end of the iterative procedure the net force on each site is zero within a pre-set tolerance and the minimum of  $\Phi$  is reached. Such states of mechanical equilibrium are conveniently characterized by a local stress tensor definable for each lattice cite (or bond) of the spring network. For operational purposes we have used the well-known atomic stress tensor introduced first by Born and Huang [10], properly modified to account for: (1) the non-central forces due to the last term in equation 1, and (2) the periodic boundary conditions employed in some of our simulations, as explained in detail in Appendix I. In that appendix we

also demonstrate that the conjugate gradient energy minimization technique together with the generalized definition of the local stress constitute a fully versatile method for solving boundary value problems for strain/stress distributions in isotropic plane elasticity. It is shown that the stress fields obtained for a simple test case using both the conjugate gradients method with the spring network and the finite elements method for the corresponding continuum approach, closely match each other. This correspondence and the ease with which the variability of micro-mechanical properties of RBSN is mapped onto the spring network make it a natural choice for the specific purposes of the present simulation.

## 2.2 Method of Implementation of Solutions

In order to probe the elastic properties, the tensile strength and the crack propagation resistance of a microstructure, appropriate local elastic and strength properties were assigned to the spring network that overlays the field of heterogeneities such as pores, grains, inclusions, and interfaces. The microstructure volume element was then subjected to a set of uniaxial border displacements, and was equilibrated internally using the conjugate gradient method until the overall elastic strain energy function  $\Phi$  was minimized for a unit level of border displacement which served to scale the internal displacement field distribution. Forces in all extensional bonds were then computed and the bond subjected to the highest ratio of tensile force to bond strength was identified. This ratio was then used to re-scale the border displacements associated with the probing "unit" imposed strain. The stiffness of this bond was set to zero to account for its fracture. The mesh was then unloaded, reloaded, and equilibrated to identify the next weakest bond that can be broken, and so on, until the entire cross section of the microstructure volume element was severed. To obtain stress-straining curves, the overall system stress on the microstructure was found as the area average of the node level stress tensors (see Appendix).

The fracture criterion was chosen as a maximum tensile bond force as the best approximation to a critical local tensile stress over other criteria, such as critical energy density or bond extension, since brittle solids fracture when local stresses reach the intrinsic material strength.



### 2.3 Fracture Behavior of Individual Porous Microstructures

In the first simulation the fracture behavior was determined of individual microstructures of a size substantially larger than the representative volume elements (RVE) of the porous material. Parenthetically, we note here that the size of an appropriate RVE should be chosen as a small multiple of interpore spacings, over which smoothed behavior is obtained, as we will discuss in more detail in Section 2.4 below.

The microstructures used in the simulation were generated primarily by a Monte Carlo reaction kinetics simulation referred to in Section 1 above [4]. In addition we have, performed some simulations on microstructures obtained by digitizing actual micrographs of typical RBSN samples.

The specific larger scale microstructure elements used in the simulation were mapped onto the two dimensional triangular network in the following manner. Solid elastic elements of the microstructure were differentiated from pores such that solid bonds have full stiffness and bonds falling into pores have zero stiffness. The fracture properties were incorporated by assigning strength to bonds. Here intergranular bonds were differentiated from the matrix bonds by assigning them a lower strength, e. g.,  $f_b^* = 0.75 f_m^*$ , where the latter stands for the strength of a bulk (matrix) bond. This value of boundary bond strength was chosen as an estimate of the strength necessary to develop the experimentally observed prevalence of intergranular fracture in polycrystalline RBSN, in a manner similar to what was done by Wang et al. [7]. Widespread intergranular fracture has been observed in high purity RBSN manufactured by Haggerty and co-workers [11] whose research has been closely linked with the present simulations. In the present model the dimension of the bond was taken to be a fraction of the grain size in order to capture some of the internal deformation gradients due to the pore and grain size distributions. At the same time, the specific fracture criterion of a critical bond strength used here approximated the actual intergranular fracture behavior of RBSN [11], as already stated. Once the spring mesh was assembled, and the strengths and stiffnesses of all bonds were assigned, the spring network of the sample microstructure was subjected to uniaxial tension by prescribing border displacements. Periodic boundary conditions were imposed on the test microstructure elements to approximate essentially infinite bodies with no free surfaces. The size of the mesh was  $64 \times 64$  nodes, approximating to a nominal dimension of 2 microns. This was usually enough to incorporate 10-20 pores of 0.1 micron dimension, i. e. a field of roughly 25 RVEs (see Section 2.4).

## 2.4 Variability of Strength and Stiffness

To explore more general behavior with greater ease, without considering specific porous microstructures, simulations were performed on continuous material in which, however, the characteristic variabilities of the porous microstructure were locally introduced. This approach was convenient to probe the effect of heterogeneities on the crack propagation resistance. Thus, for this purpose a second set of simulations was performed in the gradient field of a Mode I crack. In this case, each node represented the variable properties of a volume element. This was accomplished by introducing a series of increasing bond strength and stiffness variations randomly for each bond to obtain some idealized trends resulting from local variability. In a third, subsequent simulation the question of the dimension of the volume element was addressed, by performing a series of fracture simulations on specific microstructures that could be considered as representative volume elements (RVE)s.

In the second simulation the mesh was pre-cracked and was placed in the strain gradient field of an infinite Mode I crack which approximates a realistic crack tip environment in a solid body of large dimensions. Beyond the border of a core region surrounding the crack tip the material was considered homogenized. Inside the core region the variations due to individual bond properties were considered explicitly as they interacted with the crack. Care was taken to minimize the possible adverse effects of the borders on the crack tip by keeping the size of the core region larger than any crack tip process zone. The local fracture criterion for crack advance was taken as a maximum principal tensile stress approximated by a critical tensile bond force, as already stated above.

To explore the effect of variability of bond stiffness and/or strength, the bond properties were randomly assigned values between a maximum of 1.0, and a minimum value determined by a variance which was defined by a coefficient of variation (i. e. as the standard deviation divided by the mean). The density of the distribution of the bond properties was assumed to be constant over the range of values defined by a minimum and the maximum value (1.0). In this manner, the coefficient of variation,  $c(x)$ , in the variable  $x$  is defined as:

$$c(x) = \frac{1}{\sqrt{3}}\left(\frac{1}{\bar{x}} - 1\right), \quad (6)$$

where  $\bar{x} = (x_{\max} + x_{\min})/2$  is the mean of the distribution in which  $x_{\max} = 1$ . Thus, a variable uniformly distributed on the segment (0,1) has a maximum coefficient of variation of 0.577. In the simulation each parameter of strength and stiffness was varied either independently, or the two parameters were varied together with a prescribed correlation, established from specific simulations of properties of actual microstructure volume elements, as discussed below in Section 2.5.

## 2.5 Incorporating Microstructural Information into Stress Gradient Simulation

To make the choice of variations in strength and stiffness of the bonds and their co-variation less arbitrary, possible combinations of microstructural stiffness and strength were sampled. This was accomplished by testing a large number of small microstructure volume elements as potential representative volume elements (RVEs), extracted from a very large field of a porous microstructure by a random selection process. These microstructure VEs were tested under uniaxial stress to obtain their initial elastic stiffness and their peak stress during fracture. This is described in detail in Section 3.3.4 below.

Moreover, to introduce an element of 3-D realism where porosity in a real structure is randomly distributed into the third dimension rather than being columnar, as implied in a 2-D model, a special two dimensional “super element” was constructed by averaging the properties of three neighboring RVEs in a row, chosen randomly from a very large computer-generated microstructure as depicted in Fig. 3. The upper bound average strength and stiffness properties of such rows of 3 elements then constituted the “super element” with the desired 3-D properties, to represent an arbitrary strip of a 3-D crack front, projected into the 2-D plane. The effective strength  $\sigma^*$  of the “super element” was obtained based on the argument of Rose [12] that the average energy release rate of a strip of crack front with heterogeneities is approximately equal to the line average of the local energy release rates,  $g$ , of the neighboring crack front line elements,  $\Delta s$ , i. e. :

$$\sigma^* = \frac{K_c^*}{\sqrt{\pi r_u}} = \frac{\sqrt{E(\sum_{i=1}^3 g_i \Delta s)/3\Delta s}}{\sqrt{\pi r_u}} = \sqrt{\frac{E \sum_{i=1}^3 g_i}{3\pi r_u}}, \quad (7)$$

where  $r_u$  is the size of the microstructural RVE used in the preliminary simulations to gather statistical data,  $g_i$  is the energy release rate (area under the stress-strain simulation of the individual

RVEs times  $r_u$  of an individual RVE), that this approximation is reasonable is demonstrated in Fig. 4 where a more exact result obtained by Bower and Ortiz [13] for a crack pinned at two tough heterogeneities and bowing into a region with lower toughness for five different ratios of the toughnesses of the two regions through which this crack advances.

The simulation which incorporated the 2-D super element was a final variant of the third simulation in which correlated strength and stiffness information of actual RVEs was considered.

### 3 RESULTS

#### 3.1 The Evolution of Damage Under Uniaxial Tension

The damage evolution in homogeneously stressed microstructure volume elements is characterized by cascades of individual bond fracture events with the fracture process almost always initiating at a pore surface and developing into a succession of breaks which comprise the evolution of a microcrack. The nature of fracture was predominantly intergranular, with 75-100% of the breaks occurring along the lower strength grain boundary bonds, as it was arranged to happen by the deliberate choice of the lower strength for the boundary bond, to parallel the experimental observations. The cascade of breaks commonly represents the sequential breaking of elements in a ligament between two pores, which is generally the smallest dimension between two adjacent pores. This was established from the observed fact that the number of breaks in the cascade correlates directly with the number of mesh elements that make up a ligament that fractures. These fracture cascades were separated often by single breaks at pore surfaces which, however, did not grow.

Figure 5 shows in considerable detail the response of a stressed microstructure volume element obtained from the digitized image of a real RBSN sample. The figure identifies the connection between the features on the stress strain curve with events on the stressed microstructure.

During the simulation when a local break is obtained, such as at the point near A, between the two central pores, the system registers a slight decrease in elastic stiffness. At this stage, for operational purposes the system is unloaded and subjected to the same unit border displacement to seek a new level of internal equilibrium, and is then reloaded until the second break is registered (at point A). The decreased stiffness (increased compliance) of the system manifests itself by an elastic loading line with reduced slope, connecting the origin to point A (not shown in the stress strain curve). We note that the second break at point A in the newly re-equilibrated microstructure occurs at a system stress *less* than the first break. This was a frequent occurrence. After this break the continued loading of the system (following the usual re-equilibration) produces a third break which now exceeds the stress of the first break. All other dotted lines falling inside the outer envelope of the stress-strain curve represent similar virtual re-equilibration and reloading processes probing the system in the computer. In a real system loaded by border displacements or by imposed external strain increments, there would be no retraction of strain, but the system

response would be given by vertical stress drops as the outer envelope stress-strain curve indicates. In this case, all individual fracture events represented by crosses falling inside the stress strain curve represent unstable fracture cascades, as those identified by A-I in the stress strain curve and located correspondingly on the microstructure.

During the evolution of damage, leading progressively to increasing concentration of fractured ligaments, the overall system modulus systematically decreases, shown by the ever decreasing slopes of the lines connecting the origin to the new fracture events. This progressive decrease in stiffness of the structure, accumulating increasing levels of breaks, is summarized in Fig. 6.

### 3.2 Uniaxial Fracture Behavior of a Series of Microstructure Volume Elements

A series of porous microstructures which were produced under systematically varied conditions, with the associated reaction kinetics simulation [4], were probed in tension for their quasi-homogeneous fracture properties. The different computer generated microstructures shown in the various parts of Fig. 7 were deemed to be realistic in appearance and within quantitative measures resembling real microstructures such as the one shown in Fig. 1. A typical control microstructure of 25% porosity and its stress-strain behavior is shown in Fig. 7a. The remaining six microstructures in Figs. 7b - 7g represent in order: a case of a higher silicon nitride nucleus density (rapid nitridation and early particle impingement) (7b); one with a higher porosity at 31% (7c); and one with a lower porosity at 20.5% (7d); a case of a significantly anisotropic grain growth condition (7e); a microstructure for a case of a low reaction to evaporation ratio, in the reaction kinetics simulation [4] producing a controlled variation in porosity distribution (7f); and finally a case involving the addition of a population of small diameter (one tenth of the normal size) silicon particles (7g). This last case was undertaken as a special simulation to compare with the experimental observation of a measured fracture toughness reduction arising from the addition of smaller  $Si$  particles, in the initial "green" material and was thought to arise possibly from different pre-nitridation particle packing effects. Details of the reaction simulations used to obtain microstructures shown in Fig. 7 are discussed by us elsewhere [4].

The corresponding stress-strain curves resulting from the simulations are also shown in Figs. 7a - 7g above their respective microstructures. In all cases the stress-strain curves presented are obtained by averaging fracture responses of four similar microstructures.

In the final stages of the simulations, when the connectivity of the microstructures is substantially reduced due to damage accumulation, the number of conjugate gradient iterations required to re-equilibrate the spring network becomes increasingly large. To reduce the computational effort, the final “tail” part of the simulation was obtained by extrapolation. For that a certain functional form was used to describe the “tail” response, which was obtained by an empirical fit to a few typical fracture responses. This same termination form was then applied to all other simulations.

Perusal of the composite stress-strain curves of these simulations shows many similarities in their shapes. Apart from the case of the anisotropic microstructures which shows markedly increased tensile toughness, all other cases show few quantitative differences apart from the primary effect of changes in porosity.

Figures 8a - 8c summarize the principal results of these simulations on specific microstructure volume elements, showing the dependence on porosity of: the Young's modulus,  $E$ , (8a); the peak strength,  $\sigma_c$ , (8b); and the fracture work per unit volume  $w$  (the so-called tensile toughness) as, (8c). In the latter the beneficial effect of the anisotropic grain growth stands out. In all other cases the porosity level is clearly the most important structure characterizing parameter, and other effects are relatively minor.

In the simulations the tensile toughness,  $w$ , was obtained as the area under the individual stress-strain curves, i. e. :

$$w = \int_0^{\epsilon_m} \sigma d\epsilon \quad (8)$$

where  $w$  is the energy per unit volume required to completely fracture the microstructure to a state of zero load support under uniaxial strain, and  $\epsilon_m$  is the strain for complete fracture of the microstructure. Typical energy densities normalized by the energy to fracture a perfect elastic solid of bulk material,  $\sigma_c \epsilon_c / 2$ , are in the range of 0.1-0.2; as Fig. 8c shows. The terms  $\sigma_c$  and  $\epsilon_c$  are the strength and strain to fracture a fully dense matrix in uniaxial tension.

The restriction of the uniaxial strain condition of loading can produce additional load support, especially at the end of the simulation, due to the absence of stress relaxation perpendicular to the loading direction. However, the magnitude of the energy contribution under the tail for strains between 0.5 and 1.0  $\epsilon_c$ , the critical strain to failure under uniaxial strain, is not a major portion of the work of fracture and scales with the total energy,  $w_{\text{tail}} = (0.3 - 0.4)w_{\text{total}}$ .

### 3.3 Fracture of a Fully Dense Reference Solid with Prescribed Variability Mimicking the Porous $Si_3N_4$

#### 3.3.1 Uncorrelated strength and stiffness variation

The properties of porous microstructures in the uniaxial tension simulations discussed above revealed that because of the porosity and the variability introduced through lower strength bonds for grain boundaries in comparison with the strength of the bulk matrix, damage accumulation was strongly clustered. This effect, which was discussed in detail in connection with Fig. 5 manifests itself in the form of cracking cascades and implies that for purposes of simulation of crack growth the material can be divided up into smaller volume elements as discussed briefly in Section 2.4 above. We have followed this approach in the second and third simulations involving crack growth, as outlined in Section 2.4.

Thus in the second simulation which we will discuss in this section we have considered the material to be free of pores in which, however, the expected clustered growth of a crack was arranged to result from material heterogeneities in either strength or stiffness, as might result from porosity in a real material, and where the variabilities in either property were taken as uncorrelated. In the third simulation the strength and stiffness of the heterogeneities were correlated on the basis of a separate uniaxial tensile simulation of the fracture behavior of RVEs of a size roughly corresponding to the cracking cascades that were observed earlier in the first set of simulations in connection with Figs. 5 and 7a - 7g. The results of this third simulation are discussed in Section 4.2 below. In both the second and third simulations we have utilized the same triangular spring network model discussed above, where however the individual "bonds", in a generalized sense, were now interpreted to represent the heterogeneities in the clustered cracking behavior, noted in the fracture response of the actual larger microstructures. The propagation of Mode I cracks through such "homogenized" material with prescribed variability was then investigated in a manner described in Section 2.5 above, leading to the findings described below.

The degree of variation of both the bond strength and stiffness was found to affect directly the extent of microcracking, crack deflection, branching and bridging behavior. For small variability, the crack path is planar. The crack samples, on the whole, the population average of element strength,  $\bar{\sigma}$ , and the average fracture toughness is that of a homogenized structure with the average



properties,  $K_c(\bar{\sigma}, \bar{k})$ . Here  $K_c = \sigma_o \sqrt{\pi a_o/2}$ , the peak fracture toughness of the heterogeneities, has been taken as the unit of toughness measure, where  $\sigma_o$  is the peak strength of the distribution of material elements of size  $a_o$  (the appropriate RVEs), now treated as a distinct “bond”. As the variation of local properties increases, the crack path becomes more tortuous, and the number of redundant breaks increases. This trend is shown in Figs. 9a - 9f for increasing coefficients of variation in “bond” strength  $\sigma_c$  of elements and in Figs. 10a - 10c for increasing coefficients of variation in “bond” stiffness  $k_o$  of elements.

The results of these two simulations with separate strength and stiffness variability are summarized in Figs. 11a and 11b respectively. In the case of local strength variability in a material with uniform local stiffness, the toughening is a direct result of the observed increase in crack complexity associated with the very substantial redundant microcracking, which could not be present in the homogeneous reference structure. This is clear from Fig. 11a and shows that the beneficial effect of relative improvement in toughening reaches a maximum with a coefficient of variation of around 0.3. In the case of the largest strength variation with  $c(\sigma) = 0.52$ , the toughening effect normalized with the toughness of the homogeneous material was 1.26, and the advancing crack splinters into a cloud of microcracks. Figure 12 shows the resulting R-curve behavior for this level of strength variability arising solely from the tortuosity of the crack profile, the extreme preponderance of redundant microcracking and the associated crack deflection. The ratio of the maximum steady state toughness to initial toughness is observed to be approximately 3 for the chosen random distribution of element strength.<sup>1</sup> By comparing this behavior with the results in Fig. 9 we note that this apparent beneficial behavior is at the expense of a lowered ultimate (plateau) toughness.

In the case of stiffness variation alone, where the material has uniform strength, the effective toughening, summarized in Fig. 11b, must result solely from crack tip shielding attributable to the random elastic inhomogeneities which then manifest themselves in crack deflection with very little associated redundant microcracking. Since the material is of uniform strength, the toughening due to stiffness variability increases monotonically. Here the average stiffness of the broken bonds is equal to the average of the entire population, suggesting no favoring of high or low stiffness bonds for fracture. Hence, any elastic shielding is due to a favorable stress redistribution arising from a

---

<sup>1</sup>In this simulation, the first 60 bonds were broken one at a time with intervening steps of equilibration, and the following 400 were broken in sets of 20 highest stressed bonds to expedite calculations, thus explaining the sparsity of simulation points for increasing numbers of breaks.

broader, and in this case only downward, distribution of bond stiffness. Thus, in comparison with a homogeneous material where all bonds have the same average stiffness, the largest toughening effect is 1.34, achieved with the largest coefficient of variation of 0.52 in bond stiffness. We note that the homogeneous reference material also maintains constant toughness by the argument that a more compliant bond absorbs proportionally more energy, yet the surrounding material has a reduced elastic modulus which is related to the bond stiffness. This demonstrates that the toughness of a homogeneous brittle material whose energy release rate is inversely proportioned to its stiffness is independent of the elastic properties, for a stress based fracture criterion.

The increase in toughness due to material variability manifests itself directly in the form of crack complexity or degree of deviation from planarity of the crack as is already clear from the insets in Figs. 9 and 10. This is demonstrated more directly by the calculated root mean square of the vertical positions of the breaks with respect to the median plane of the crack which make up the overall crack profile, and naturally includes effects of crack tortuosity and redundant microcracking. Figure 13 shows the positive correlation of the crack path deviation from planar form, with the relative toughness  $\Delta K/\bar{K}$ . The parameter  $\Delta K$  is defined as the difference between the average  $K$  sampled locally, minus the reference toughness  $\bar{K} = \sqrt{\bar{E} \times \bar{g}}$ , of a homogeneous material with average properties. Here the term  $g$  stands for the energy release rate of one severed element (bond)  $(1/2)\sigma\epsilon a_o$ , where  $\sigma$  is the local element (bond) strength,  $\epsilon$  its failure strain, and  $a_o$  is the element dimension. We note that the dependence of the normalized toughness increment  $\Delta K/\bar{K}$  on crack surface roughness is steeper for the case of stiffness variability where the material is of uniform strength and the toughness increase must be a direct consequence of crack tip shielding due to the elastic inhomogeneities. Higher complexity in crack configurations and crack tortuosity due to microcracking is a direct consequence of the strength variability as already noted above.

### *3.3.2 Effect of correlated strength and stiffness variation on crack propagation*

We note that while the abstract analysis of the second simulation discussed in Section 3.3.1 of the effects of uncorrelated variability of the strength and stiffness was quite instructive, in most real materials the strength and stiffness of material elements will be more or less correlated. This is especially the case with porous materials where pores reduce both local strength and stiffness. Thus, in preparation of a more complete third simulation discussed in Section 3.3.4 below, a variant of the

second abstract simulation was performed where the strength and stiffness of individual elements were varied together in perfect covariation and then independently, with a coefficient of variation of 0.346 for strength. The resulting effects on the crack profile are shown in Fig. 14 where now the average fracture toughness in the material with correlated strength and stiffness variation has decreased to  $\bar{K} = 0.65$  from the reference case of strength variation alone with  $\bar{K} = 0.87$ , measured relative to the fracture toughness of the perfect material.

The expected value of toughness for a cooperative effect between strength and stiffness variability is  $K_{\text{expected}}/K(\bar{\sigma}, \bar{k}) = K(\bar{\sigma} + d\sigma, k_o)/K(\bar{\sigma}, k_o) \times K(\sigma_o, \bar{k} + dk)/K(\sigma_o, \bar{k}) = 1.25 \times 1.09$  or  $1.37 \pm 0.04$ , when normalized with the homogeneous equivalent material toughness, where  $k_o$  and  $\sigma_o$  are the peak element stiffness and strength, correspondingly. The actual result for perfect covariation of strength and stiffness is a crack configuration of reduced toughness, as compared to the homogenized equivalent material,  $K(\bar{\sigma} + d\sigma, \bar{k} + dk)/K(\bar{\sigma}, \bar{k}) = 1.04 \pm 0.01$ . The uncertainty is estimated as the standard deviation of the mean,  $\delta = s/\sqrt{N}$ , where  $s$  is the population standard deviation and  $N$  is the population size.

The conclusion is that the perfect correlation of strength and stiffness effectively transforms the fracture criterion into a critical strain criterion, with some effects of elastic shielding. These effects produce weaker microcracking and crack diffuseness and lower toughness than either toughening effect of strength or stiffness variation alone.

The opposite case of independent strength and stiffness variation produces increased tortuosity, and higher toughness with much higher levels of redundant microcracking of the strength variability. The relative toughness is then  $K(\bar{\sigma} + d\sigma, \bar{k} + dk)/K(\bar{\sigma}, \bar{k}) = 1.34 \pm 0.01$ , which is an effect very close in magnitude to the expected effect. Qualitatively, the meanderings of the crack configurations appear similar between the two cases of correlated and uncorrelated variations, however with the latter showing a much higher level of redundant surrounding microcracking.<sup>2</sup> This is confirmed by a nearly equal crack profile height (r.m.s. height of 3.0 compared to 2.6 element dimensions for the uncorrelated and correlated cases respectively). The increased toughness for the uncorrelated material is due to two effects. The elements with high stiffness and low strength serve as potent microcracking sources, and those with low stiffness and high strength have a significantly higher energy absorbing capacity.

---

<sup>2</sup>This explains the shorter crack for the same number of breaks

### 3.3.3 *Realistic distribution of correlated strength and stiffness at the representative volume element level*

In the light of the abstract exercise of the effects of the correlated and uncorrelated strength and stiffness variations presented in Sections 3.3.1 and 3.3.2 above, a separate simulation was performed to obtain more realistic information on covariation of strength and stiffness. This was derived from explicit microstructural simulations of the properties of small volume elements as specific microstructure units. For this purpose a large ( $1000 \times 1000$  points) computer generated microstructure was sectioned into three families of increasing cell sizes: with  $10 \times 10$ ,  $20 \times 20$  and  $40 \times 40$  points. A very large number of such cells in each family of three sizes was then tested in tension as potential candidates for RVEs to determine their distributions of porosity, strength and stiffness. These distributions are shown in Fig. 15. The results of the  $10 \times 10$  point cells were taken as the preferred size of the RVEs since this came close to the extent over which unstable cracking cascades had been observed in connection with the first simulation discussed in Sections 3.1 and 3.2. In this manner the criterion of local fracture could be arranged to match the consequential material response.

Since the crack propagation resistance of various microstructures was governed directly by the local variability of strength and stiffness, and their covariation, the dependence of such variability on porosity was studied in  $10^4$  RVEs of  $10 \times 10$  size. This dependence is shown in Fig. 16 together with the specific direct correlation of the strengths and stiffness of these elements. The same information on variability of the strength and stiffness of these  $10^4$  RVEs in terms of their coefficients of variation is summarized in Table I. The correlation between the strength and stiffness values was measured here by the two variable correlation parameter  $\chi$  as follows:

$$\chi = \frac{[(\sigma(\vec{r}) - \bar{\sigma})(k(\vec{r}) - \bar{k})]}{s_{\sigma} s_k} \quad (9)$$

where  $\sigma$  and  $k$  represent the strength and stiffness of the RVEs,  $\vec{r}$  is the location of the element in the 2-D field from which the information was extracted and  $s_{\sigma}$  and  $s_k$  are the standard deviations of the respective distributions of strength and stiffness. The computed values of  $\chi$  were found to be in the range of 0.84 – 0.93 for these simulated microstructures. A value of 1.0 implies perfect covariation and 0 independent populations. The high value of  $\chi$  implies a tendency towards the critical strain criterion response with the resulting reduced toughness. In addition, the variability of strength

and stiffness are seen to be relatively insensitive to the details of the different microstructures that were generated in this study. The coefficients of variation of these RVEs are relatively large in comparison with those considered previously in Section 3.3.1. They range from 0.59 to 0.68 and from 0.56 to 0.77 for strength and stiffness respectively. The strongest dependence of variability was seen to be on the average porosity; as porosity increases, the variability increases for both strength and stiffness, as shown in Fig. 17. One reason for this is that higher porosity elements have a larger number of possible ways for this porosity to be distributed (high entropy), within the restrictions of the reaction kinetic simulation model which produced these microstructures. This result suggests that microstructures with a higher frequency of high porosity elements, e.g. high average porosity microstructures, have the potential for higher local variability and consequential increased crack tortuosity, and associated higher energy release rate.

In addition to the close correlation between local strength and stiffness, the connection between local stiffness and porosity on the scale of the RVEs indicates a small and relatively constant effect of the typical factors other than average porosity which govern elastic properties of porous solids such as pore size, shape and spatial distribution. This same result was obtained in Section 3.1 for larger microstructure elements, implying that over the range of scale from the interpore ligament to a scale 5-10 times larger, the simulated microstructures exhibit limited sensitivity of elastic modulus to pore shape and spatial distribution, and strong sensitivity to average porosity, as the single most important parameter.

The strength and local porosity are seen to be less correlated than stiffness and porosity (compare Fig. 16(a) and Fig. 16(b)). The previously mentioned factors for variability of stiffness associated with pore morphology, and their spatial distribution together with the increased variability generated by reduced grain boundary strength are the major contributors to overall variability of properties.

The effect of grain boundary strength is seen to be an important factor in the de-coupling of local strength and stiffness. This is a consequence of a decrease in the covariation parameter,  $\chi(\sigma, k)$ , from 0.951 to 0.854 produced by a reduction of grain boundary strength to 75% of full strength of matrix. The reduction of all grain boundary strengths in such a manner was noted to produce the high proportion of intergranular fractures in the tensile fracture simulation of large microstructures discussed in Section 3.1. This effect also serves to de-couple the local strength from local porosity as evidenced by the decrease of another covariation parameter  $\chi(\sigma, p)$ , from 0.800 to

0.680. The fact that the average local strength is reduced from 0.287 to 0.267, but the resulting toughness measured explicitly by propagating a crack through a microstructure remains relatively unaffected, demonstrates the effectiveness of the variability of the local strength.

#### *3.3.4 Crack propagation with correlated specific local strength and stiffness using the 2-D super elements*

To evaluate the effects of specific correlations of strength and stiffness at the local RVE level on crack propagation resistance, and to incorporate a measure of three dimensionality to the microscale crack propagation, a final simulation was performed utilizing the 2-D super element with effective 3-D properties as described in Section 2.5 above. The specific correlations of strength and stiffness of the  $10 \times 10$  point cell RVEs discussed in Section 3.3.3 above were incorporated into the properties of the "bonds" in a random manner. Figure 18a shows the effective strength and stiffness distributions of the 2-D super cells based on the  $10 \times 10$  point cell RVEs, averaged 3 at a time, in the manner described in Section 2.5. Clearly, this type of third dimension effect has removed elements of zero strength and zero stiffness, compared to the distributions of the constituent 2-D elements shown in the upper row of Fig. 15. This has resulted in an elevation of the average normalized strength to 0.488 and the average normalized stiffness to 0.365, with reductions in corresponding coefficients of variation of strength and stiffness to 0.42 and 0.385 respectively, from the values given in Table I. Figures 18b and 18c show the resulting fracture toughness sampled by the growing crack and the tortuosity of the crack plane. While the crack plane exhibits significant roughness and some bridging behavior there is minimum redundant microcracking in the vicinity of the crack plane. The fracture toughness normalized with that of the homogeneous equivalent control microstructure (described in Section 3.2) is now  $1.15 \pm 0.02$ , indicating a modest effect on toughness, compared to the maximum possible cooperative toughening of  $K_{\max}(\bar{\sigma} + d\sigma; \bar{k} + dk)/K(\bar{\sigma}; \bar{k}) = (1.34 \times 1.26) = 1.69$ .

In summary, the major result of the simulation of crack propagation through microstructures with element properties obtained by sampling RVE scale sections of simulated microstructures is that the measured toughness is relatively unaffected by variables associated with pore size and shape distributions, but most strongly determined by the average porosity. The simulated fracture paths were of a similar planar character with minimal microcracking and some limited bridging ligaments. The limits of pore size and spatial distribution imposed by the reaction kinetics model

used to generate these microstructures serve to place bounds on the strength and stiffness variations available for optimal microstructure design. One case for which some insight can be derived is the high porosity microstructure with associated relatively higher strength and stiffness variability. This case demonstrates the competition between the increase in toughness due to higher variability in strength and stiffness against the reduction in toughness due to the relatively strong dependence of the elastic properties on average porosity.

## 4 DISCUSSION AND CONCLUSIONS

We have demonstrated a connection between pertinent microstructural features and crack propagation resistance of porous heterogeneous materials by simulating the fracture process in computer generated microstructures. Such models demonstrate that by associating the development of microstructural features and the heterogeneities in local stiffness and strength with processing parameters, followed by probing the fracture response of such microstructures, the gap can be bridged between processing and mechanical properties. This is especially relevant for fracture toughness which is particularly sensitive to microstructural heterogeneities. For example; the variability in local strength and stiffness affects the fracture toughness more strongly than average physical properties such as the elastic modulus.

The two dimensional fracture simulations for representative microstructures with a range of 20-30% porosity exhibit a stable ligament microcracking behavior which results in the evolution of sub-critical damage leading to an eventual fracture instability. In the tensile simulation under displacement control no instability develops, but rather characteristic stress-strain curves with long tails of decreasing stress are obtained for material degeneration on continued extension. The tensile toughness values can be significantly altered in comparison with those of a perfect homogeneous material. This tensile toughness  $w = \int \sigma d\epsilon \sim 0.15(\sigma_c \epsilon_c / 2)$ , where the subscript  $c$  indicates critical stress and strain values of a reference perfect material. In fact an otherwise perfect solid with a stress amplifying defect will have less energy absorbing capacity than the porous microstructures analyzed here if the stress concentration due to the defect is more than approximately 3.

The frequency and effectiveness of beneficial microcracking are strongly determined by the blunting ability of the surrounding pores in the porous microstructure. For three-dimensional microstructure, the possibility exists for crack growth in the third dimension, and the blunting effect may be diminished. A fully three dimensional treatment of crack interaction with porosity is needed to fully evaluate this effect. An attempt in the introduction of a 2-D super element with some aspects of the variability of the material in the third dimension has provided some interesting trends and important insight indicating the mutually beneficial interaction of strong and weak segments along a crack front.

Variability of elastic stiffness and fracture properties on the scale of pore clusters give rise to increasing crack tortuosity, microcracking, bridging and associated R-curve behavior. When



varied independently, the local stiffness and strength each produce maximum relative toughness increases of 34 and 31% respectively. Independent assignment of strength and stiffness (correlation of 0) to local material elements produces a tougher structure in comparison with proportional variation of strength and stiffness (correlation of 1). This latter distribution of element properties effectively corresponds to a critical strain fracture criterion and a toughening effect significantly less than either of the two toughening effects, determined independently. Effects such as reduced grain boundary strength (at constant bond stiffness) tend to decouple the correlation of strength and stiffness of representative volume elements and results in increased toughening in reference to a homogeneous microstructure. Sampling the properties of large size simulated microstructures revealed a correlation between the microstructural element strength and stiffness of 0.84-0.93, between the two extremes of 0 and 1, but closer to the less potent toughening of the critical strain criterion behavior. This strong correlation is a direct consequence of the porous microstructure where pores reduce both strength and stiffness. In other situations where no such geometrical connection exists, less correlation between local strength and stiffness should be attainable which, with increasing variability, has significant toughening effects, as is well known in composites [15].

The question of microstructural design to coax the crack into bridging, crack trapping and blunting configurations is key in order to improve the toughness. We have shown the potency of the fracture of isolated ligaments to increase energy absorption in a representative microstructure of a relatively high porosity brittle medium and quantified the role of local material variability in terms of crack plane roughness derived by effects such as microcracking, crack deflection and bridging for an advancing crack. It is clear that crack bridging is one of the more effective mechanisms, which is predominant in highly heterogeneous structures in which the crack tip stress singularity is still high. This is the mechanism actually observed in associated experimental studies of the fracture of porous RBSN [16].

**Acknowledgement:**

This research has been supported by the AFOSR under Grant AFOSR-91-0263C. For this support we are grateful to Drs. G. Haritos and W. Jones. We gratefully acknowledge many useful discussions with Dr. J. Haggerty of the Materials Processing Center of M.I.T., who has been a direct collaborator in the experimental phase of this research program, and useful correspondence with Professor D. Srolovitz of the University of Michigan, on the method of simulation.

**Table I Strength and Stiffness Variabilities of RVEs of  $10 \times 10$  Size**

Simulation Description	strength $\sigma/\sigma_0$	stiffness $k/k_0$	porosity p	$c(\sigma)$	$c(k)$	Correlation			K/K <sub>0</sub>
						$\sigma - k$	$\sigma - p$	$k - p$	
Control	0.27	0.32	0.25	0.61	0.68	0.85	-0.68	-0.84	0.65
(1)	0.23	0.32	0.25	0.64	0.66	0.93	-0.77	-0.84	0.50
(2)	0.21	0.24	0.31	0.68	0.75	0.81	-0.60	-0.81	0.67
(3)	0.32	0.43	0.19	0.60	0.56	0.93	-0.79	-0.87	0.82
(4)	0.22	0.30	0.25	0.59	0.63	0.93	-0.75	-0.81	0.57
(5)	0.25	0.29	0.28	0.66	0.77	0.84	-0.65	-0.83	0.65
(6)	0.26	0.32	0.24	0.62	0.68	0.85	-0.67	-0.85	0.65
Control (no grain boundaries)	0.29	0.32	0.25	0.64	0.68	0.95	-0.80	-0.84	0.63

## REFERENCES

- [1] R.W. Rice, *J. Mater. Sci.* , **20**, (1985), 1392.
- [2] L.J. Gibson and M.F. Ashby "Cellular Solids, Structure and Properties" Pergamon Press, New York (1988).
- [3] R.W. Rice, in "Treatise on Materials Science and Technology", edited by R.K. MacCrone, Academic Press, N.Y. , **Vol. 2**, p. 199, (1977).
- [4] F.G. Haubensak, V.V. Bulatov and A.S. Argon, *Computer-Aided Material Design*, in this issue.
- [5] J.G. Kirkwood, *J. Chem. Phys.*, **7**, (1939), 506.
- [6] P.N. Keating, *Phys. Rev.*, **152**, (1966), 774.
- [7] H.Y. Wang, R. Najafabadi, D.J. Srolovitz and R. Lesar, *Met. Trans. A*, **23**, (1992), 3105.
- [8] F.A. McClintock and A.S. Argon in "Mechanical Behavior of Materials", Chapter 3, Addison-Wesley, Reading, MA (1966).
- [9] W.H. Press, S.A. Teukolsky, W.T. Vetterling and B.P. Flannery, "Numerical Recipes in C", Cambridge University Press, Cambridge, p. 413 (1992).
- [10] M. Born and K. Huang "Dynamical Theory of Crystal Lattices," Clarendon Press, Oxford, (1966).
- [11] A. Lightfoot, J. Sigalovsky, and J.S. Haggerty, *J. Am. Ceram. Soc.*, submitted for publication.
- [12] L.R.F. Rose, *Mechanics of Materials*, **6**, (1987), 11.

- [13] A.F. Bower and M. Ortiz, *J. Mech. Phys. of Solids*, **38**, (1990), 443.
- [14] C. Wu, S.W. Freiman, R.W. Rice and J.J. Mecholsky, *J. Mater. Sci.*, **13**, (1978), 2659.
- [15] A.S. Argon in "Composite Materials: Fracture and Fatigue", edited by L.J. Broutman. Academic Press: New York, **vol. 5** p. 153, (1974).
- [16] F.G. Haubensak, A. Lightfoot, A.S. Argon and J.S. Haggerty, *J. Mater. Sci.*, submitted for publication.
- [17] J.F. Lutsko, *J. Appl. Phys.*, **65**, (1988), 2991.

## APPENDIX. THE SPRING NETWORK MODEL COMPARED WITH THE FINITE ELEMENT METHOD IN THE SOLUTION OF LINEAR PLANAR ELASTICITY PROBLEMS

In order to examine the capabilities of the spring network model to adequately account for non-uniform stress distributions we present here a comparison between the stress field solution with the spring network model against a corresponding solution obtained with the finite elements method. Since the focus in the present study is on porous solids, an infinite two-dimensional periodic array of circular pores is chosen as the test case.

For the sake of comparison and in order to calculate the stress distributions a local stress tensor is introduced either on the basis of a network *node* or a network *bond* in the spring network model. For that the usual definition [10] is used for the stress tensor expressed in terms of the "on-site" forces  $\mathbf{f}_i$  as follows:

$$\Omega \boldsymbol{\sigma} = \frac{1}{2} \sum_i (\mathbf{f}_i \otimes \mathbf{r}_i + \mathbf{r}_i \otimes \mathbf{f}_i), \quad (\text{A.1})$$

where  $\boldsymbol{\sigma}$  is the stress tensor,  $\Omega$  is the total volume of the body,  $\mathbf{r}_i$  is the position vector of site  $i$ , and the summation is performed over all sites within the body, where the factor  $1/2$  compensates for the pair-wise double counting.

As was demonstrated by Lutsko [17], equation (A.1) should be modified for the case of periodic boundary conditions and general non-central forces, as:

$$\Omega \boldsymbol{\sigma} = \frac{1}{2} \sum_i \left( \frac{\partial}{\partial \mathbf{r}_{ij}} \otimes \mathbf{r}_{ij} + \mathbf{r}_{ij} \otimes \frac{\partial}{\partial \mathbf{r}_{ij}} \right) \Phi, \quad (\text{A.2})$$

where  $\Phi$  is the potential energy expressed as a function of the site coordinates and  $\mathbf{r}_{ij} = \mathbf{r}_i - \mathbf{r}_j$ . By substituting equation (A.1) for  $\Phi$  into equation (A.2), one obtains for the spring network model the following expression:

$$\Omega \boldsymbol{\sigma} = \frac{1}{2} \sum_i \sum_{j(i)} \left( \hat{\mathbf{t}}_{ij} + \sum_{k(i,j)} \hat{\mathbf{t}}_{ijk} \right), \quad (\text{A.3})$$

where tensors  $\hat{\mathbf{t}}_{ij}$  and  $\hat{\mathbf{t}}_{ijk}$  are defined as <sup>3</sup>

---

<sup>3</sup>All other quantities in equations (A.4) and (A.5) were defined in Section 2.1.

$$\hat{\mathbf{t}}_{ij} = k_{ij}(r_{ij} - a_0)\mathbf{u}_{ij} \otimes \mathbf{u}_{ij} \quad (\text{A.4})$$

$$\hat{\mathbf{t}}_{ijk} = c_{ijk}(\mathbf{u}_{ij} \cdot \mathbf{u}_{ik} - b_0)\{[\mathbf{u}_{ik} - (\mathbf{u}_{ijk} \cdot \mathbf{u}_{ik})\mathbf{u}_{ij}] \otimes \mathbf{u}_{ij} + \mathbf{u}_{ij} \otimes [\mathbf{u}_{ik} - (\mathbf{u}_{ij} \cdot \mathbf{u}_{ik})\mathbf{u}_{ij}]\}/r_{ij}. \quad (\text{A.5})$$

In equation (A.3) summation is performed over all sites  $i$  of the triangular spring network, their six nearest neighbor sites  $j(i)$ , and two common nearest neighbor sites  $k(i, j)$  of sites  $i$  and  $j$ , respectively.

In order to examine the stress distribution inside the body it is necessary to partition the total stress (equation A.3) among the sites (or the bonds) requiring that the volume average of local stresses be equal to the total stress:

$$\Omega \boldsymbol{\sigma} = \sum_{\text{sites}} \omega_i^{\text{site}} \cdot \boldsymbol{\sigma}_i^{\text{site}} \sum_{\text{bonds}} \omega_{ij}^{\text{bond}} \cdot \boldsymbol{\sigma}_{ij}^{\text{bond}} \quad (\text{A.6})$$

The per-site volume  $\omega_i^{\text{site}}$  is defined as the area of the hexagon surrounding each site. Accordingly, the “per-bond” volume  $\omega_{ij}^{\text{bond}}$  is defined as the bond share of the “per-site” volume, i.e.,  $\omega_{ij}^{\text{bond}} = \omega_i^{\text{site}}/3$ . It is natural, then, to define the “per-site” stress as

$$\boldsymbol{\sigma}_i^{\text{site}} = \frac{1}{2\omega_i^{\text{site}}} \sum_{j(i)} \left( \hat{\mathbf{t}}_{ij} + \sum_{k(i,j)} \hat{\mathbf{t}}_{ijk} \right), \quad (\text{A.7})$$

and the per-bond stress as

$$\boldsymbol{\sigma}_{ij}^{\text{bond}} = \frac{1}{2\omega_{ij}^{\text{bond}}} \left( \hat{\mathbf{t}}_{ij} + \frac{1}{2} \sum_{k(i,j)} (\hat{\mathbf{t}}_{ijk} + \hat{\mathbf{t}}_{ikj}) \right), \quad (\text{A.8})$$

so that by performing summations in (A.6) the average stress (equation A.3) is obtained.

Local stress computed according to equation (A.8) was compared against the corresponding finite elements solution for the hexagonal periodic array of circular pores subjected to uniaxial load (Fig. 19). Small differences in the  $\sigma_{11}$  component (perpendicular to the loading axis) seen near the pore surfaces are due to the discreteness of the spring network. Other than that, the agreement is almost complete.

## Figure Captions

- Fig. 1      A typical microstructure of reaction bonded silicon nitride (RBSN), showing the propagation of a crack through the microstructure.
- Fig. 2      A 3 node point configuration of the extension springs and angle flexing "watch springs" in the mesh.
- Fig. 3      Method of determination of the strength and stiffness properties of 2-D super elements by line averaging the properties of 3 adjacent representative volume elements from a typical field of simulated porous microstructure, as explained in the text.
- Fig. 4      A comparison between the stress intensity based upon the weighted line average of the energy release rate,  $g$ , and the more accurate solution from Bower and Ortiz, [13], for crack trapping. Top frame depicts five critical crack front shapes penetrating into a low toughness region between two high toughness regions for the five specific ratios of critical fracture toughnesses of the low and high toughness regions. The lower frame shows the important effect of crack front support by the tough regions for the five special solutions of toughness ratio of the low to the high toughness. In the range of ratios from 0.4 to 1.0 the effective toughness is well described by the simple mean value.
- Fig. 5      Fracture response of a uniaxially stressed microstructure volume element of RBSN. The unstable fracture cascade events shown in the stress-strain curve are associated with the sites where such fracture cascades occur in the top figure of the computer generated microstructure.
- Fig. 6      The monotonic decline of the normalized Young's modulus of the stressed microstructure of Fig. 5 with increasing damage accumulation. Note the drops associated with pore linkage and subsequent nucleation of a microcrack elsewhere.



- Fig. 7      The microstructures and uniaxial stress-strain responses, to fracture, of a series of 7 specific cases: (a) a control sample of 25% porosity; (b) a case of high initial  $Si_3N_4$  nucleus density; (c) a high porosity microstructure with 31% porosity; (d) a low porosity microstructure with 19% porosity; (e) a microstructure with anisotropic grain growth; (f) a case with negligible product/reactant impingement; (g) a case with 4% by volume of smaller  $Si$  particles in the green material population.
- Fig. 8a      Dependence of the normalized Young's moduli on porosity of the 7 simulations presented in Fig. 7. The key to the identification of the information is as follows: (c) control microstructure, Fig. 7a; (1) is Fig. 7b; (2) is Fig. 7c; (3) is Fig. 7d; (4) is Fig. 7e; (5) is Fig. 7f; (6) is Fig. 7g.
- Fig. 8b      Dependence of the normalized maximum tensile strengths on porosity of the 7 simulations presented in Fig. 7. The key to the identification numbers is given in the caption of Fig. 8a.
- Fig. 8c      Dependence of the normalized tensile toughness on porosity of the 7 simulations presented in Fig. 7. The key to the identification numbers is given in the caption of Fig. 8a.
- Fig. 9      Crack propagation experiments through fully dense material with variability in bond strength but constant maximum stiffness. The coefficients of variation in strength  $c(\sigma)$  increase from a to f. Initial positions of the pre-cracks are marked by short vertical lines.
- Fig. 10      Crack propagation experiments through fully dense material with variability in bond stiffness but constant maximum strength. The coefficients of variation in stiffness  $c(k)$  increase from a to e.

- Fig. 11a      Summary of results of simulations presented in Fig. 9 giving the dependence of average fracture toughness on the coefficients of variation of bond strength.
- Fig. 11b      Summary of results of simulations presented in Fig. 10, giving the dependence of average fracture toughness on the coefficient of variation of bond stiffness.
- Fig. 12      R-curve behavior of a structure with a high coefficient of variation in strength of  $c(\sigma_c) = 0.52$ .
- Fig. 13      The correlation between rms crack profile height and the relative toughness indicates crack deviation from planar morphology relates to measured toughness due to such effects as crack deflection and microcracking.
- Fig. 14      The effect of perfect correlation between bond stiffness and strength on fracture toughness, for a coefficient of variation of 0.346, in both strength and stiffness, compared with a case in which variability in strength and stiffness is uncorrelated.
- Fig. 15      Strength, stiffness and porosity distributions obtained by probing potential representative volume elements of a large simulated microstructure which spans 10,000 volume elements. Upper row for elements of 10 mesh points on the side, middle and lower rows for elements 20 and 40 mesh points on the side, respectively.
- Fig. 16      Spread of normalized stiffness (a) and, strength (b) with porosity in  $10^4$  VEs of 10 mesh points on the side, tested to sample realistic distributions. Correlation of normalized strength with normalized stiffness (c).

- Fig. 17      Dependences of the coefficients of variation in strength and stiffness on porosity for the simulations presented in Fig. 16.
- Fig. 18      Effective three dimensional strength and stiffness distributions embodied in the 2-D super element: (a) frequency distributions; (b) evolution of crack propagation resistance; (c) crack plane tortuosity.
- Fig. 19      Stress field solution comparison between a finite element generated solution and the discrete spring network model for an infinite hexagonal array of pores with spacing to diameter ratio of 4 under uniaxial strain. Loading direction ( $x_1$ ) is vertical. Heavy black lines represent the continuum FEM solution, shading and thin lines represent discrete spring stress solution.

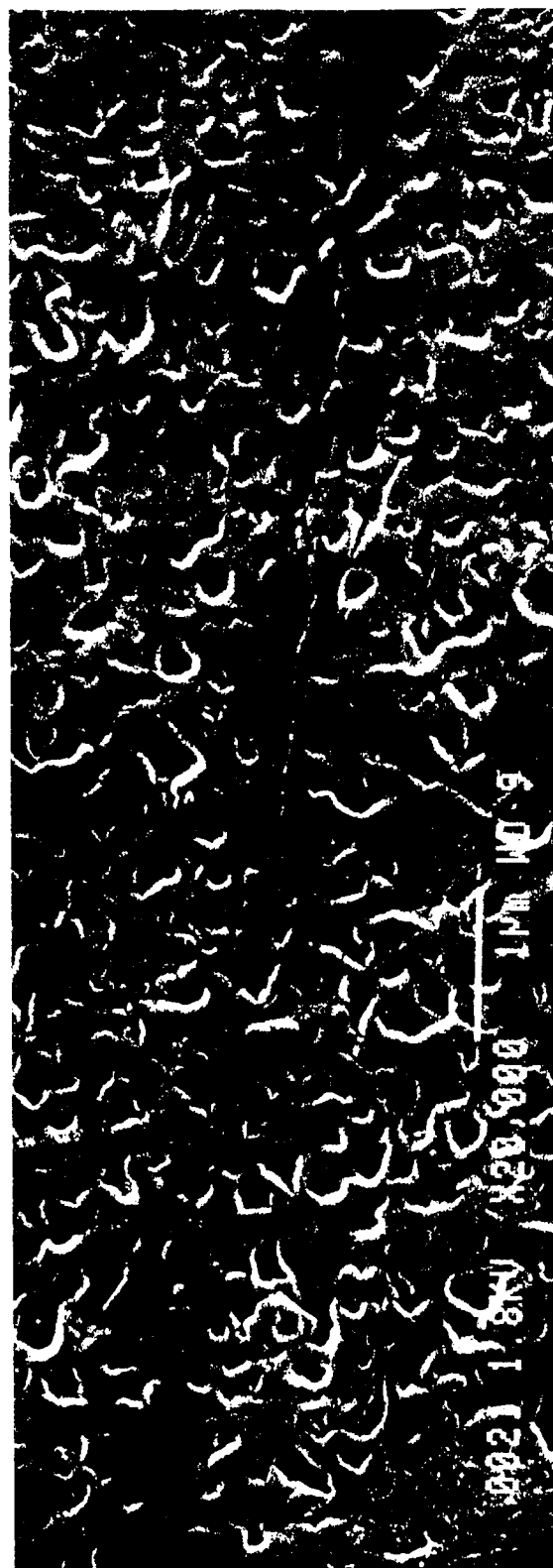


Fig. 1 A typical microstructure of reaction bonded silicon nitride (RBSN), showing the propagation of a crack through the microstructure.

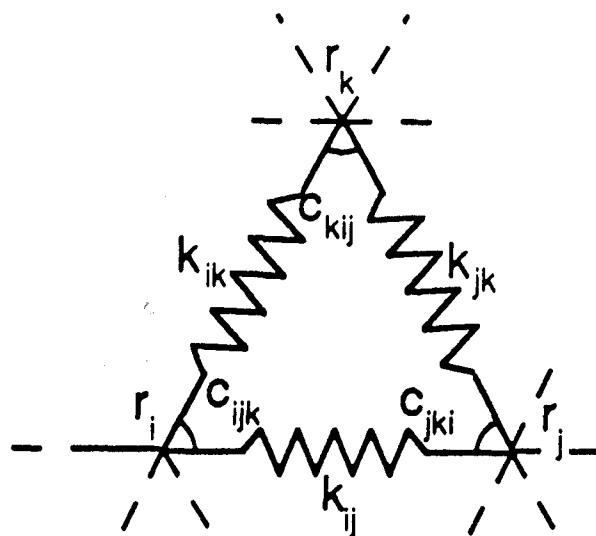


Fig. 2

A 3 node point configuration of the extension springs and angle flexing "watch springs" in the mesh.

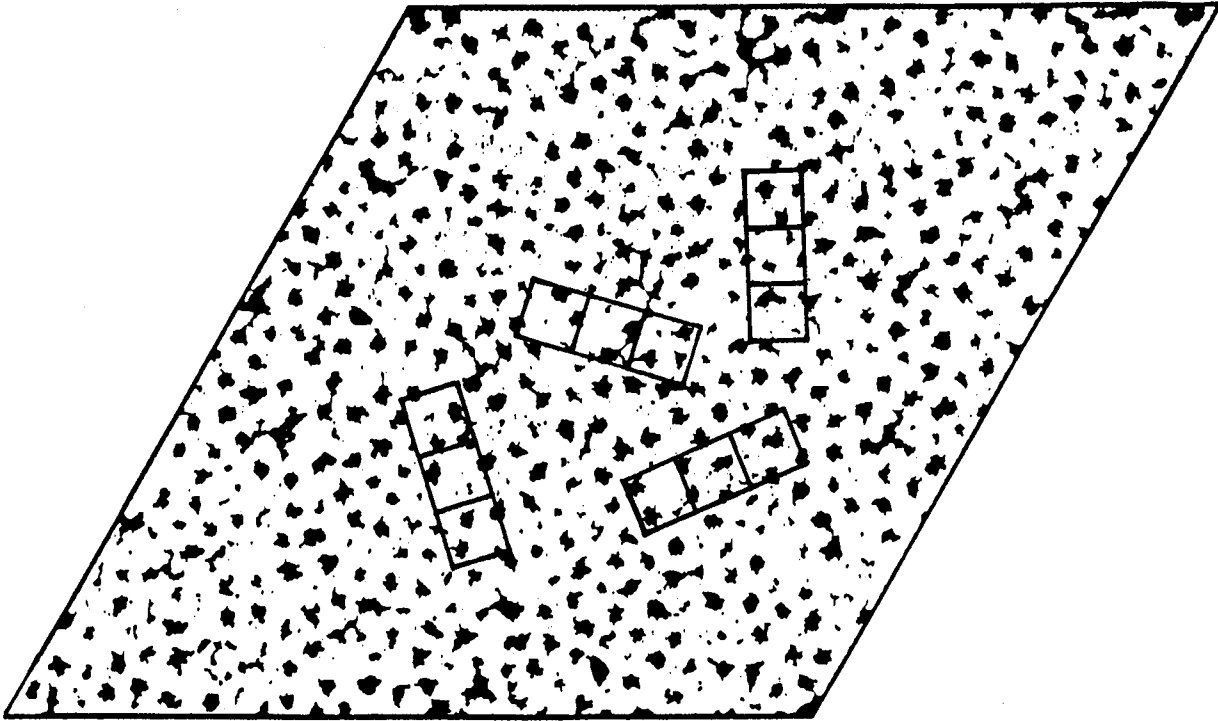


Fig. 3 Method of determination of the strength and stiffness properties of 2-D super elements by line averaging the properties of 3 adjacent representative volume elements from a typical field of simulated porous microstructure, as explained in the text.

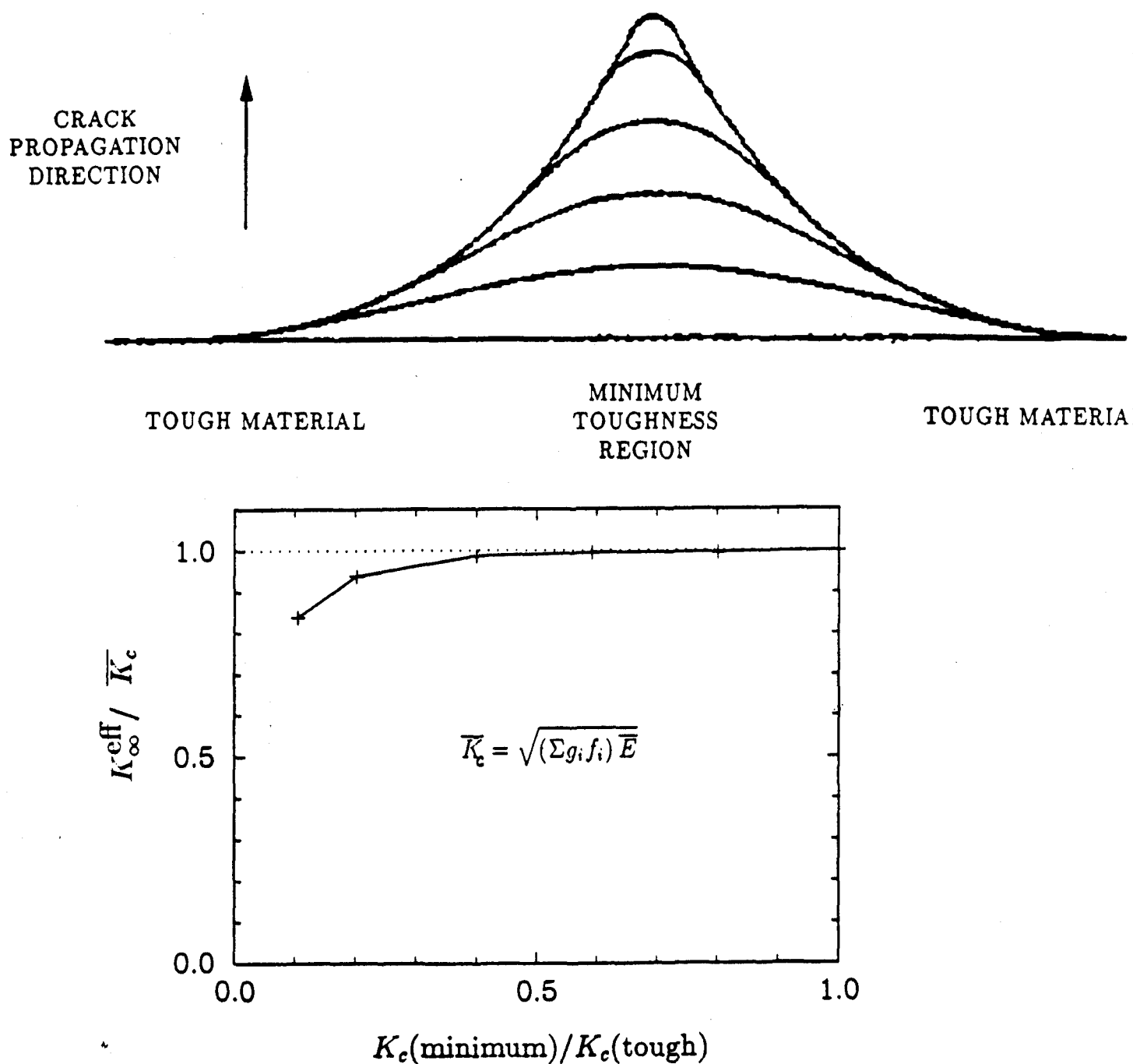


Fig. 4

A comparison between the stress intensity based upon the weighted line average of the energy release rate,  $g$ , and the more accurate solution from Bower and Ortiz, [13], for crack trapping. Top frame depicts five critical crack front shapes penetrating into a low toughness region between two high toughness regions for the five specific ratios of critical fracture toughnesses of the low and high toughness regions. The lower frame shows the important effect of crack front support by the tough regions for the five special solutions of toughness ratio of the low to the high toughness. In the range of ratios from 0.4 to 1.0 the effective toughness is well described by the simple mean value.

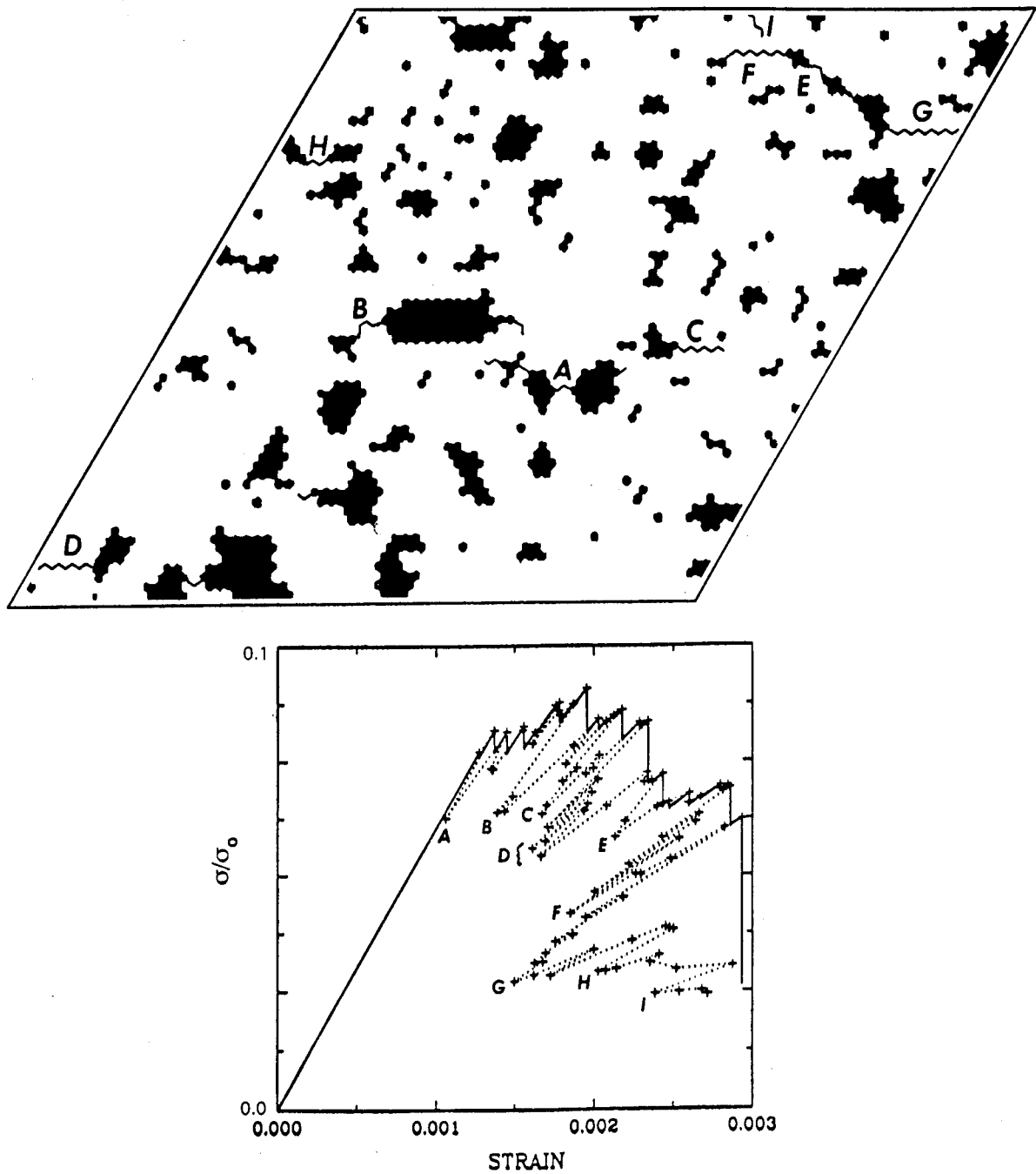


Fig. 5

Fracture response of a uniaxially stressed microstructure volume element of RBSN. The unstable fracture cascade events shown in the stress-strain curve are associated with the sites where such fracture cascades occur in the top figure of the computer generated microstructure.



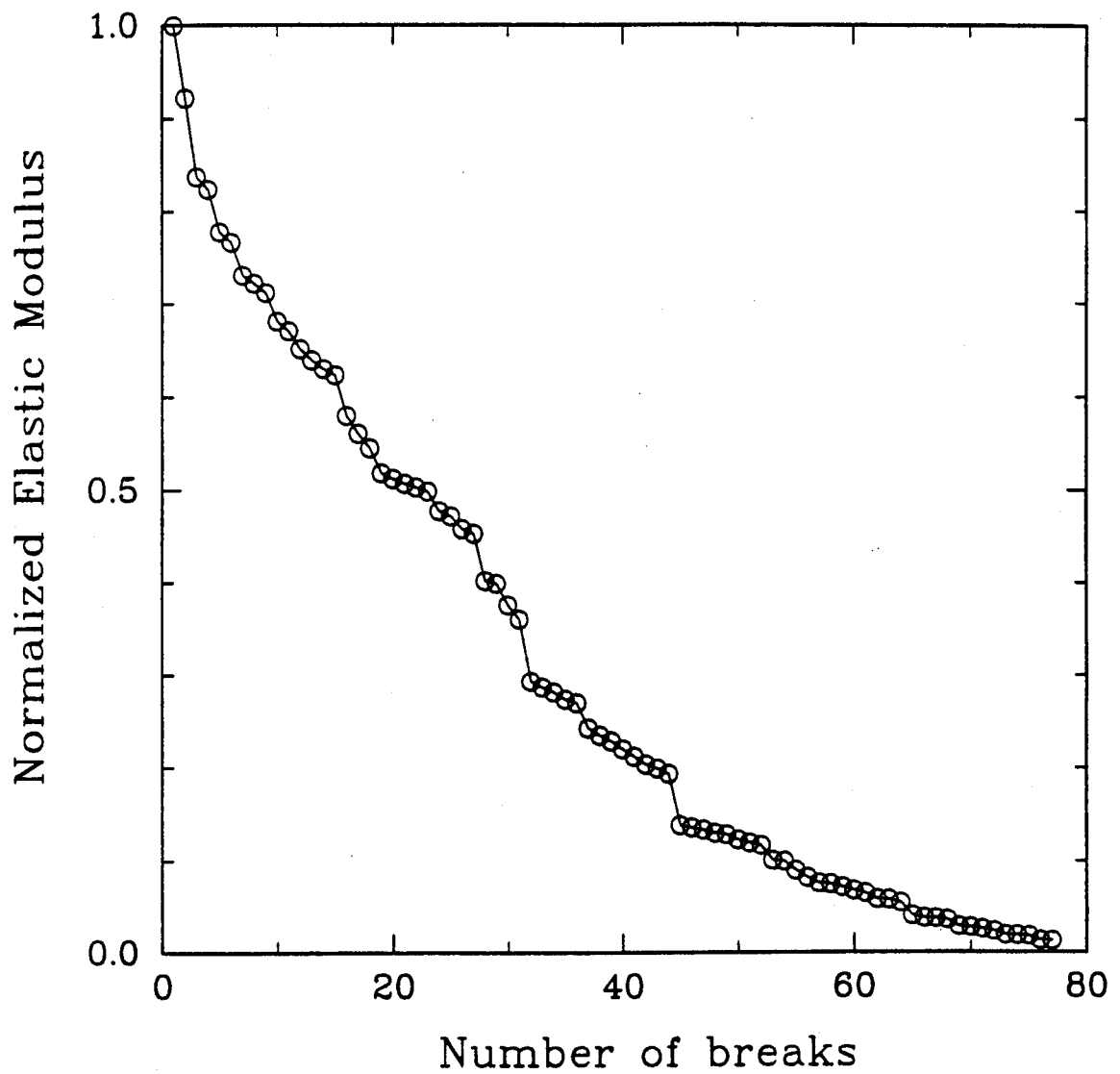


Fig. 6

The monotonic decline of the normalized Young's modulus of the stressed microstructure of Fig. 5 with increasing damage accumulation. Note the drops associated with pore linkage and subsequent nucleation of a microcrack elsewhere.

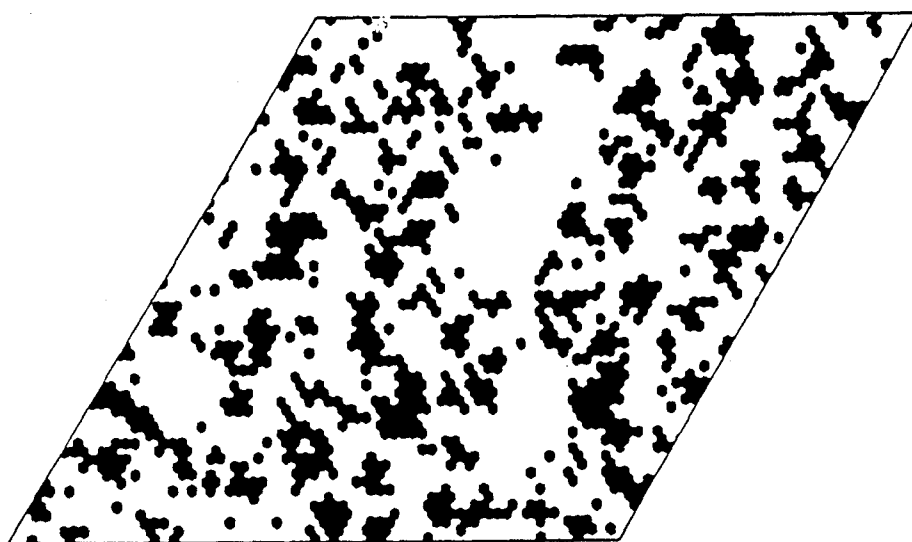
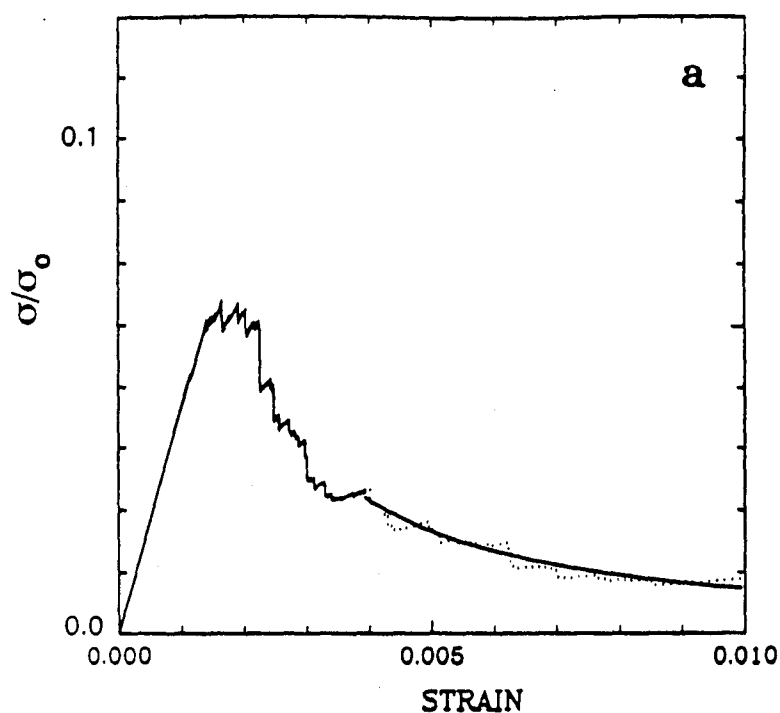
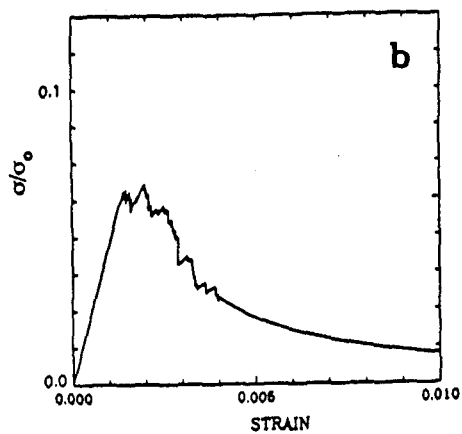


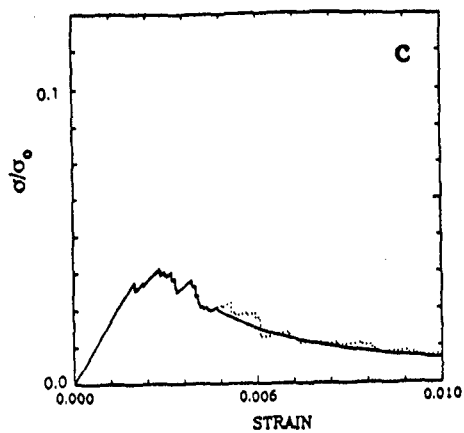
Fig. 7

The microstructures and uniaxial stress-strain responses, to fracture, of a series of 7 specific cases: (a) a control sample of 25% porosity; (b) a case of high initial  $Si_3N_4$  nucleus density; (c) a high porosity microstructure with 31% porosity; (d) a low porosity microstructure with 19% porosity; (e) a microstructure with anisotropic grain growth; (f) a case with negligible product/reactant impingement; (g) a case with 4% by volume of smaller  $Si$  particles in the green material population.

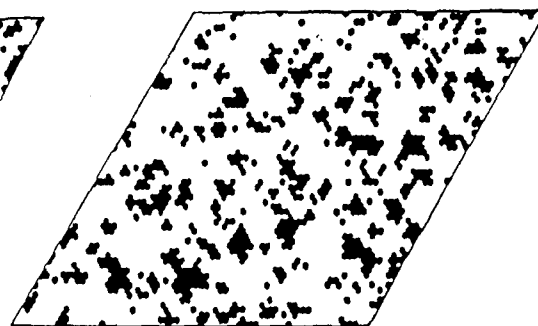
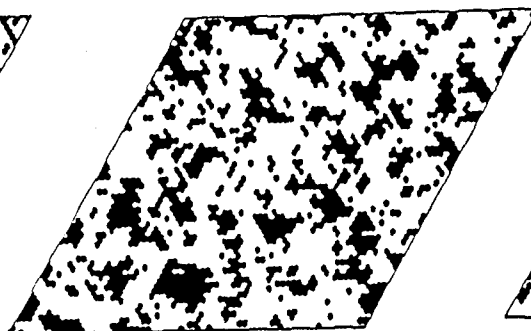
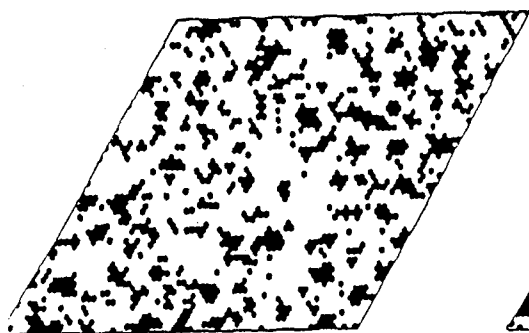
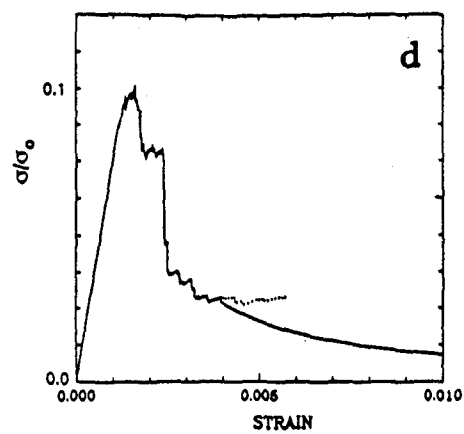
High Silicon Nitride Nuclei Density



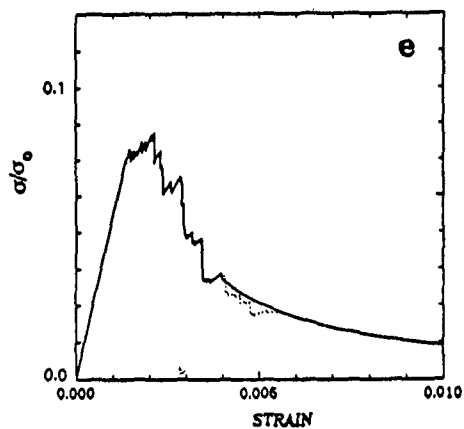
High Porosity



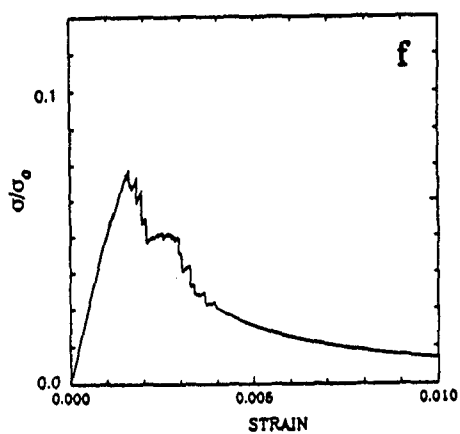
Low Porosity



Anisotropic grains



No product / reactant impingement



4 wt% Smaller Si Particle Population

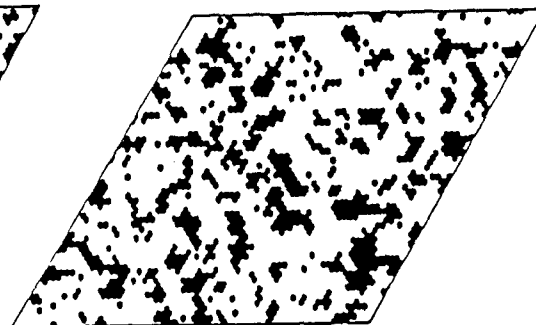
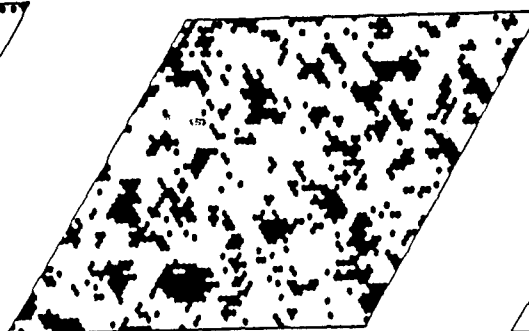
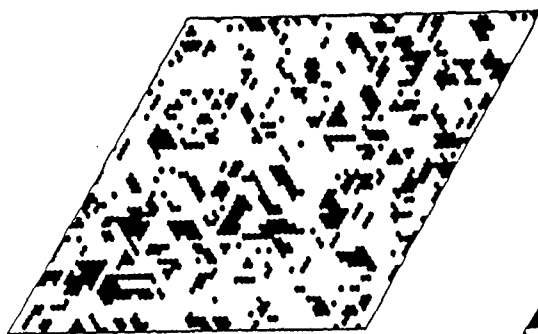
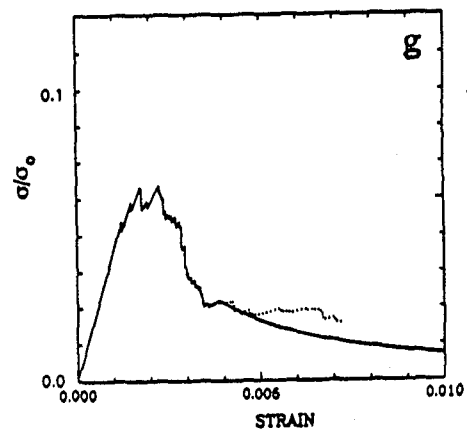


Figure 7 (b)-(g)

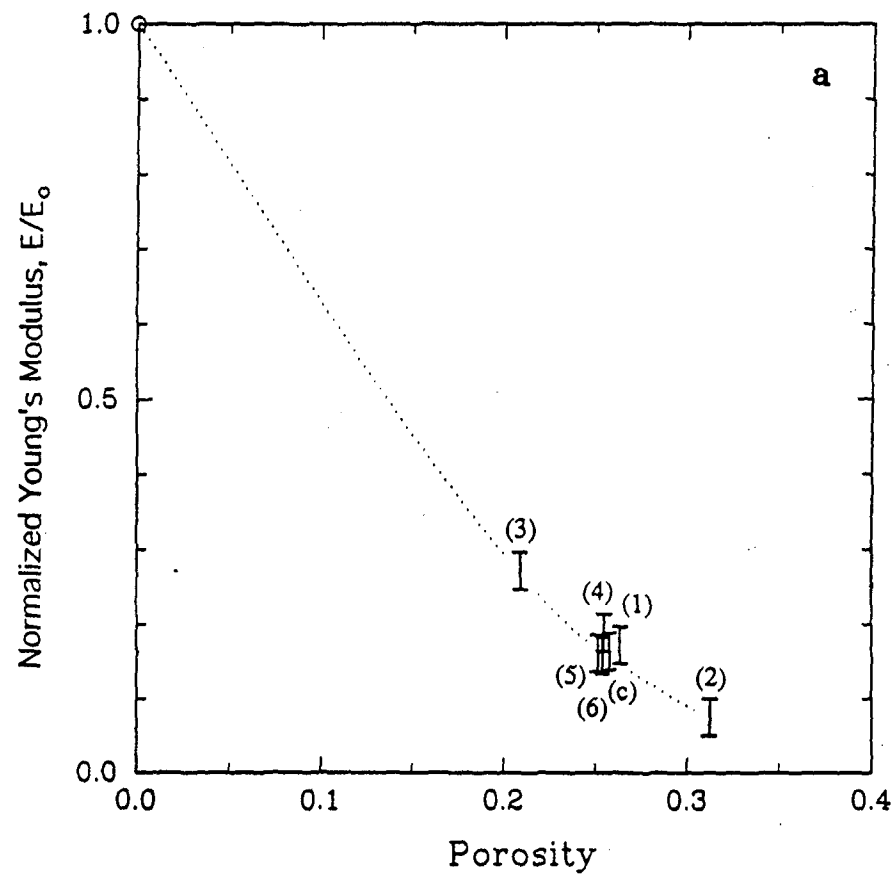


Fig. 8a

Dependence of the normalized Young's moduli on porosity of the 7 simulations presented in Fig. 7. The key to the identification of the information is as follows: (c) control microstructure, Fig. 7a; (1) is Fig. 7b; (2) is Fig. 7c; (3) is Fig. 7d; (4) is Fig. 7e; (5) is Fig. 7f; (6) is Fig. 7g.

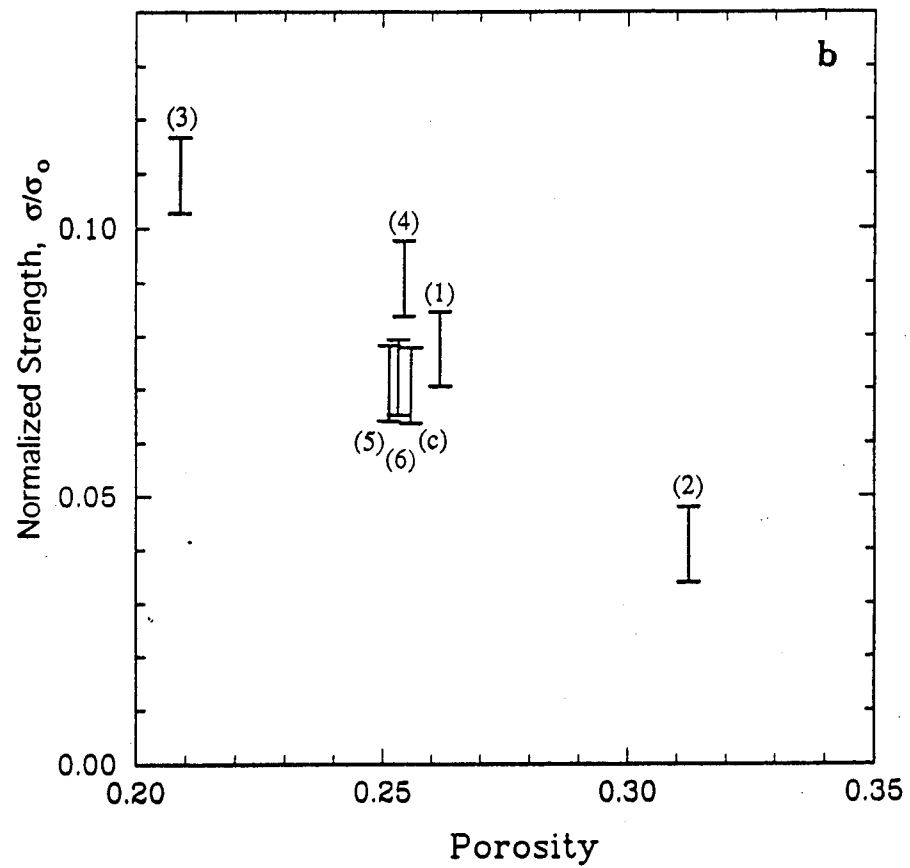


Fig. 8b

Dependence of the normalized maximum tensile strengths on porosity of the 7 simulations presented in Fig. 7. The key to the identification numbers is given in the caption of Fig. 8a.

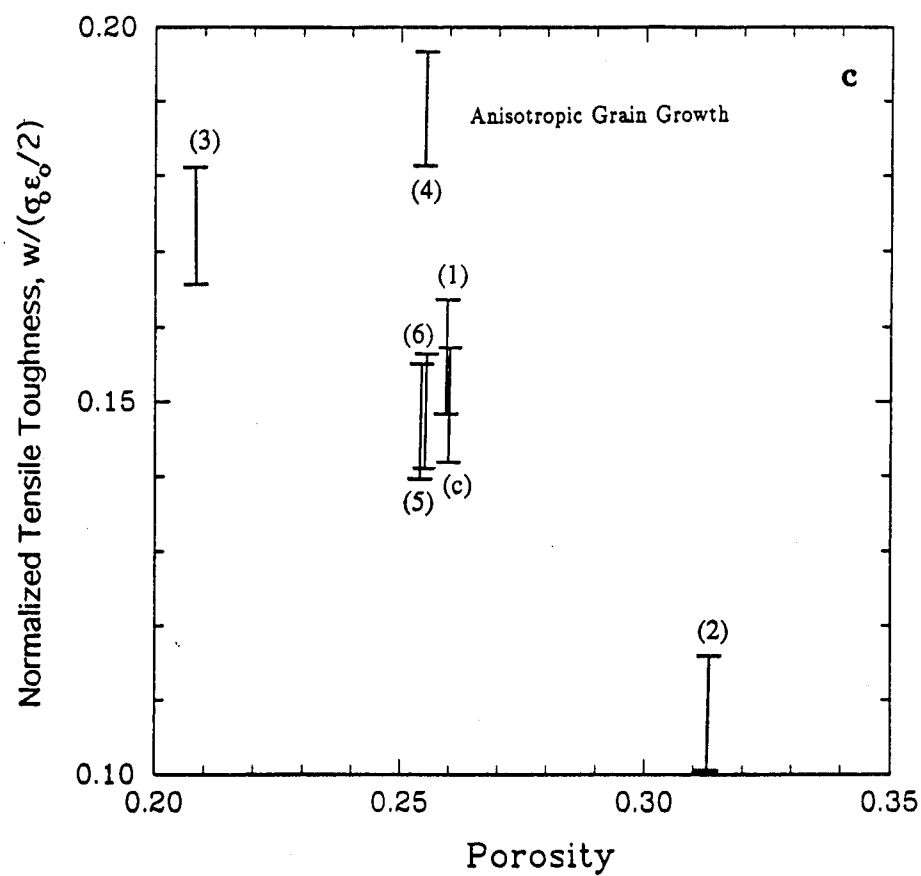


Fig. 8c

Dependence of the normalized tensile toughness on porosity of the 7 simulations presented in Fig. 7. The key to the identification numbers is given in the caption of Fig. 8a.

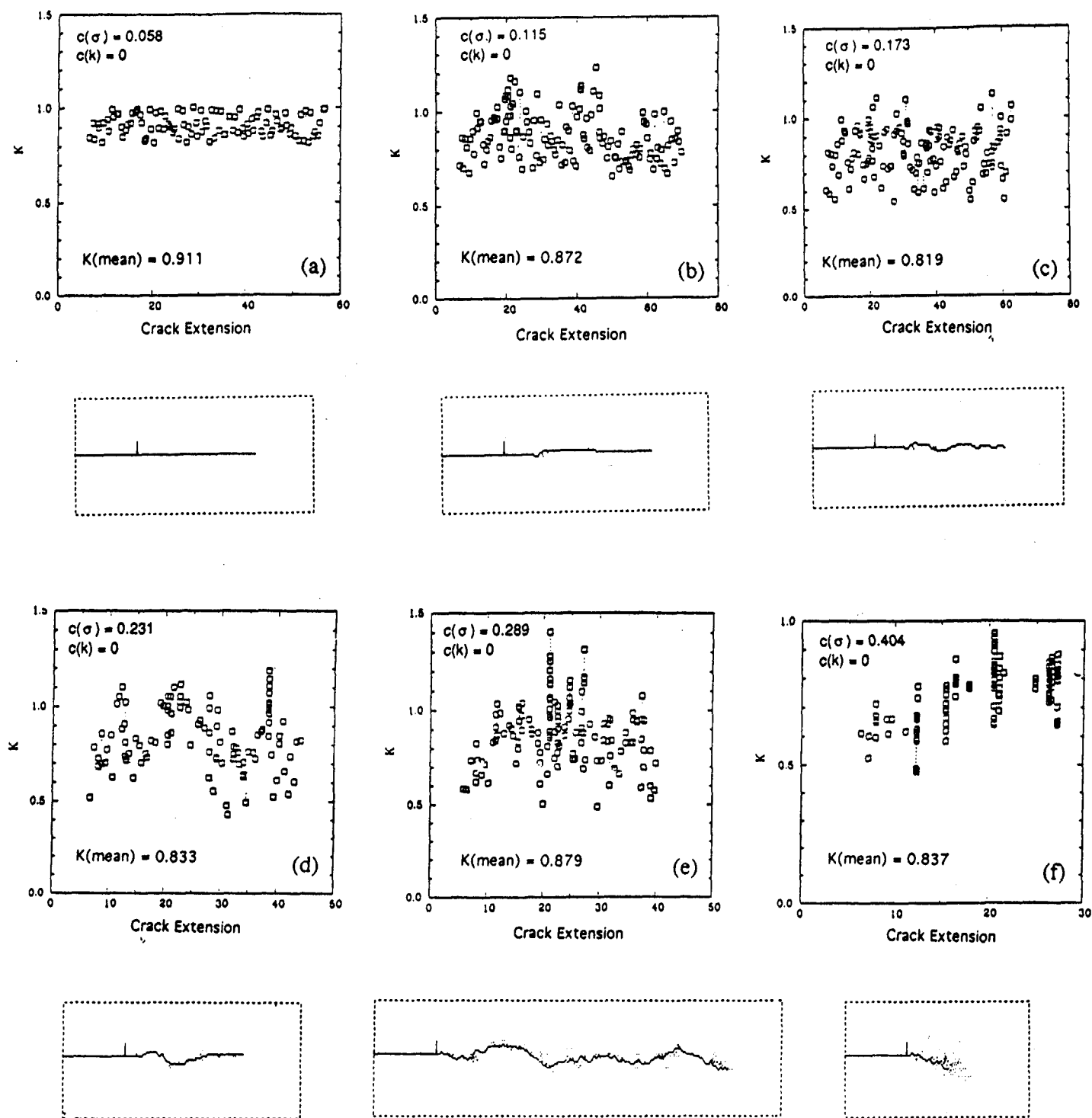


Fig. 9

Crack propagation experiments through fully dense material with variability in bond strength but constant maximum stiffness. The coefficients of variation in strength  $c(\sigma)$  increase from a to f. Initial positions of the pre-cracks are marked by short vertical lines.

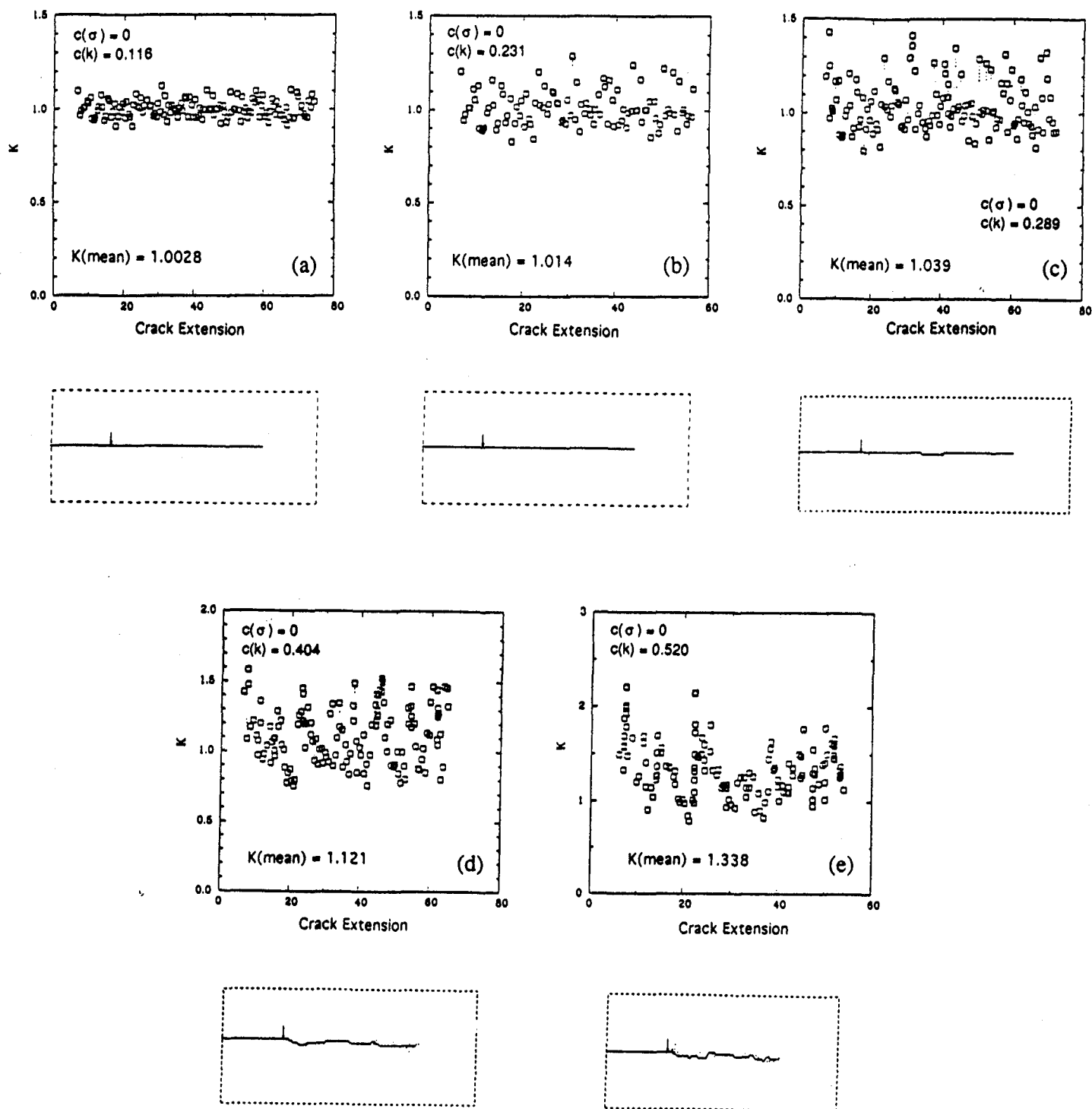


Fig. 10

Crack propagation experiments through fully dense material with variability in bond stiffness but constant maximum strength. The coefficients of variation in stiffness  $c(k)$  increase from a to e.



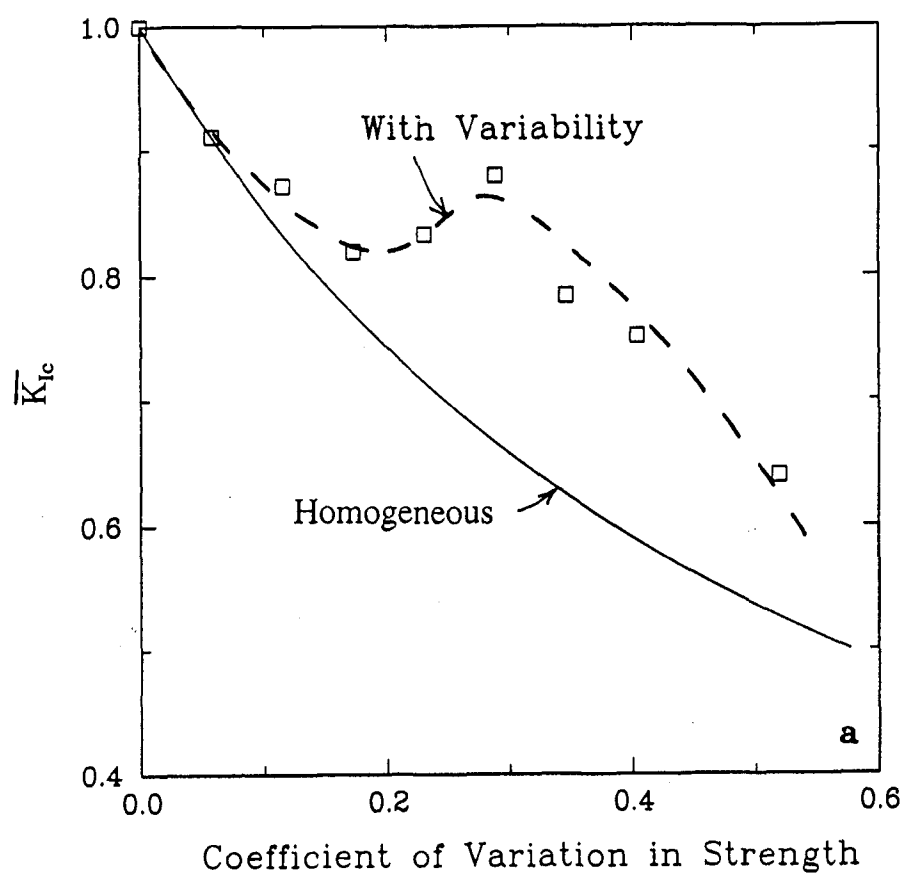


Fig. 11a Summary of results of simulations presented in Fig. 9 giving the dependence of average fracture toughness on the coefficients of variation of bond strength.

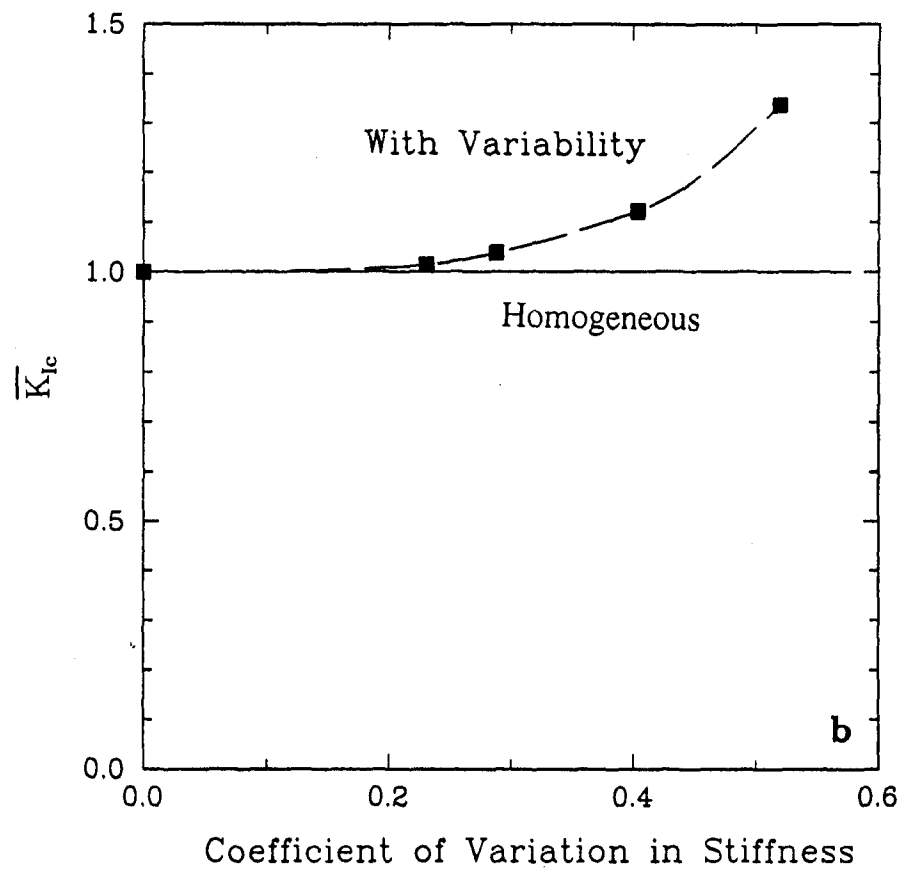


Fig. 11b

Summary of results of simulations presented in Fig. 10, giving the dependence of average fracture toughness on the coefficient of variation of bond stiffness.

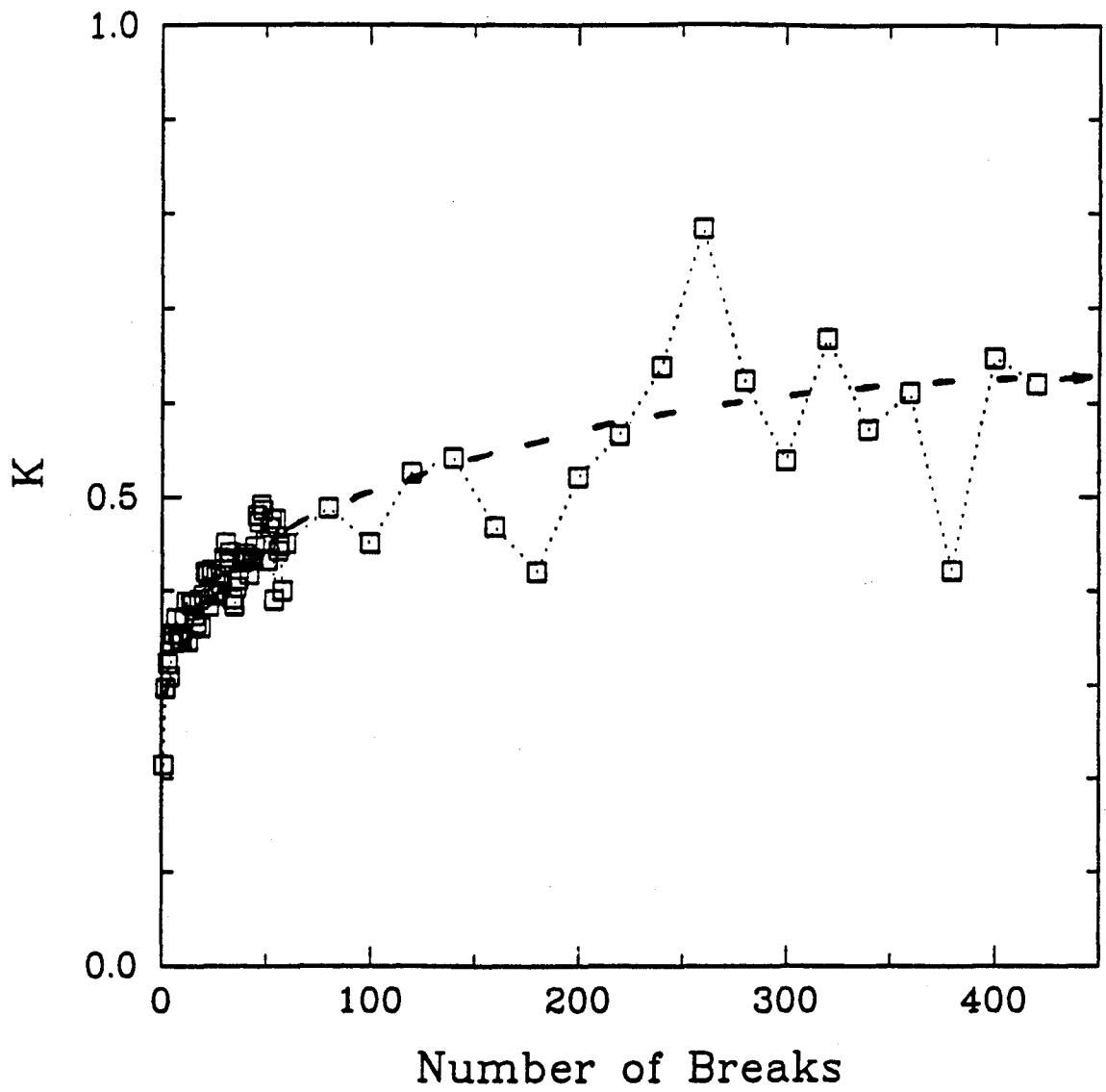


Fig. 12

R-curve behavior of a structure with a high coefficient of variation in strength of  $c(\sigma_c) = 0.52$ .

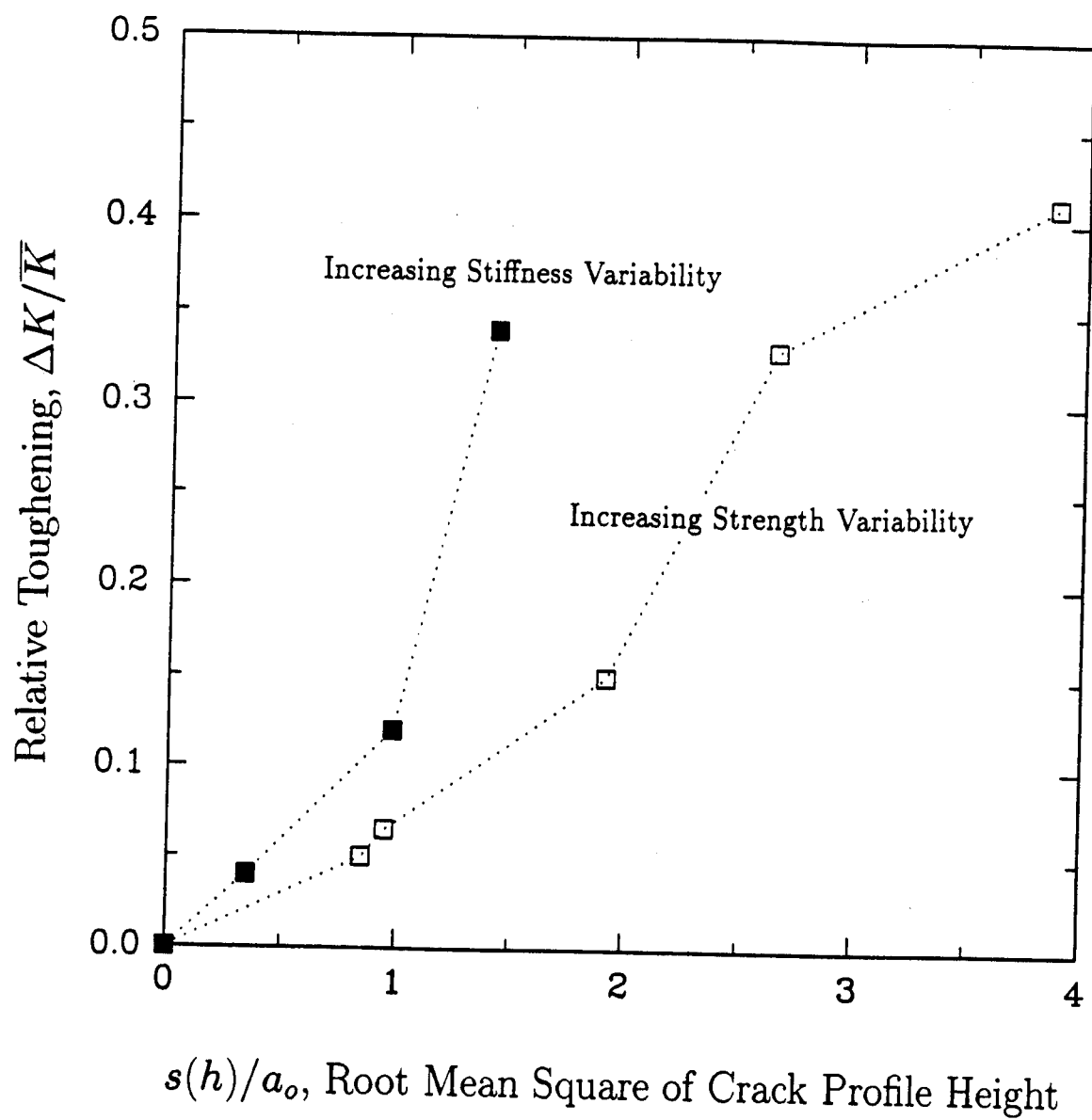


Fig. 13

The correlation between rms crack profile height and the relative toughness indicates crack deviation from planar morphology relates to measured toughness due to such effects as crack deflection and microcracking.

Correlated

$$\overline{K_I} = 0.65$$



Uncorrelated

$$\overline{K_I} = 0.87$$

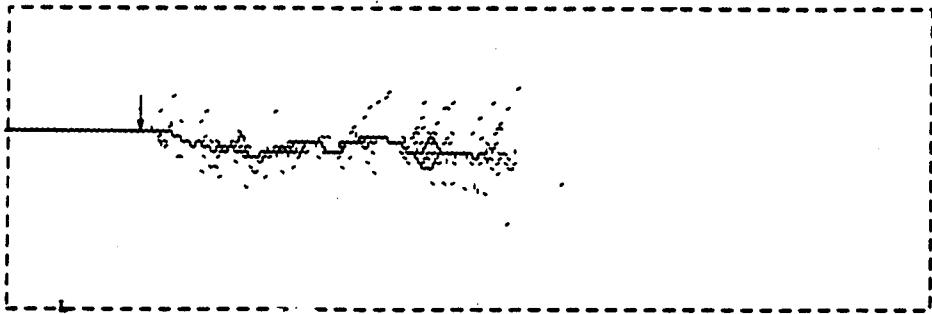


Fig. 14

The effect of perfect correlation between bond stiffness and strength on fracture toughness, for a coefficient of variation of 0.346, in both strength and stiffness, compared with a case in which variability in strength and stiffness is uncorrelated.

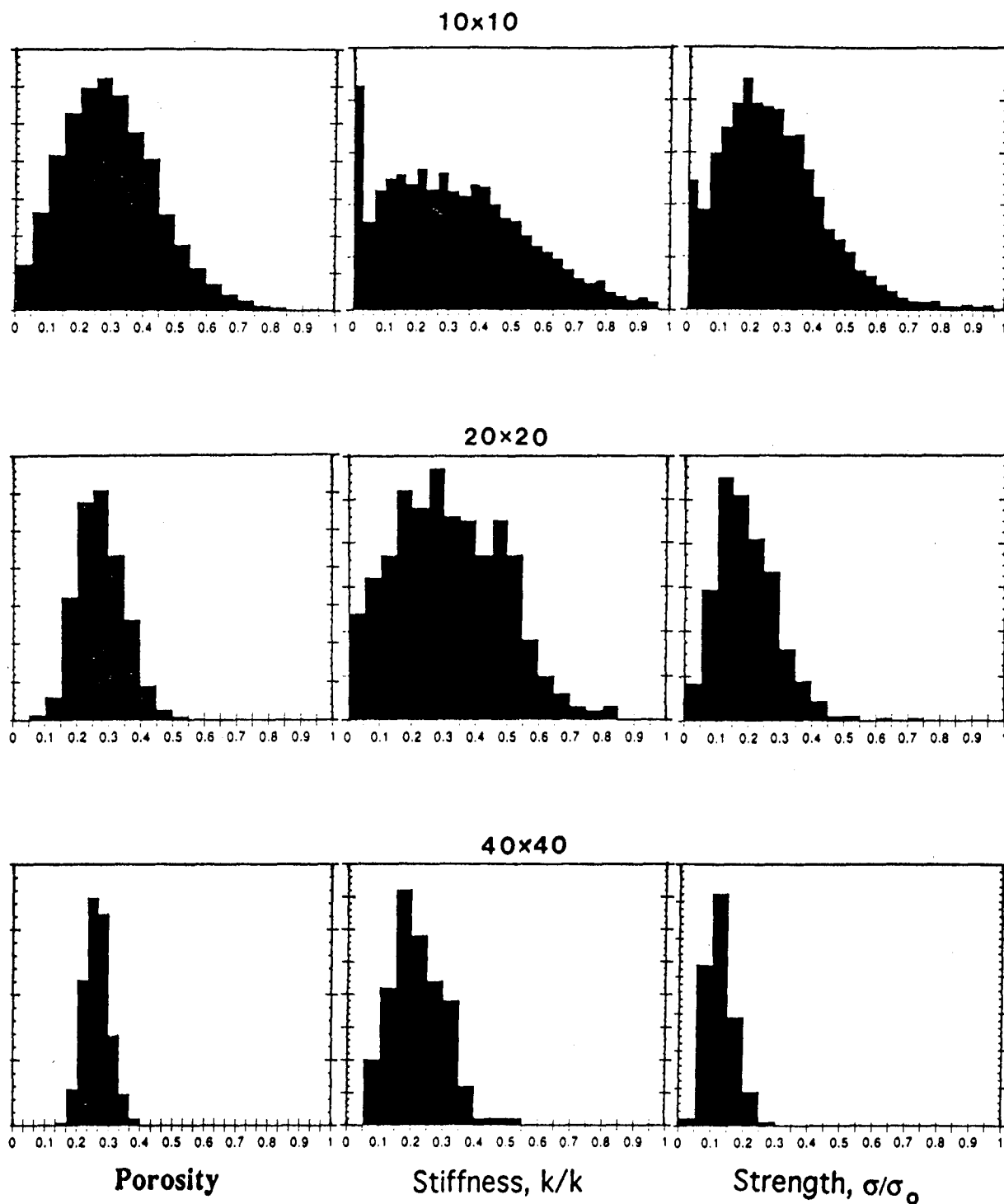


Fig. 15      Strength, stiffness and porosity distributions obtained by probing potential representative volume elements of a large simulated microstructure which spans 10,000 volume elements. Upper row for elements of 10 mesh points on the side, middle and lower rows for elements 20 and 40 mesh points on the side, respectively.

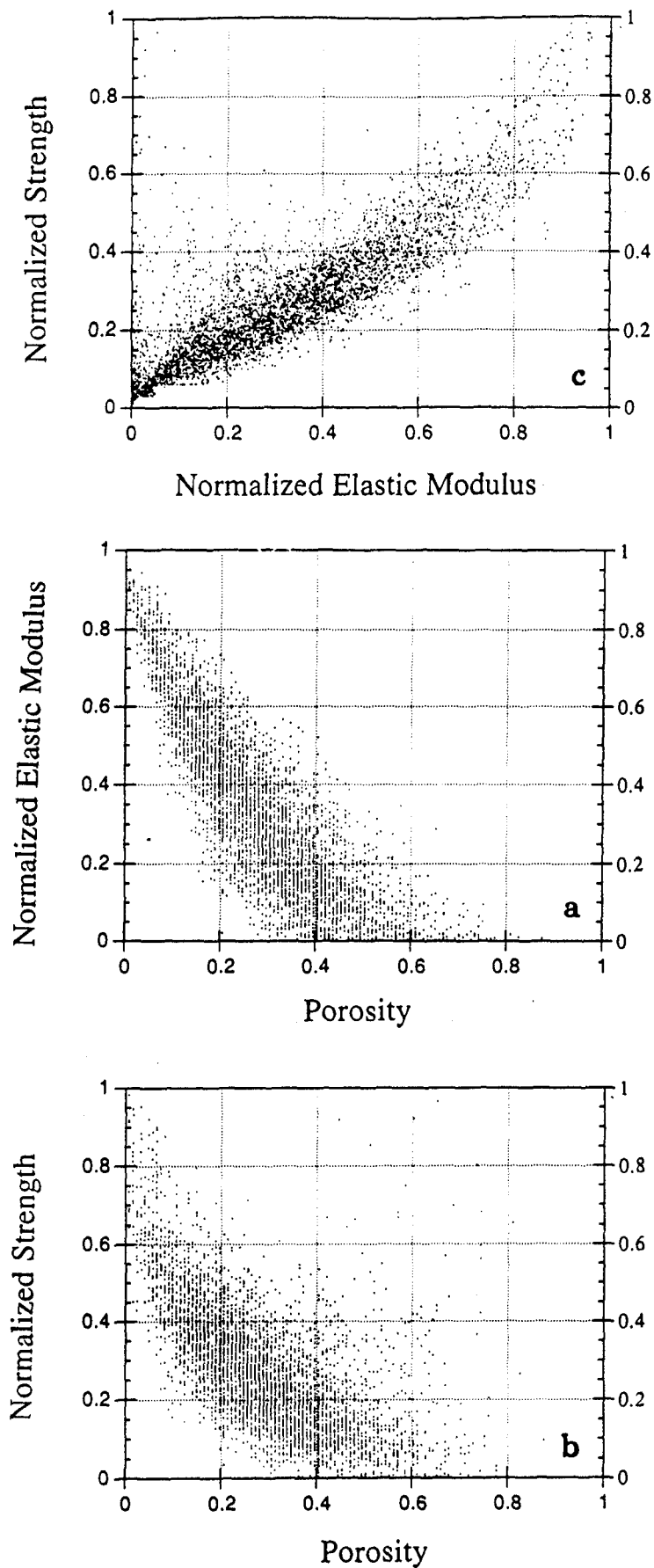


Fig. 16

Spread of normalized stiffness (a) and, strength (b) with porosity in  $10^4$  VEs of 10 mesh points on the side, tested to sample realistic distributions. Correlation of normalized strength with normalized stiffness (c).

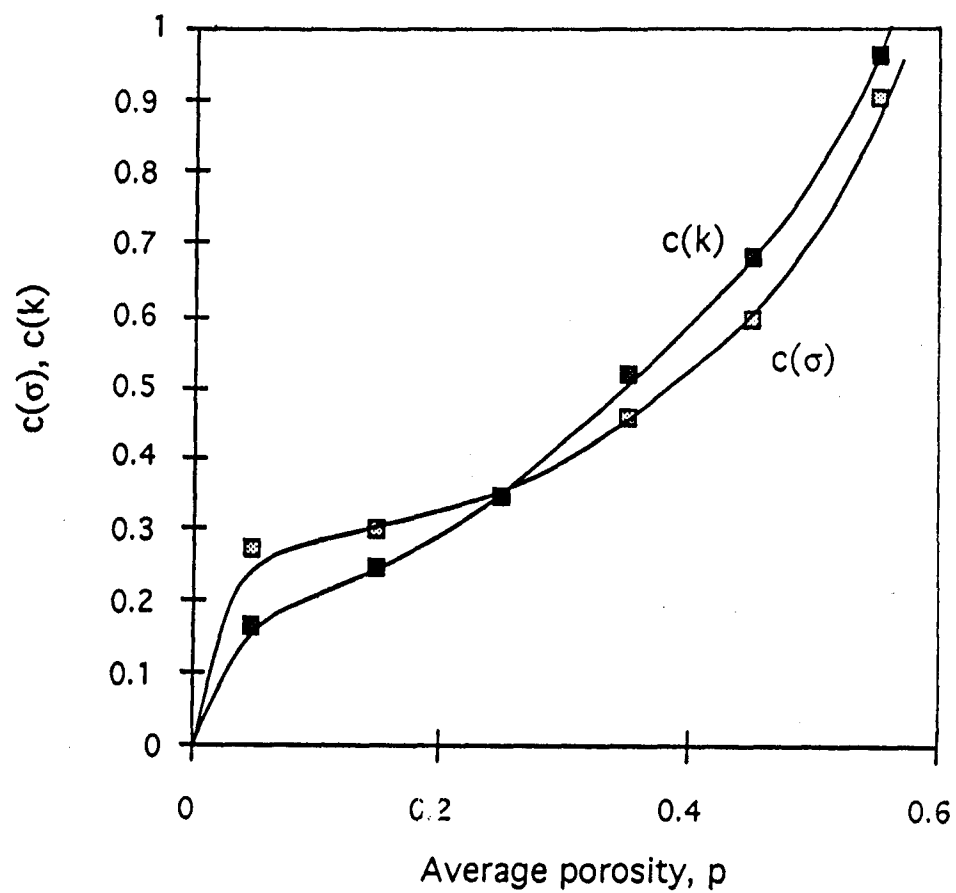


Fig. 17

Dependences of the coefficients of variation in strength and stiffness on porosity for the simulations presented in Fig. 16.



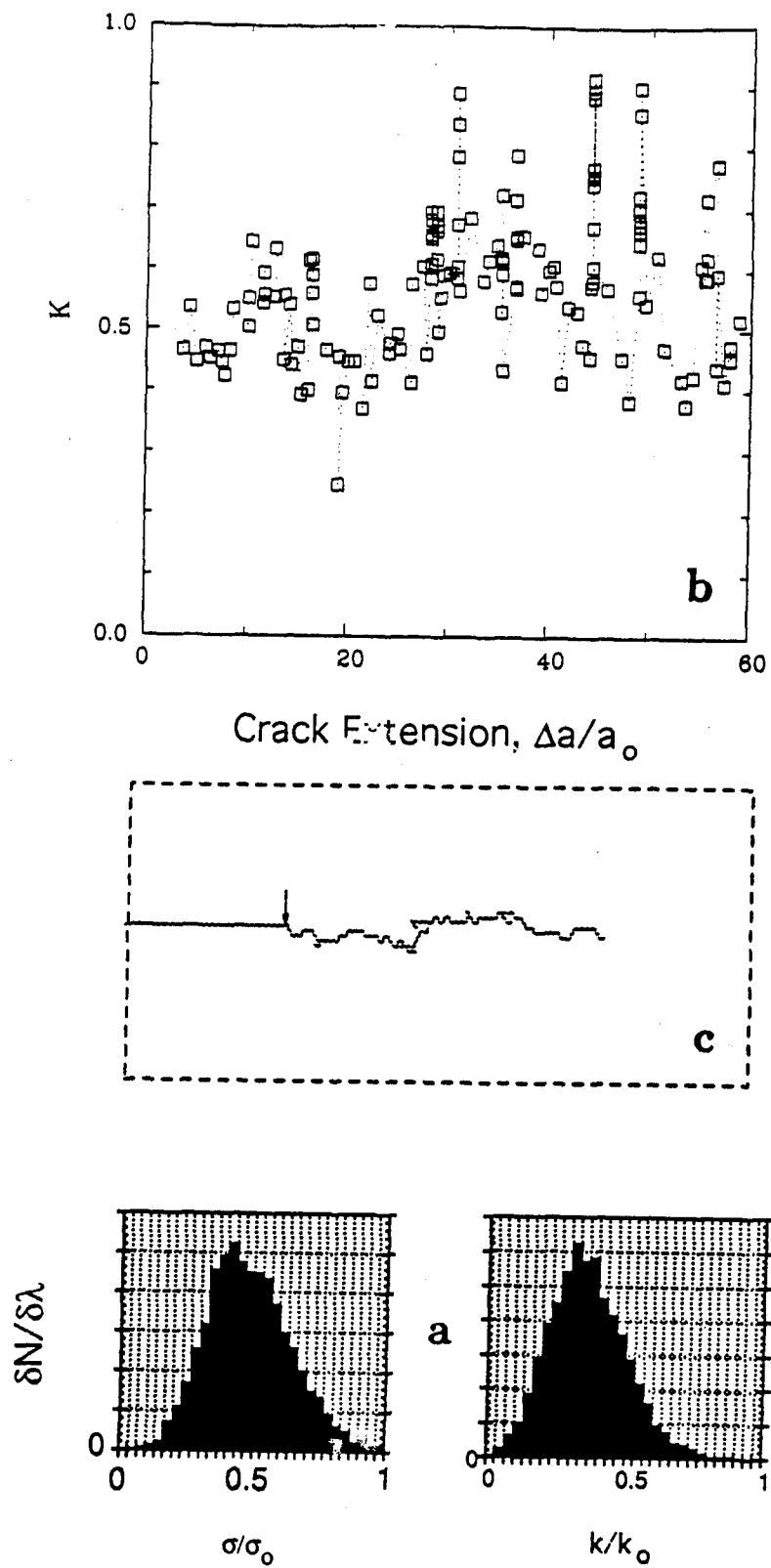


Fig. 18

Effective three dimensional strength and stiffness distributions embodied in the 2-D super element: (a) frequency distributions; (b) evolution of crack propagation resistance; (c) crack plane tortuosity.

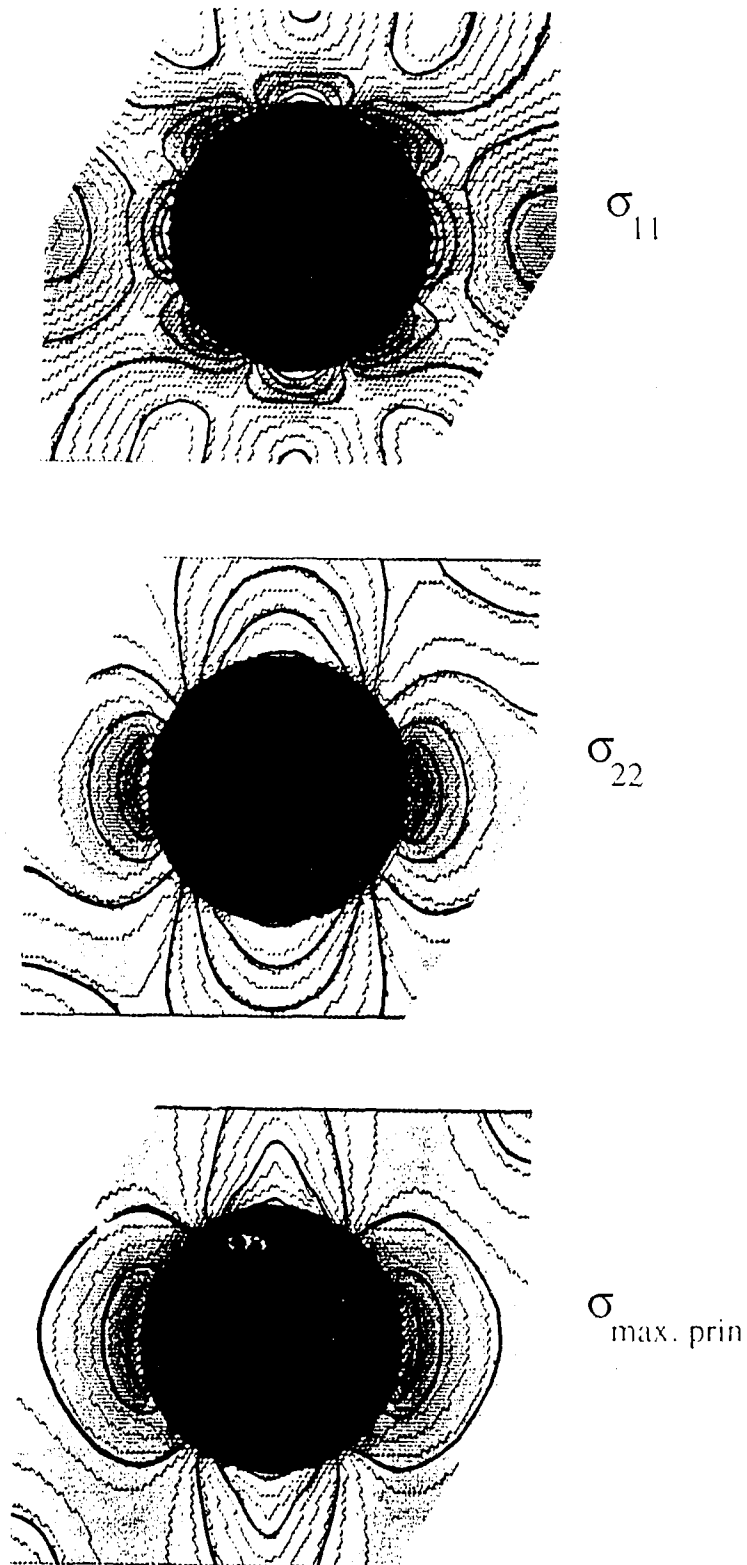


Fig. 19

Stress field solution comparison between a finite element generated solution and the discrete spring network model for an infinite hexagonal array of pores with spacing to diameter ratio of 4 under uniaxial strain. Loading direction ( $x_1$ ) is vertical. Heavy black lines represent the continuum FEM solution, shading and thin lines represent discrete spring stress solution.